August 2013

Aqueous Turbulence Structure Immediately Adjacent to the Air - Water Interface and Interfacial Gas Exchange

Binbin Wang
University of Wisconsin-Milwaukee

AQUEOUS TURBULENCE STRUCTURE IMMEDIATELY ADJACENT TO THE AIR – WATER INTERFACE AND INTERFACIAL GAS EXCHANGE

by

Binbin Wang

A Dissertation Submitted in

Partial Fulfillment of the

Requirements for the Degree of

Doctor of Philosophy

in Engineering

at

The University of Wisconsin-Milwaukee

August 2013

ABSTRACT

AQUEOUS TURBULENCE STRUCTURE IMMEDIATELY ADJACENT TO THE AIR – WATER INTERFACE AND INTERFACIAL GAS EXCHANGE

by

Binbin Wang

The University of Wisconsin – Milwaukee, 2013
Under the Supervision of Professor Qian Liao

Air-sea interaction and the interfacial exchange of gas across the air-water interface are of great importance in coupled atmospheric-oceanic environmental systems. Aqueous turbulence structure immediately adjacent to the air-water interface is the combined result of wind, surface waves, currents and other environmental forces and plays a key role in energy budgets, gas fluxes and hence the global climate system. However, the quantification of turbulence structure sufficiently close to the air-water interface is extremely difficult. The physical relationship between interfacial gas exchange and near surface turbulence remains insufficiently investigated. This dissertation aims to measure turbulence *in situ* in a complex environmental forcing system on Lake Michigan and to reveal the relationship between turbulent statistics and the CO_2 flux across the air-water interface. The major objective of this dissertation is to investigate the physical control of the interfacial gas exchange and to provide a universal parameterization of gas transfer velocity from environmental factors, as well as to

propose a mechanistic model for the global CO_2 flux that can be applied in three dimensional climate-ocean models.

Firstly, this dissertation presents an advanced measurement instrument, an *in situ* free floating Particle Image Velocimetry (FPIV) system, designed and developed to investigate the small scale turbulence structure immediately below the air-water interface. Description of hardware components, design of the system, measurement theory, data analysis procedure and estimation of measurement error were provided.

Secondly, with the FPIV system, statistics of small scale turbulence immediately below the air-water interface were investigated under a variety of environmental conditions. One dimensional wave-number spectrum and structure function sufficiently close to the water surface were examined. The vertical profiles of turbulent dissipation rate were intensively studied. Comparison between the turbulence structures measured during the wind wave initiation period and those obtained during the growing period was presented. Significant wave effects on near surface turbulence were found. A universal scaling law was proposed to parameterize turbulent dissipation rate immediately below the air-water interface with friction velocity, significant wave height and wave age.

Finally, the gas transfer velocity was measured with a floating chamber (FC) system, along with simultaneously FPIV measurements. Turbulent dissipation rate both at the interface and at a short distance away from the interface (~ 10 cm) were analyzed and used to examine the small scale eddy model. The model coefficient was found to be dependent on the level of turbulence, instead of being a constant. An empirical relationship between the model coefficient and turbulent dissipation rate was provided, which improved the accuracy of the gas transfer velocity estimation by more than 100%

for data acquired. Other data from the literature also supported this empirical relation. Furthermore, the relationship between model coefficient and turbulent Reynolds number was also investigated. In addition to physical control of gas exchange, the disturbance on near surface hydrodynamics by the FC was also discussed. Turbulent dissipation rates are enhanced at the short distance away from the interface, while the surface dissipation rates do not change significantly.

Acknowledgments

I would like to express my sincere gratitude to my advisor, Dr. Qian Liao, who not only facilitated my entry to the field of environmental fluid mechanics, but also directed me in conducting field experiments and solving complex research problems with his great talent and experiences. His kindness, patience, support, humor and friendship made the discovering process during my Ph.D. program valuable and fun. My growth as a scientist has greatly benefited from his knowledge and personality.

I am particularly grateful to Dr. Harvey A. Bootsma for being a knowledgeable and conscientious reader of the manuscript. I wish to thank him for his valuable advice and comments. I would also like to express my gratitude to my thesis committee including Dr. Hector Bravo, Dr. Ryoichi S. Amano, Dr. Val Klump and Dr. Paul J. Roebber, for their insights and availability.

I am deeply grateful to my colleagues in the Department of Civil Engineering and Mechanics and School of Fresh Water Sciences, especially Mr. Jianen Xiao, Ms. Xinxin Wang, Dr. Lei Tan, Mr. Chunqi Shen, Mr. Joseph H. Fillingham and other research members in Dr. Bootsma's lab, for their companion and help on this work.

I would also like to express my gratitude to the research staff in Great Lakes WATER institute and community of the UWM Ph.D. program, including the faculty, staff and students. Their efforts are deeply appreciated.

Finally, I would like to acknowledge my wife Dejun and my daughter Sophia for their loving support and constant encouragement throughout the time that this work was in progress. I would like to share this accomplishment with them.

The financial support from the US National Science Foundation and the Wisconsin Sea grant is greatly acknowledged.

Thanks to all of you.

Contents

LIST OF FIGURES

LIST OF TABLES

NOMENCLATURE

a	Wave amplitude
$a(t)$	Local amplitude of analytic signal from HHT
c'	Instantaneous concentration fluctuation
c_p	Phase speed of characteristic wave
C	CO_2 concentration in the floating chamber
C_a	Bulk gas concentration at air phase
C_D	Drag coefficient
C_s	Smogorinsky constant
C_w	Bulk gas concentration at water phase
C_{wt_1}	Concentration of released tracer in water at time t_1
C_{wt_2}	Concentration of released tracer in water at time t_2
D	Molecular diffusivity
D^{2D}	Two dimensional velocity gradient tensor
D_H	Thermal conductivity of water
D_{ij}	Second order structure function
E_{ij}	One dimensional velocity spectra
E_u	One dimensional velocity spectrum along the horizontal direction for horizontal velocity component
E_w	One dimensional velocity spectrum along the horizontal direction for horizontal vertical component
f	Surface renewal frequency
F	Gas flux across the air-water interface

g	Gravitational acceleration
h	Mean depth of mixed layer
$H(t)$	Hilbert transform of input singal $X(t)$
H_s	Significant wave height
k	Gas transfer velocity
k_0	Gas transfer velocity due to other factors except for bubbles
k_b	Gas transfer velocity due to bubble effect
k_{600}	Gas transfer velocity of CO_2 at 20 ℃ for fresh water
k_{660}	Gas transfer velocity of CO_2 at 20 ℃ for sea water
k_H	Interfacial transfer velocity of heat
K_m	Turbulent diffusivity of momentum
K_c	Turbulent diffusivity of gas concentration
l	Mixing length
L	Turbulence integral length scale
L_B	Batchelor's micro-scale
pCO_{2w}	Partial pressure of CO_2 in water
pCO_{2a}	Partial pressure of CO_2 in air
P_c	TKE production with ensemble averaging
P_w	TKE production that includes the effects of wave induced velocities
q	Turbulent velocity scale
R_ε	Enhancement ratio of dissipation rate
R_k	Enhancement ratio of gas transfer velocity
s_{ij}	Rate of strain tensor

$\bar{S}_{ij}$	Rate of strain tensor at resolved scale of large eddy PIV analysis
t	Time
T	Wave period
t_1	Mass balance start time of tracer release
t_2	Mass balance end time of tracer release
u_i	Instantaneous velocity components
u_*	Surface shear velocity
u_{*a}	Shear velocity at air side
u_{*w}	Shear velocity at water side
$\tilde{u}_i$	Instantaneous wave induced orbital velocity component
u	Instantaneous streamwise velocity
u'	Instantaneous streamwise fluctuating velocity
$\tilde{u}$	Instantaneous wave induced orbital velocity (horizontal component)
$\breve{u}_i$	Velocities at unresolved scale of large eddy PIV analysis
U	Ensemble averaged velocity
U_{10}	Wind speed at 10 meter above the water surface
$\overline{U}_i$	Velocities at resolved scale of large eddy PIV analysis
v	Instantaneous spanwise velocity
v'	Instantaneous spanwise fluctuating velocity
w	Instantaneous vertical velocity
w'	Instantaneous vertical fluctuating velocity
$\tilde{w}$	Instantaneous wave induced orbital velocity (vertical component)

x_i	Coordinates
x	Streamwise coordinate
$X(t)$	Input signal for HHT
y	Spanwise coordinate
z	Vertical coordinate
z_0	Surface roughness length
$Z(t)$	Analytic signal from HHT
α	Model coefficient in the Small Scale Eddy Model
β	Wave age
δ, δ_D	Thickness of diffusivity boundary layer
Δ	Window size of large eddy PIV analysis
ε	Turbulent dissipation rate
ε_D	Turbulent dissipation rate estimated though direct method
ε_{iso}	Turbulent dissipation rate in isotropic turbulence
ε_{LES}	Turbulent dissipation rate estimated though large eddy PIV approach
ε_{LF11}	Turbulent dissipation rate estimated though one dimensional horizontal velocity spectrum fitting
ε_{LF33}	Turbulent dissipation rate estimated though one dimensional vertical velocity spectrum fitting
ε_{LOW}	Turbulent dissipation rate calculated from LOW scaling
ε_{SF11}	Turbulent dissipation rate estimated though second order horizontal structure function fitting

ε_{SF33}	Turbulent dissipation rate estimated though second order vertical structure function fitting
ε_{SGS}	Reynolds averaged SGS dissipation rate of TKE
ϕ	Maximum rotation angle of PIV system
κ	Wave number
κ	Von Kármán constant
λ	Wave length
η	Kolmogorov length scale
$\eta(t)$	Surface elevation signal
ν	Kinematic viscosity of water
γ	Surface divergence
θ_s	Exposure time scale of surface renewal model
$\theta(t)$	Phase angle of analytic signal from HHT
ρ_a	Density of air
ρ_w	Density of water
τ_i	Shear stress at air-water interface
τ_{ij}	SGS stress tensor
ω	Angular frequency of waves
ω_{sys}	Artificial vorticity induced by system rotation
Pr	Prandtl number
Re	Reynolds number
Re_t	Turbulent Reynolds number

Re_w	Reynolds number defined wave parameters
Sc	Schmidt number
Sc_t	Turbulent Schmidt number
ADCP	Acoustic Doppler Current Profilers
ADV	Acoustic Doppler Velocimetry
DBL	Diffusive boundary layer
EMD	Empirical mode decomposition
FC	Floating chamber
FOV	Field of view
FPIV	Free-floating Particle Image Velocimetry
HHT	Hilbert huang transform
IMF	Intrinsic mode function
LES	Large eddy simulation
LOW	Law of the wall
MKE	Mean kinetic energy
PIV	Particle Image Velocimetry
SDM	Surface divergence model
SEM	Small scale eddy model
SGS	Sub-grid-scale
TKE	Turbulent kinetic energy
WASL	Wave affected surface layer
WKE	Wave kinetic energy

Chapter 1

Introduction

1.1 background and motivation

Gas exchange across the air-water interface is an important process in atmosphere – aquatic system coupling and relevant to global biogeochemical cycling and climate. The physical transport of gas across the air-water interface is governed by the interplay of molecular and turbulent transport processes across several boundary layers immediately adjacent to the interface. For example, turbulent motions damp at viscous boundary layer where molecular viscosity controls the mechanism of momentum transport; mass transport processes across the diffusive boundary layer (DBL) are dominated by molecular diffusion. The random bursts of turbulent eddies renew the water surface and hence control the strength of the gas exchange across the air-water interface, referred to surface renewal model [*Danckwerts*, 1951]. The coefficient controlling the speed of gas exchange across the air-water interface, that is, the transfer velocity k is given by Ficks diffusion law: $k = D/\delta$, where D is molecular diffusivity of gas of interest and δ is thickness of DBL.

In the past decades, many efforts have been made to parameterize the transfer velocity in variety of laboratory and field aquatic systems [*Ho et al.*, 2011a; *Jähne et al.*, 1987; *R Wanninkhof*, 1992]. Most of studies are focused over a range of temporal and spatial scales in the ocean and wind speed parameterizations are routinely established [*Nightingale et al.*, 2000; *R Wanninkhof*, 1992]. However, wind speed is not the only factor that dominates gas transfer velocity due to complexity of environmental forcing. In river and estuaries, gas transfer velocities were found to be correlated with combined effect of wind speed, current velocity and water depth [*Raymond and Cole*, 2001].

Although a transfer velocity can be well parameterized by environmental forces, the relationship among them is location specific. Recently, evidence shows that the gas transfer velocity is directly correlated to near surface turbulence [*Zappa et al.*, 2007], characterized by a small scale eddy model (SEM) [*Lamont and Scott*, 1970]:

$$k = \alpha(\varepsilon\nu)^{1/4} Sc^{-n} \tag{1}$$

where ε is the turbulent kinetic energy dissipation rate at the surface; ν is the kinematic viscosity of water; Sc is the Schmidt number defined as $Sc = \nu / D$; α is the coefficient.

In SEM, the concept of surface renewal is related with the near surface hydrodynamics through the renewal time scale τ, determined by Kolmogorov time scale,

$$\tau \sim (\nu / \varepsilon)^{1/2} \tag{2}$$

Generally, the environmental parameters are appreciated proxies that dominate the near surface turbulence mechanism in different aquatic systems. Wind shear is dominant in oceans and large lakes [*R Wanninkhof*, 1992], current or tidal velocities are dominant in shallow rivers and estuaries. Other environmental factors also need to be considered in the natural system, such as rainfall [*Ho et al.*, 1997], wind fetch [*Borges et*

al., 2004], breaking wave induced bubbles [*Woolf*, 1997] and micro-scale wave breaking associated vortex structures [*Zappa et al.*, 2004]. Among these factors, the wide range of applications of small scale eddy model (SEM) can be insured by measuring or modeling ε in the water sufficiently close to the interface, regardless of the generation mechanism of turbulence. *Soloviev et al.* [2007] estimated transfer velocity based on SEM from remote sensing data, accounting for the effect of shear, convection and breaking waves. More recently, the SEM has been utilized to estimate gas transfer velocity in lakes with great impact of convective motion [*MacIntyre et al.*, 2010; *Read et al.*, 2012].

However, due to the strong dependency of turbulent dissipation rates on the distance away from the air-water interface at the ocean upper layer, the dissipation rate measurement location is critical to the coefficient α in the SEM. To date, field applications of the SEM have been made by measuring turbulent dissipation rate over a large range of distances (from tens of centimeters to meters) away from interface [*Vachon et al.*, 2010; *Zappa et al.*, 2007]. As a result, the coefficient α (determined by linear regression of predicted transfer velocity against measured data) varies significantly with the depth at which the turbulent dissipation rate is measured.

Alternatively, surface divergence has been shown to be correlated to transfer velocity at the unsheared free water surface, known as the surface divergence model [*McCready et al.*, 1986]:

$$k \sim Sc^{-1/2}(\nu\bar{\gamma}_{RMS})^{1/2} \tag{3}$$

where $\bar{\gamma}_{RMS}$ is the root mean square of surface divergence, defined as,

$$\bar{\gamma}_{RMS} = \sqrt{\left.\overline{\left(\frac{\partial u'}{\partial x} + \frac{\partial v'}{\partial y}\right)^2}\right|_{\text{int}}} \tag{4}$$

where u' and v' are fluctuating horizontal velocities, and subscript "int" denotes the air-water interface. In this study, $\bar{\gamma}_{RMS}$ is evaluated through the expression,

$$\bar{\gamma}_{RMS} = \sqrt{\left(\frac{\partial w'}{\partial z}\right)^2}\Bigg|_{\text{int}} \tag{5}$$

where the vertical gradient of vertical velocity fluctuating component $\frac{\partial w'}{\partial z}$ is easily measured from aqueous side *in situ* PIV system.

Banerjee et al. [2004] pointed out that the "surface divergence" physically is the signature of turbulent "sweep" events representing local "upwelling" motions at the surface from the bulk fluid. On the other hand, it is an alternative expression of the surface renewal and more specifically modeled by tangential components of velocities at the interface. In the laboratory facility the surface divergence can be measured by surface PIV system [*Asher et al.*, 2012]. However, as to our knowledge, the field implementation of surface divergence has never been done associated with transfer velocity measurements.

Due to evidence of the relationship between near surface turbulence and interfacial gas exchange, it is important to simultaneously measure the statistics of near surface turbulence and gas flux across the air-water interface. However, to date, most field measurements of the turbulence dissipation rate have been conducted in the ocean upper layer (O(1-10m)) through indirect means, such as the spectra fitting method. Breaking waves have been considered as a direct source of near surface turbulence due to momentum transfer into the water column [*Melville*, 1996; *Melville et al.*, 2002]. Breaking associated dissipation of wave energy has been extensively studied [*Lamarre*

and Melville, 1991; *Rapp and Melville*, 1990]. Highly intermittent turbulent energy dissipation due to wave-breaking is of great importance for the air-water flux of gas and heat. Direct measurements of the turbulence intensity in both laboratory and field studies indicate that the decay of turbulence intensity follows a power law relationship with time [*J R Gemmrich and Farmer*, 2004; *Melville et al.*, 2002; *Rapp and Melville*, 1990]. Non-breaking waves without wind shear are suggested as another important source of near surface turbulence. Wave orbital motion can directly generate turbulence when the Reynolds number, defined according to wave conditions ($\mathrm{Re}_w = a^2\omega/\nu$), is above a critical value [*Babanin and Haus*, 2009]. Here, a is the wave amplitude at the water surface, ω is the angular frequency of the wave, and ν is kinematic viscosity of water. However, the generation of turbulence due to this mechanism is still not clearly understood. With the triple decomposition of the instantaneous velocity field, i.e., $u_i(x_i,t) = \bar{u}_i(x_i) + \tilde{u}_i(x_i,t) + u_i'(x_i,t)$, where $\bar{u}_i$ is the mean current velocity, $\tilde{u}_i$ is wave induced orbital velocity and u_i' is turbulent fluctuation, *Cheung and Street* [1988] suggested that wave induced Reynolds stresses transfer kinetic energy from the wave to mean flow and eventually to turbulence, because the wave kinetic energy production term $-\overline{\tilde{u}\tilde{w}}\frac{\partial \bar{u}}{\partial z}$ is generally negative, while the turbulent production term $-\overline{u'w'}\frac{\partial \bar{u}}{\partial z}$ is typically positive. Moreover, the near surface turbulence is affected by wave induced Stokes drift and strongly interacts with surface wave motion [*Ardhuin and Jenkins*, 2006; *Thais and Magnaudet*, 1996; *Veron et al.*, 2009].

In order to better understand turbulence in the ocean upper layer, much effort has been put into designing instruments or systems to quantify turbulence *in situ*. For

example, *in situ* platforms or vehicles [*Dhanak and Holappa*, 1999; *Osborn and Lueck*, 1985] carrying a variety of sensors have been deployed to measure turbulence in the open ocean. In the past several decades, Acoustic Doppler Velocimetry (ADV) and Acoustic Doppler Current Profilers (ADCP) have been extensively applied for field turbulence measurements. Several methods have been developed to estimate dissipation rate with ADCP measurements [*Lorke and Wuest*, 2005]. However, coarse spatial resolution and high background noise near the water surface make it difficult to resolve the detailed structures of turbulence just beneath the water surface. Most field measurements of turbulence in the upper layer have been made within several meters beneath the air-water interface. Turbulence within a very short distance (<20 cm) of the surface is typically extrapolated from data measured below. Direct observations in this thin layer of surface water are needed in order to validate mechanistic models of the gas transfer velocity, such as the eddy cell model, in which the dissipation rate immediately below the water surface needs to be quantified. Recently, attempts have been made to measure high resolution near surface turbulence structures. For example, a high resolution ocean upper layer observation was conducted by *J Gemmrich* [2010], who applied a single beam Doppler Sonar to measure the vertical profiles of dissipation rate using the structure function method.

Particle Image Velocimetry (PIV) has been used to investigate the surface boundary layer turbulence in the laboratory [*Babanin and Haus*, 2009; *Peirson*, 1997]. Near surface coherent structures can be resolved in the vertical 2-D velocity map derived from PIV measurements. Using this approach in laboratory studies, "eddies" with high vorticity have been detected and are considered to be associated with micro-breaking

events in the near surface region [*M H K Siddiqui and Loewen*, 2007]. In general, standard PIV systems are unsuitable for field deployments due to complex optical configurations and high demands on electrical power and computing resources. Nevertheless, a partially submersible PIV system has been developed and successfully deployed to study turbulent flow structures in coastal oceans during the past decade [*Doron et al.*, 2001; *Hackett et al.*, 2011; *Nimmo Smith et al.*, 2002]. More recently, with the development of compact diode lasers and diode-pumped solid state (DPSS) laser technologies, battery-powered, self-contained *in situ* PIV systems [*Katija and Dabiri*, 2008; *Liao et al.*, 2009; *Tritico et al.*, 2007] have been developed, extending PIV measurements from the laboratory to field studies. For example, *Steinbuck et al.* [2010] used a stereoscopic PIV along with a biological profiler to quantify physical and biological structure in the upper layer of the ocean.

1.2 Scope and objective

In this dissertation, an *in situ* measurement system has been developed to simultaneously quantify the near surface turbulence and CO_2 flux across the air-water interface. Furthermore, the turbulence structure immediately below the air-water interface was examined at the wind wave surface layer of Lake Michigan.

The objective of this research is to provide *in situ* data to better understand the relation between the interfacial gas flux and near surface hydrodynamics under a variety of environmental forcing conditions. A free floating PIV system was designed, developed and tested for field deployment. With the advanced technique, the hydrodynamics model

of interfacial gas exchange was investigated with *in situ* data of the PIV system and compared with the direct measurement of CO_2 flux by using a floating chamber (FC) and a portable gas analyzer. The physical control of the gas exchange was examined carefully.

Furthermore, I am specifically interested in the vertical turbulence structure sufficient close to the water surface at the existence of surface gravity waves. A universal parameterization of vertical structure of near surface turbulence dissipation rate would be investigated based on the meteorological data and wave parameters. To study the wave impact on near surface turbulence and interfacial gas exchange, a series of field experiments were conducted in the surface layer of Lake Michigan and the embayment of Milwaukee harbor for multiple purposes. The primary objectives of this dissertation is listed as follows:

[1] To develop an in situ Particle Image Velocemitry system to measure statistics of turbulence immediately below the air-water interface.

[2] To investigate the hydrodynamics model of interfacial gas exchange rate, including the small scale eddy model and surface divergence model. The model coefficient would be carefully examined.

[3] To quantify wave impact to the near surface turbulence characteristics.

[4] To seek a universal scaling to normalize the turbulent dissipation rate immediately below the air-water interface.

In the long run, I hope to provide a comprehensive study on parameterization of near surface turbulence with the meteorological and hydrodynamic data and its application on interfacial gas flux.

1.3 Outline

The introduction of the background of this dissertation as well as the scope and objective of this dissertation has been presented in Chapter 1. Chapter 2 provides a detail of review of the process of mechanistic and experimental studies of gas exchange across the air-water interface. In Chapter 3, the development of a free floating Particle Image Velocimetry (FPIV) system is introduced. A series of field deployments of the FPIV is presented as well. Chapter 4 presents a series of experimental studies on turbulence structure immediately below the air-water interface. The wave impact on vertical turbulent dissipation rate profiles is discussed. In Chapter 5, the relation between the interfacial gas exchange and near surface turbulence is studied with in situ FPIV/FC measurements. Chapter 6 provides conclusions of this dissertation and recommendations for future studies.

Chapter 2

Review of Research Progress on Mechanistic and Experimental Studies on Gas Exchange Across the Air-Water Interface

2.1 Theoretical models

Oceans and the atmosphere are tightly coupled to influence the energy budget, gas exchange and the global climate. For example, 20%~30% anthropogenic emitted CO_2 was sequestered by oceans. The ocean surface boundary layer plays an intermediary role on the exchange of mass, momentum and energy between air and ocean. Quantifying transport terms (such as temperature, gas fluxes) across the air-water interface has been an important subject of physical oceanography for several decades.

The physical mechanism of interfacial gas exchange is complex for several reasons. (1) Fluid motions on both sides of the interface are typically turbulent, a stochastic feature with a wide range of scales; (2) The interface can be disturbed and hence deformed into irregular shapes, and interacts with the turbulence structure in both boundary layers.

Gas transfer velocity k is the key parameter that regulates the interfacial gas exchange, which is usually determined through experimental methods. The gas transfer velocity can be defined as

$$k = \frac{F}{C_w - \alpha C_a} \tag{1}$$

where, F is gas flux across the air water interface, C_w and C_a are bulk gas concentration at water and air phase, α is the Ostwald solubility coefficient.

It is a well accepted concept that the flux of slightly soluble gas (such as CO_2) across the air-water interface without wave breaking is largely controlled by the transport mechanism through a very thin aqueous diffusive boundary layer. The gas transfer velocity is determined by molecular transport though this thin layer, whose thickness is usually related to the level of turbulence very close to the interface

2.1.1 Film theory

The simplest model to quantify the interfacial gas exchange is film theory [*Lewis and Whitman*, 1924]. In this model, gas transfer occurs through a thin "stagnant" film of laminar fluid adjacent to the air-water interface of thickness δ. According to the Fick's diffusion law, the gas transfer velocity is given as,

$$k = \frac{D}{\delta} \tag{2}$$

where D is molecular diffusivity of the dissolved gas.

In reality, a "stagnant" diffusivity boundary layer (DBL) with a constant thickness is a poorly modeled concept, actual DBL is disrupted by sporadic "bursts" of turbulent

"eddies", which are large scale turbulent motions that lift "fresh" fluids to the surface and create renewed exposure to the air phase [*Danckwerts*, 1951; *Higbie*, 1935]. The gas transfer is still driven by molecular diffusion during the exposures. Therefore, the exposure time θ_s becomes a key parameter controlling the flux across the interface. And the thickness of near surface DBL is a dynamic value, which is related to properties of impinging turbulent eddies.

2.1.2 Penetration model and surface renewal model

In the penetration model [*Higbie*, 1935], near surface DBL is periodically disrupted by penetrating eddies from the bulk water body with a constant exposure time scale. In contrast, the surface renewal model [*Danckwerts*, 1951] considers a random renewal time function, hence the average time is introduced to represent the exposure of elements of surface. Therefore, gas transfer velocity is described as,

$$k = \sqrt{\frac{4D}{\pi\theta_s}} \qquad \text{(Penetration model)} \qquad (3)$$

$$k = \sqrt{\frac{D}{\theta_s}} \text{ or } k = \sqrt{Df} \qquad \text{(Surface renewal model)} \qquad (4)$$

where f is the surface renewal rate. In these two models, gas transfer velocity are modeled by,

$$k \sim D^{1/2} \qquad (5)$$

Both laboratory and fields studies have shown that k is better modeled by the surface renewal model than by the "stagnant film" model[*Jähne et al.*, 1984; *Upstill-*

goddard et al., 1990]. And k is observed as $k \sim D^n$, where n varies between 1/2 and 2/3, depending on free surface roughness and near surface hydrodynamics [*Jähne et al.*, 1987].

2.1.3 Random eddy model

Differing slightly from the concept of surface renewal, *Harriott* [1962] proposed that near surface random eddies would also enhance the gas flux while approaching air-water interface even without completely renewing the interfacial layer. Laboratory study of renewal events of a thermal boundary layer (TBL) has proven that significant fraction of renewal events do not renew the TBL completely [*Jessup et al.*, 2009]. Gas transfer is therefore controlled by the eddy penetration depth and the lifetime of those random eddies [*Atmane et al.*, 2004].

Many efforts have been made to parameterize the mean time interval between surface renewals through the properties of near surface random eddies. The "large eddy model" [*Fortescue and Pearson*, 1967] argued that the renewal time scale is dominated by the largest turbulent eddies, which suggested,

$$\theta_s \sim L / u' \tag{6}$$

where L is the integral length scale and u' is the root-mean-square of fluctuating turbulent velocities.

One the other hand, the "small eddy model" [*Banerjee et al.*, 1968; *Lamont and Scott*, 1970] suggested that the smallest eddies are the controlling mechanism of interfacial gas exchange. Thus the renewal time scale is determined by Kolmogorov time scale,

$$\theta_s \sim (\nu / \varepsilon)^{1/2} \tag{7}$$

where ν is kinematic viscosity and ε is turbulent dissipation rate at the interface.

If substituting the renewal time scale into transfer velocity given by surface renewal model (e.g. equation (4)), k can be written as,

$$k \sim Sc^{-1/2} u' \mathrm{Re}_t^{-1/2} \text{ (large eddy model)} \tag{8}$$

$$k \sim Sc^{-1/2} u' \mathrm{Re}_t^{-1/4} \text{ (small eddy model)} \tag{9}$$

where Sc is Schmidt number defined as $Sc = \nu / D$, Re_t is turbulent Reynolds number, which is defined,

$$\mathrm{Re}_t = u' L / \nu . \tag{10}$$

In the "small scale eddy" model, dissipation rate has been scaled with the large scale eddies as,

$$\varepsilon \sim u'^3 / L \tag{11}$$

following the concept of turbulent energy cascade. These hydrodynamic models have shown good agreement with both laboratory and field measurements on the interface gas transfer velocity. *Chu and Jirka* [1992] conducted simultaneous measurements on turbulence and gas concentrations in a grid-stirred tank to reveal the relation between large eddy motions and gas transfer with the turbulent Reynolds number varying from 80 to 660. Small scale eddy motions have also been shown to be correlated with gas flux in a variety of experiments [*Asher and Pankow*, 1986; *Zappa et al.*, 2003; *Zappa et al.*, 2007]. In the "small scale eddy" model, gas transfer velocity is generally expressed explicitly as related with near surface turbulent dissipation rate,

$$k \sim Sc^{-1/2} (\nu \varepsilon)^{1/4} \tag{12}$$

The "two regime model" proposed by *Theofanus et al.* [1976]combined the "large eddy model" and the "small eddy model" by arguing that different size of the near surface turbulent eddies dominate interfacial gas flux mechanism depending on the turbulent Reynolds number. That is, the "large eddy model" is more appropriate at low turbulent Reynolds numbers (Re_t< 500), and small scale eddies are more relevant at high turbulent Reynolds number flows (Re_t> 500),

$$k = 0.73 Sc^{-1/2} u' \mathrm{Re}_t^{-1/2} \text{ at } \mathrm{Re}_t > 500 \tag{13}$$

$$k = 0.25 Sc^{-1/2} u' \mathrm{Re}_t^{-1/4} \text{ at } \mathrm{Re}_t < 500 \tag{14}$$

2.1.4 Surface divergence model

Based on the source layer theory (or blocking theory) and considering the transport of homogeneous and isotropic turbulence in the far field away from the free surface without tangential shear [*Hunt and Graham*, 1978], *Banerjee* [1990] provided a "surface divergence model" that relates the gas transfer velocity to the divergence of horizontal velocities on the air-water interface,

$$k \sim Sc^{-1/2} u' \mathrm{Re}_t^{-1/2} \left[\left\langle \frac{\partial u'}{\partial x} + \frac{\partial v'}{\partial y} \right\rangle^2 \right]_{\mathrm{int}}^{1/4} \tag{15}$$

where *u'* and *v'* are fluctuating horizontal velocities, and subscript "*int*" denotes the air-water interface.

Banerjee et al. [2004] pointed out that the "surface divergence" physically is the signature of turbulent "sweep" events representing local "upwelling" motions at the surface from the bulk fluid. On the other hand, it is an alternative expression of the

surface renewal and more specifically modeled by tangential components of velocities at the interface. *Csanady* [1990] emphasized the role of breaking wavelet at the interface with high surface divergence by squeezing DBL due to "upwelling" motions, i.e., the disturbance of DBL by turbulent eddies is enhanced during micro-wave breaking events. Recently, surface divergence has been shown to correlate with interfacial gas transfer process in laboratory studies [*Asher et al.*, 2012; *McKenna and McGillis*, 2004].

One advantage of the "surface divergence" model is that it can be easily implemented: (1) concept of "surface divergence" replaces the renewal time scale by velocity fluctuating motions, while the renewal time varies due to different environmental flow conditions (2) "surface divergence" is easier to measure than the renewal time (e.g. through the surface PIV measurement using infrared imaging techniques at the water surface [*Asher et al.*, 2012]).

2.2 Measurement techniques on interfacial gas transfer

Considering the fact that the interfacial gas transfer is ultimately limited by the very thin layer of DBL (on the order of micrometers), existing measurement technologies are not direct measurement of the gas transfer velocity across the air-water interface. Most measurement techniques applied are indirect methods, e.g., measuring a designed tracer flux across the air-water interface then converting it to the gas of interest assuming that both are controlled by the near surface turbulence then the transfer velocity is scaled by the molecular diffusivity (i.e. equation (5) in surface renewal model).

2.2.1 Deliberate volatile trace experiments

Inert volatile tracers have been widely used in determining gas transfer velocities in field studies through a mass balance approach. For example, sulfur hexafluoride (SF_6) was deliberately added to water bodies to quantify the gas transfer velocity as a function of wind speed [*Clark et al.*, 1995; *Upstill-goddard et al.*, 1990; *R Wanninkhof et al.*, 1985; *R Wanninkhof et al.*, 1987; *R H Wanninkhof and Bliven*, 1991], since it can be detected at a very low levels in water with an excellent signal-to-noise ratio. Based on mass balance approach, gas transfer velocity can be determined,

$$k \approx \frac{h}{t_2 - t_1} \ln \frac{C_{wt_1}}{C_{wt_2}} \tag{16}$$

where C_{wt} is concentration of released tracer in water at time t. h is the mean depth of mixed layer. Originally, the tracer experiment was designed for closed lakes with relatively small size [*Clark et al.*, 1995]. The experiment time scale is on the order of days to weeks depending on the size of lakes. However, for a large lake or ocean, the concentration of tracer decreases quickly due to horizontal transport and dispersion. Meanwhile, the mixing layer depth may vary significantly in space as the surface area and volume exposed to the atmosphere increases due to dispersion effect.

The tracer method can be improved by co-releasing a second inert tracer with a different diffusion coefficient (e.g. ^3He). By releasing two tracers with a constant ratio, the decreases of concentration due to dispersion are the same for the two gases, but different due to interfacial exchange. Since the transfer velocity should differ by a factor of 3, as $Sc(^3He)$ is about eight times smaller than $Sc(SF_6)$, the effect of horizontal

dispersion can be separated out. The dual tracer technique has been used to measure gas exchange in different water bodies [*Ho et al.*, 2006a; *Ho et al.*, 2011b; *R Wanninkhof et al.*, 2004; *Watson et al.*, 1991]. Besides dual tracer technique, a third nonvolatile tracer (e.g. bacterial spores and rhodamines) can also be introduced to determine the gas transfer velocity independently based on an arbitrary tracer pair [*Nightingale et al.*, 2000].

2.2.2 Active controlled flux technique (proxy technique)

The active controlled flux technique (ACFT) is a method to quantify the gas transfer velocity through the analogy with the heat transfer across the air-water interface [*Haußecker and Jähne*, 1995; *Haußecker et al.*, 1995]. One example is to use an infrared laser to heat a certain area of water surface. A sensitive infrared imager is used to capture the time series of images of the heated patch on water surface. In order to determine the renewal frequency *f*, the "surface renewal model" is employed to fit the observed average surface temperature decay curve. The transfer rate of heat can be calculated as,

$$k_H = \sqrt{D_H f} \tag{17}$$

where D_H is thermal conductivity of water. Thus, gas transfer velocity can be estimated as,

$$k_G = k_H \left(\frac{Sc}{\mathrm{Pr}} \right)^{-n} \tag{18}$$

where *Sc* is Schmidt number of gas of interest and Pr is Prandtl number defined as $\mathrm{Pr} = \nu / D_H$, the exponent *n* varies in the range between 1/2 and 2/3 depending on the roughness of water surface [*Jähne and Haußecker*, 1998; *Jähne et al.*, 1987]. Using this

technique, *Garbe et al.* [2004] have experimentally demonstrated the probability density function of the surface renewal time can be described with a lognormal distribution.

However, several experiments found that discrepancies exist between estimates of transfer velocity based on ACFT and that from dual tracers measurements [*Atmane et al.*, 2004] or direct covariance method [*McGillis et al.*, 2001; *McGillis et al.*, 2004]. *Atmane et al.* [2004] found gas transfer velocity (as referenced to *Sc* = 600) determined by ACFT (using heat as proxy) was overestimated by a factor of 2, approximately.

The discrepancy can be attributed to the fact that the random eddies might not take effect on heat and gas exchange equally through renewal events. The *Sc* number is typically much greater (e.g. Sc(CO_2) is 600 at 25 ℃ in fresh water) than the Pr (e.g. Pr is around 7 at 20 ℃ in water) number, hence the thickness of the gas DBL is significantly smaller than that of the TBL. Some of the "upwelling" eddies might not approach the gas DBL but they can disturb the TBL effectively. *Asher et al.* [2004] proposed a different scaling with *Sc* number and explain the solution to the problem by using the surface penetration model. *Atmane et al.* [2004] argued that the eddy approach distance need to be included as an extension to the surface renewal model.

2.2.3 Eddy covariance (correlation) method

The vertical flux of the scalar of interest (e.g. temperature, moisture, CO_2 concentration) can be estimated by evaluating the covariance between the fluctuating vertical velocity component and the fluctuating scalar concentration measured simultaneously at a certain height above the air-water interface. With the method,

horizontal homogeneity is assumed and Reynolds decomposition is applied. The "eddy flux" is written as,

$$F = \overline{w'c'} \tag{19}$$

where *w'* and *c'* are fluctuation of vertical velocity and concentration.

In order to apply the eddy covariance method, fast response instrumentations are required to capture the high frequency fluctuation of gas concentration and turbulent flow, as measuring gas transfer across the air-water interface. The eddy covariance method has been applied to measure the air-sea CO_2 flux from the air side [*Edson et al.*, 1998; *McGillis et al.*, 2001] and DO (Dissolved Oxygen) flux from the aqueous side [*Chu and Jirka*, 1992]. Applying eddy covariance method from the air side on the open ocean can be challenging due to the distortion of flow induced by the movement of ship-based platform and the uncertainty of gas concentration due to changes in air density caused by variations in temperature and water vapor known as the Webb effect [*Webb et al.*, 1980].

Alternative to the eddy covariance method, a relaxed eddy accumulation (EA) method [*Businger and Oncley*, 1990; *Zemmelink et al.*, 2004; *Zemmelink et al.*, 2002] was developed and employed to estimate the gas flux by separating measurement of gas concentration from updrafts and downdrafts. This method avoids the requirement of high frequency measurement on the fluctuating gas concentration.

Recently, measurements of turbulent flux with particle image velocimetry (PIV) and laser induced fluorescence (LIF) techniques [*Herlina and Jirka*, 2004] were conducted in a grid stirred tank. *Herlina and Jirka* [2008] suggested that the gas transfer at different turbulent levels can be associated with different dominant eddy sizes

according to the spectra of covariance terms, which agreed with the "two regime" theory [*Theofanus et al.*, 1976].

In the field, eddy covariance method has been widely applied to measure DO flux across the water-sediment interface [*Berg et al.*, 2003; *Berg et al.*, 2009]. Recently, a waterside direct covariance measurement [*D'Asaro and McNeil*, 2007] has also been conducted in the field to investigate the air-sea gas exchange under extreme wind speed conditions. Although the requirement of high sampling rate can be relaxed due to longer time and length scales of turbulence on the waterside than the air side, the isotropic turbulence assumption still needs to be invoked and justified.

2.2.4 Floating chamber measurements

Gas flux across the air-water interface can also be estimated by monitoring the buildup of gas emitted into a floating chamber (FC) [*Frankignoulle*, 1988] over a certain period of time. *Kremer et al.* [2003] suggested that FC method would be applicable for low to moderate wind conditions (less than 8-10 m/s) and with a limited fetch such that waves are young and nonbreaking. An ideal chamber should have a large ratio of water surface area to chamber volume. *Matthews et al.* [2003] compared the CO_2 and CH_4 fluxes based on the FC method, tracer technique and wind dependence estimation. The result showed that the FC method overestimate the transfer velocity in low wind shear condition. *Guerin et al.* [2007] conducted FC measurements in reservoirs and rivers, which gave similar results with the eddy covariance technique. FC method was also applied in coastal regions [*Tokoro et al.*, 2007] under low to moderate wind (<10 m/s)

and weak current condition (<20 cm/s). The results showed overestimation on transfer velocity compared with wind dependent relationship. *Vachon et al.* [2010] tested the FC method with dissipation rate measurement. The results showed that the artificial effect of FC on near surface turbulence depends strongly on the background turbulence level, that is, overestimation by FC method is relatively large in a low turbulence environment.

2.3 Driving forces and parameterizations

2.3.1 Wind speed

Most experimental work and modeling on gas transfer velocity are based on wind speed measurements and parameterization. Although it is not a direct driving force on interfacial gas transfer, wind stress has been considered as the primary source of near surface turbulence. Overall, wind speed is a reliable parameterization variable and is found to agree well with experimental data on gas transfer velocity. The advantage of wind speed models is that wind speed can be easily measured or obtained through meteorological modeling or remote sensing thus it can be easily implemented into regional and global gas flux estimations.

Although accurate wind speed measurement is rather difficult [*Frost and Upstill-Goddard*, 2002; *Nightingale et al.*, 2000; *Upstill-Goddard*, 2006; *M J Yelland et al.*, 1998], a large amount of laboratory and field experiments [*Frost and Upstill-Goddard*, 2002; *Liss*, 1983; *Liss and Merlivat*, 1986; *Merlivat and Memery*, 1983; *Nightingale et al.*, 2000; *R Wanninkhof*, 1992; *R Wanninkhof and McGillis*, 1999; *R Wanninkhof et al.*, 1993;

R H Wanninkhof and Bliven, 1991] have been conducted to estimate the empirical relationship between wind speed and gas transfer velocity and they are summarized in the following.

The first wind speed model was presented by *Liss and Merlivat* [1986]. A "three linear segments" relationship between the gas transfer velocity and the wind speed was proposed based on wind tunnel experiments. The three segments were categorized according to the surface roughness (smooth surface,U_{10}< 3.6 m/s; rough surface, 3.6 m/s <U_{10}< 13 m/s; breaking wave region,U_{10}> 13 m/s).

Up to the present day, the most popular wind speed based gas transfer model is a quadratic relation. *R Wanninkhof* [1992] suggested that gas transfer velocity scales with U_{10}^2 [*R H Wanninkhof and Bliven*, 1991] based on global bomb ^{14}C constraint [*W S Broecker et al.*, 1985] and wind wave tank results. The quadratic relation indicates that the gas transfer scales with wind stress as $\tau \sim C_D U_{10}^2$. The quadratic relationship [*R Wanninkhof*, 1992] for gas transfer velocity of CO_2 at 20 ℃ for seawater (Sc = 660) is written as

$$k_{660} = 0.39\langle U_{10} \rangle^2 \tag{20}$$

where the transfer velocity is expressed in "cm/hour" and wind speed is in "m/s". Furthermore, *R Wanninkhof* [1992] modified the scaling factor for the cases of short-term or steady wind conditions,

$$k_{660} = 0.31\langle U_{10} \rangle^2 \tag{21}$$

Similar quadratic relationship was derived by *Nightingale et al.* [2000] from deliberate tracer experiments in the coastal ocean:

$$k_{660} = 0.222U_{10}^2 + 0.333U_{10} \tag{22}$$

This result is in between the model of *Liss and Merlivat* [1986] and that of *R Wanninkhof* [1992]. Recently, the SOLAS Air-Sea Gas Exchange (SAGE) experiment was conducted in the Southern Ocean [*Ho et al.*, 2006a]. The new quadratic relationship is given from dual tracer injection experiments as

$$k_{660} = (0.266 \pm 0.019)U_{10}^2 \tag{23}$$

More recently, additional dual tracer experiments were conducted in Southern Ocean [*Ho et al.*, 2011c]. From the new data, the relationship [*Ho et al.*, 2011b] was updated to,

$$k_{660} = (0.262 \pm 0.022)U_{10}^2 \tag{24}$$

Alternatively, a cubic relation was proposed by *R Wanninkhof and McGillis* [1999] for steady or short term wind conditions,

$$k_{660} = 0.0283U_{10}^3 \tag{25}$$

This relation is in good agreement with direct covariance results of air-sea Gas Exchange Experiment conducted in 1998 (GasEx-98). The cubic relation is supported by GasEx-98 data [*McGillis et al.*, 2001] and GasEx-2001 data [*McGillis et al.*, 2004] in the following expressions,

$$k_{660} = 0.026U_{10}^3 + 3.3 \tag{26}$$

$$k_{660} = 0.014U_{10}^3 + 8.2 \tag{27}$$

Although wind speed parameterization is probably the most convenient and a successful model [*Takahashi et al.*, 2002] for estimating interfacial gas transfer velocity, the method is largely empirical. Most supporting data came from local experiments,

which could be affected by many factors (such as the experiment location, measurement techniques, instrumentation errors and experimental uncertainties). *Ho et al.* [2006b] argued that the experiments of *Nightingale et al.* [2000] might be affected by an underdeveloped wind field and higher concentration of surfactants in coastal area. And the result of *R Wanninkhof* [1992] is most likely an overestimate because of an excessive ^{14}C inventory of the global ocean.

If the wind speed model were to apply to estimate the global CO_2 uptake by oceans, the global wind speed estimate would be a very critical issue. The total fluxes estimation is very sensitive to the accuracy of global wind speed estimation [*Boutin et al.*, 2002; *Naegler et al.*, 2006]. *R Wanninkhof et al.* [2009] pointed out since the long term averaged transfer velocity essentially scales with the second or third order of moment of the wind speed, the quadratic relationship gives a 27% higher result compared with the short term estimation while the cubic relationship gives a 91% higher result. It should be noted that the global wind speed distribution can be approximately represented by a Rayleigh distribution [*R Wanninkhof*, 1992; *Wentz et al.*, 1984].

2.3.2 Wind stress

In general, the relation between gas transfer velocity and wind speed can be summarized as,

$$k \sim Sc^{-n} U_{10}^{b} \tag{28}$$

where b = 1, 2, 3, representing linear, quadratic, cubic relations with respect to the wind speed. According to Charnock's Law [*Charnock*, 1955],

$$\frac{U(z)}{u_{*a}} = \kappa^{-1} \ln\left(\frac{gz}{u_{*a}^2}\right) + C \tag{29}$$

where κ is von Kármán's constant. Meanwhile the surface shear stress caused by wind can be related to the wind speed as,

$$\tau = \rho_a C_D U_{10}^2 \tag{30}$$

where C_D is the wind drag coefficient, which is also a function of U_{10} [*Large and Pand*, 1981; *M Yelland and Taylor*, 1996]. If one applies the continuity of shearing stress at the interface,

$$\tau = \rho_a u_{*a}^2 = \rho_w u_{*w}^2 \tag{31}$$

So the relation among the wind speed and friction velocities of the air and water sides can be ,

$$U_{10} \sim u_{*a}^{\alpha} \sim u_{*w}^{\alpha} \tag{32}$$

where α depends on the scaling of the drag coefficient with the wind speed. Many experimental results suggested that the drag coefficient increases linearly with wind speed except for the case of low wind speed, so α= 1/2 can be derived [*Anderson*, 1993; *Geernaert et al.*, 1988; *Large and Pand*, 1981; *Smith et al.*, 1992; *M Yelland and Taylor*, 1996]. Also since the quadratic law is the most widely accepted wind speed model for gas transfer velocity, i.e., b = 2 in equation (28), the gas transfer velocity is linearly scaled with the water side shear velocity,

$$k \sim Sc^{-n} u_* \tag{33}$$

For most wind speed models, the power of Schmidt number $-n$ is typically set to be -1/2, then have,

$$k \sim \sqrt{D} \tag{34}$$

which is consistent with the surface renewal model (equation (4)).

On the other hand, *Jähne and Haußecker* [1998] show that the gas transfer velocity can be expressed explicitly by interfacial shear velocity though turbulent diffusive boundary layer theory:

$$k \sim u_* Sc_t \tag{35}$$

where Sc_t is the turbulent Schmidt number, defined as the ratio of turbulent diffusion coefficient of momentum and gas concentration:

$$Sc_t = \frac{K_m}{K_c} \tag{36}$$

Using the concept of diffusive boundary layer *Deacon* [1977] proposed that,

$$k = 0.082 Sc^{-2/3} u_{*w} \tag{37}$$

which shows that gas transfer velocity is proportional to interfacial shear velocity.

The relation derived from diffusion boundary layer theory is also similar the equation (33), which is derived from the empirical wind speed model (quadratic relation). The difference is the exponent of the Schmidt number. In *Deacon* [1977]'s model, the -2/3 power scaling is suitable for smooth surface, as it is pointed out by *Jähne and Haußecker* [1998]. The -1/2 power scaling is more appropriate for a wave-covered water surface [*Jähne et al.*, 1987]. *Fairaill et al.* [2000] conducted a comprehensive analysis on a number of parameters including effects of shear forcing, roughness Reynolds number and buoyancy effects on the gas transfer. Their results have been applied by *Hare et al.* [2004] to evaluate the GasEx data. And they found significant gas flux occurs due to wave breaking and air bubble entrainment, which will be discussed in the next section.

2.3.3 The effect of sea surface roughness, wave breaking and entrained air bubbles

Experiments confirmed that gas transfer is enhanced by the presence of wind induced ripples. From the perspective of momentum transport, turbulence can be enhanced by the increase of surface roughness. The exponent of the Schmidt number in wind speed models or wind shear models varies from about -2/3 to -1/2, which was found to be dependent on the surface roughness. For CO_2, that implies a variation in the transfer velocity by a factor of 3. *Jähne et al.* [1987] demonstrated a good correlation between the gas transfer velocity and the mean square slope of surface waves in a wind/wave facility. *Frew et al.* [2004]'s field experiments shows stronger correlation between the transfer velocity and the mean square slope compared to wind speed relation. Since the wave slope can be obtained through satellite-base remote sensing, this relation provides a method can be easily implemented to estimate the global gas flux [*Frew et al.*, 2007].

The majority of laboratory and field experiments on gas transfer were conducted under weak to moderate wind conditions. Extremely high wind speed makes the measurement very difficult. From the few existing data, the transfer velocity is significantly enhanced in high wind fields. The accepted theory is that the gas flux across the interface is dominated by wave breaking and entrained air bubbles [*Asher et al.*, 1996; *Farmer et al.*, 1993; *Kitaigorodskii*, 1984; *McNeil and D'Asaro*, 2007; *Merlivat and Memery*, 1983; *Zhang et al.*, 2006]. *Woolf and Thorpe* [1991] argued that the transfer velocity is only enhanced by bubbles for very low soluble gases. *Woolf* [1993] introduced

a transfer velocity term which is specifically due to bubbles. Thus the transfer velocity can be expressed by a hybrid model [*Woolf*, 2005],

$$k = k_0 + k_b \tag{38}$$

where k_b is approximately proportional to the whitecap coverage [*Woolf*, 1997]. Factors that influence bubble mediated transfer were reviewed by *Woolf* [1997] and *Woolf et al.* [2007]. Alternatively, other parameterizations and analyses on gas transfer velocity through the whitecap coverage exist [*R Wanninkhof et al.*, 1995; *Zhao et al.*, 2003].

2.3.4 The effect of surfactants

The presence of surfactants is believed to have an attenuation effect on interfacial gas exchange. The early laboratory experiments observed a large amount of reduction of transfer velocity due to the presence of surfactants [*H C Broecker et al.*, 1978]. *Asher* [1997] reported a linear relationship between the transfer velocity and wind speed at the presence of surfactant when wind speed is smaller than 12.5 m/s.

Numerous studies of the effects of surfactants on air-sea gas transfer have been conducted in laboratory settings and *in situ* [*Asher and Pankow*, 1986; *McKenna and McGillis*, 2004; *Saylor et al.*, 2000; *Tsai*, 1996a; b; *Tsai and Yue*, 1995; *Tsai and Liu*, 2003]. Some of surfactants are soluble, while others are not. The insoluble surfactant acts as a barrier film. However, this effect can be easily dispersed by wind and waves. For high wind conditions, the soluble surfactants are believed to have a prevailing effect on gas transfer even at the presence of breaking waves, while insoluble surfactants do not [*Bock et al.*, 1999; *Frew et al.*, 1990; *Goldman et al.*, 1988].

2.3.5 The effect of rainfall

Air-sea gas exchange during rainfall events has been brought into attention recently. It has been shown that rainfall will enhance the transfer velocity across the interface [*Frost and Upstill-Goddard*, 2002; *Ho et al.*, 1997; *Ho et al.*, 2007; *Ho et al.*, 2004; *Zappa et al.*, 2009]. Existing evidence shows that the enhancement is due to rainfall generated turbulence and bubble entrainments. The kinetic energy flux (KEF) caused by raindrops has been introduced to scale with the gas transfer velocity [*Ho et al.*, 1997; *Ho et al.*, 2000]. However, *Takagaki and Komori* [2007] argued that transfer velocity is more correlated with the momentum flux of rainfall (MF).

The effect of raindrops on the enhancement of surface mixing, damping waves and changing the air-sea momentum flux has been investigated through the surface renewal model [*Schlussel et al.*, 1997]. Rainfall could also induce surface density stratification and additional surface heat flux because of temperature difference between raindrops and the sea surface. The combined effect of rainfall and high wind speed is believed to have a significant impact on air-water gas exchange, however, this effect is complex and yet to be investigated comprehensively.

2.3.6 Near surface turbulence

The parameterizations of interfacial gas exchange discussed above are generally empirical or semi-empirical. For most empirical models, gas transfer velocities are scaled with meteorological parameters such as wind speed, wind shear, momentum flux

or kinetic energy flux induced by rainfalls (rainfall dominant environment), etc. In comparison, models based on near surface turbulence structures, such as the surface renewal model and the surface divergence model, are more mechanistic. For gases with low solubility, the resistance of gas transfer is dominated by the water side, which is in turn controlled by the near surface turbulence.

A large amount of experiments was conducted to investigate the near surface turbulence and its relation to air-sea gas transfer process. *Lamont and Scott* [1970] presented an eddy cell model to quantify the mass transfer from the hydrodynamic parameters (equation (12)). Some recent studies show the gas transfer velocity is better scaled with the surface turbulence [*Asher and Pankow*, 1986; *Zappa et al.*, 2003; *Zappa et al.*, 2009]. *Zappa et al.* [2007] has shown that gas transfer velocity is well correlated with the dissipation rate rather than wind speed under a variety of environmental forcing, regardless the how the near surface turbulence was produced. *Vachon et al.* [2010] performed a number of measurements to demonstrate direct relationship between gas transfer velocity (measured by a floating chamber) and near surface turbulent dissipation rate (measured by an ADV). *Lorke and Peeters* [2006] demonstrated that equation (12) can be derived by assuming the thickness of diffusive sub-layer to be scaled with the Batchelor's micro-scale,

$$\delta_D = L_B = 2\pi\left(\frac{\nu D^2}{\varepsilon}\right)^{1/4} \tag{39}$$

It is worth noting that the dissipation rate scaling is based on the assumption of homogenous and isotropic turbulence near the water surface. Correspondingly, the small eddy model is applicable for a high Reynolds number condition, which is the prerequisite of the Kolmogorov's similarity hypothesis.

Despite the promising results from small scale eddy models, the scaling coefficient has not been clearly determined yet. In most of these studies, the coefficient is usually obtained empirically from fitting modeled transfer velocities with measured ones. Another uncertainty is associated with the depth at which the dissipation rate should be applied in the model. In theory the dissipation rate should be measured immediately below the air-water interface, but this cannot be easily achieved during field measurements. While there is very few *in situ* data available for the near surface turbulence, existing field data was obtained at a short distance (tenth of centimeters) away from the wavy surface. *Zappa et al.* [2007]argued that this might not be a serious issue, as the gas transfer velocity should scale with $\varepsilon^{1/4}$. However, if a strong gradient of dissipation rate exists near the surface, this assumption has to be examined carefully.

2.4 Summary

Gas transfer across the atmosphere/ocean interface is a very important physical process that regulates the global climate, considering the fact that this process occurs over an area that is about 70% of the Earth surface. This chapter provides a review on the current technologies of measuring the gas flux across the air/ocean surface and existing models for the gas transfer velocity. Many environmentally important gases, such as O_2 or CO_2, have a low solubility, so the major resistance of gas exchange is from the water side. Near surface turbulence might be the key physical parameter that determines the gas transfer velocity as it controls the thickness of the diffusive boundary layer, e.g., "eddy" upwelling induced surface renewal. Global gas flux estimates still use the wind

speed, or wind shear stress as the primary modeling parameter, as wind is the major source of near surface turbulence. For example W92 model is commonly applied to estimate the global air-sea CO_2 flux. Additionally, breaking wave parameters such as the whitecap coverage, are also included to account for gas exchange through bubbles induced by breaking waves. Other environmental forcing may also be significant sources of near surface turbulence that can affect the gas flux. Turbulence can be generated by bottom mixing then diffuses to the surface in a coastal area; turbulent buoyant convection, surface currents, precipitation and micro-breaking of short surface waves can also contribute to near surface turbulence production. These parameters are usually not directly related to the wind stress.

Recent studies indicated that small scale eddy models parameterized with the surface dissipation rate or divergence are more mechanistic thus universal approach to estimate the gas transfer velocity under a wide range of environmental forcing conditions, except for the case of breaking waves. In this thesis, I provide encouraging opportunities to quantify the structure of turbulence in the upmost layer below the air-sea interface.

Chapter 3

A Free Floating PIV system: Measurement of Small – Scale Turbulence under the Wind Wave Surface

3.1 Instrumentation

An *in situ* UnderWater Miniature PIV (UWMPIV) system has been recently developed and successfully deployed to characterize the hydrodynamics of the bottom boundary layer of Lake Michigan [*Liao et al.*, 2009]. Following this, a second generation UWMPIV was developed for high speed flow measurement with a Dual-Beam-Dual-Camera configuration [*Wang et al.*, 2012]. The current design of the UWMPIV is flexible. Primarily, it consists of three submersible units: 1) a laser unit with one or two continuous wave (CW) DPSS lasers and a galvanometer (scanning mirror) that scans the laser beam(s) into an effective laser "sheet"; 2) a camera unit with a CCD camera, a compact computer for streaming image data and a signal control unit; and 3) a power-

supply unit that contains high-capacity lithium-ion batteries. The power consumption of the entire system is about 30 W when running at the full rate.

In order to construct a floating PIV system, the three units are mounted on a platform built with iron pipes and Kee Klamp® adapters. The laser unit is allowed to slide along the direction of the optical axis of the camera to achieve the desired field of view (FOV) and to adjust the focus. Floating fenders are attached at the two ends of the frame to keep the system free-floating on the water surface (figure 3-1). In addition, a wireless router with an amplification antenna is placed on top of the system to provide an ad-hoc Wi-Fi network so the UWMPIV system can be remotely controlled during deployment. A black plastic plate is mounted at the tail end of the frame, behind the FOV of the camera. The plate is designed with two purposes: 1) to block background sunlight from entering the camera lens directly, 2) to guide the floating system so that the FOV of the camera is approximately parallel to the mean current direction or the wave propagation direction, thereby minimizing the out-of-plane motion of particles. Also, according to observation during deployments, the guide plate helps to orient the platform such that flow disturbance generated by the frame and the camera housing is not propagated into the laser "sheet". Preliminary tests with moderate wave conditions (significant wave height < 0.4 m) showed that the floating UWMPIV could move up and down with the undulating water surface, such that the air-water interface is visible in most if not all images acquired. These tests also indicated that, for some cases, the location of the water surface can be automatically tracked through ad-hoc image processing algorithms.

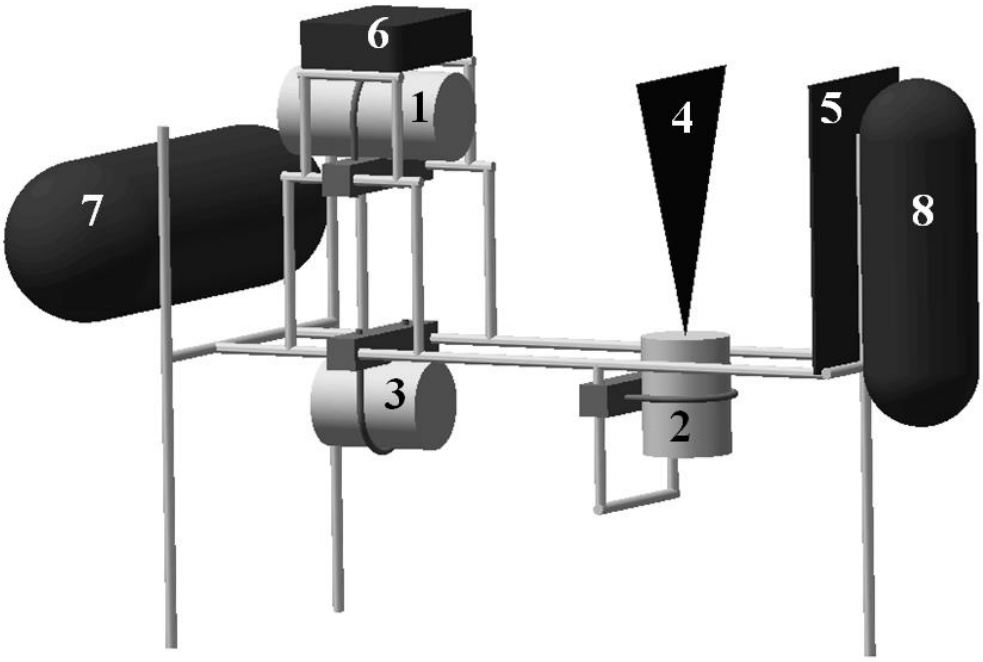

Figure 3-1. The free-floating UWMPIV. 1: camera housing; 2: laser housing; 3: battery housing; 4: effective" laser sheet; 5: guide plate; 6: wireless router; 7: tail fender; 8: head fender.

3.2 Deployment

The free-floating UWMPIV is designed to measure the surface boundary layer under low to moderate wind conditions. The objective is to reveal the structure of turbulence beneath the water surface. Under high wind wave conditions, air bubbles entrained may significantly "contaminate" PIV images and thus invalidate velocity measurements. The preliminary tests have proved that successful measurements can be made under a wavy water surface in the absence of "white caps". Microscale wave breaking associated with high vorticity near the water surface can be clearly observed.

To quantify the flow structure during the wind wave generation phase, five experiments (denoted as runs 1 ~ 5) were conducted in the Milwaukee Harbor (Lake Michigan), with a nearly zero-fetch condition. A variety of wind forcing conditions were selected for field experiments from August to November of 2011, with the wind speed ranging from 1 to 15 m s^{-1}, and the significant wave height ranging from 2 to 9 cm. A summary of environmental conditions and experimental parameters for the 5 experiments is given in Table 1. Wind speed and direction were obtained from a wind sensor installed on the top of a building situated near the experiment site (within 50 meters). The height of the wind sensor was about 10 m above the water surface. Parameters for PIV measurements, including the camera FOV, sample frequency, and laser beam sweeping time, were selected to attain the best image quality. One experiment was also conducted on open Lake Michigan (run 6). In this case, the wind speed was relatively low (2~3 m s^{-1}), and the wave age was fairly old ($c_p / u_{*a} \approx 39$). The water depth was about 10 meters, and the significant wave height was about 35 cm. The near surface current was about 6 cm s^{-1} as estimated from the drifting speed of the floating platform.

For each run 2-4 sets of images were acquired. Each data set consisted of 2000 ~ 3000 images pairs at a rate of 6-12 Hz, which corresponded to a measurement duration of about 10 - 15 minutes per set. For runs 1~4 and 6, no significant difference was found among statistics of turbulence calculated for each dataset, hence only one set was reported here. For run 5, many PIV images were contaminated by entrained bubbles, hence one set with the best image quality for this run was reported.

3.3 Effects of platform motion on turbulence measurements

The PIV system is free-floating and moves with the waves, currents, and large "eddies" near the surface. Therefore it is not able to measure absolute velocities of the flow field. Smaller turbulent "eddies" that are comparable in size with the FOV of PIV images (~10 cm) usually do not have adequate energy to significantly affect the motion of the platform. Visually, no vibration caused by near surface turbulence was observed. Therefore, the measured velocity field is a combination of the real flow and the apparent velocity induced by the solid-body movement of the platform relative to the water. Since the purpose of the free-floating UWMPIV system is to measure the turbulence structure near the water surface represented by vorticity, rate-of-strain, or dissipation rates which are calculated through the gradients of fluctuating velocity components, the solid-body translation induced by the platform movement does not affect these measurements. However, the rotation (pitch and roll) of the system needs to be considered, as it does affect the calculation of velocity gradients.

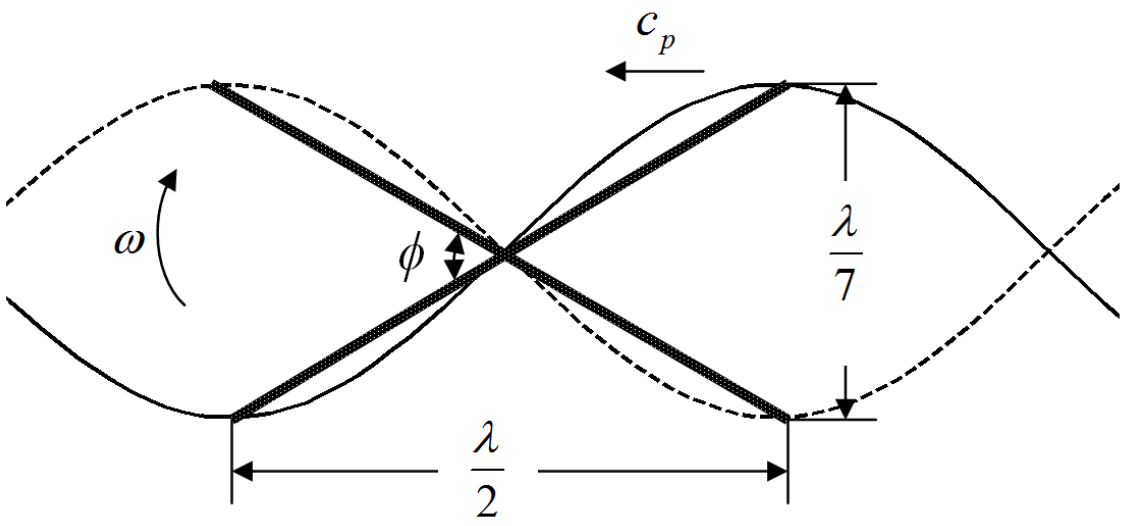

Figure 3-2. Sketch of the most severe situation when steep (near breaking) wave-induced floating platform rotation has the maximum angular speed, where c_p is the phase speed of the propagating wave, and λ is the wave length.

It should be pointed out that the impact of platform rotation is negligible under the conditions in this study, as small-scale turbulence characterized by statistics of local velocity gradients is typically dominated by intermittent peak values which are usually much greater than the angular speed of the platform rotation. This is illustrated by considering the most severe situation, in which the floating platform closely follows the surface wave. Under these conditions the maximum angular speed is expected to occur under the steepest non-breaking surface wave condition when the ratio of the wave high to wave length is approximately 1:7. In this case, the maximum rotation angle of the PIV system can be estimated as:

$$\phi = 2 \times \tan^{-1}\left(\frac{2}{7}\right) \tag{3}$$

as illustrated in figure 3-2. Meanwhile, according to the dispersion relation for deep water waves, the travel time of a half wave length can be estimated as

$$t = \frac{T}{2} = \frac{1}{2}\sqrt{\frac{2\pi\lambda}{g}} \tag{4}$$

where λ is the wave length, and T is the wave period. Thus the artificial vorticity induced by system rotation can be estimated as

$$\omega_{sys} \sim 2\frac{\phi}{t} \tag{5}$$

which is about 1.1 s^{-1} for the worst case when the wave length is about twice of the size of the floating platform (~ 3 m) while waves longer or shorter than that length will produce a lower rotational speed (i.e., smaller angle ϕ for shorter waves and long period T for longer waves). It should be emphasized that this estimate represents a "worst case scenario", and the actual platform rotational speed will likely be lower due to the inertia of the platform, i.e., it will not perfectly follow the water surface. Moreover, the directly measured vorticity was found usually to be much higher than ω_{sys} = 1.1 s^{-1} under a low to moderate wave steepness condition.

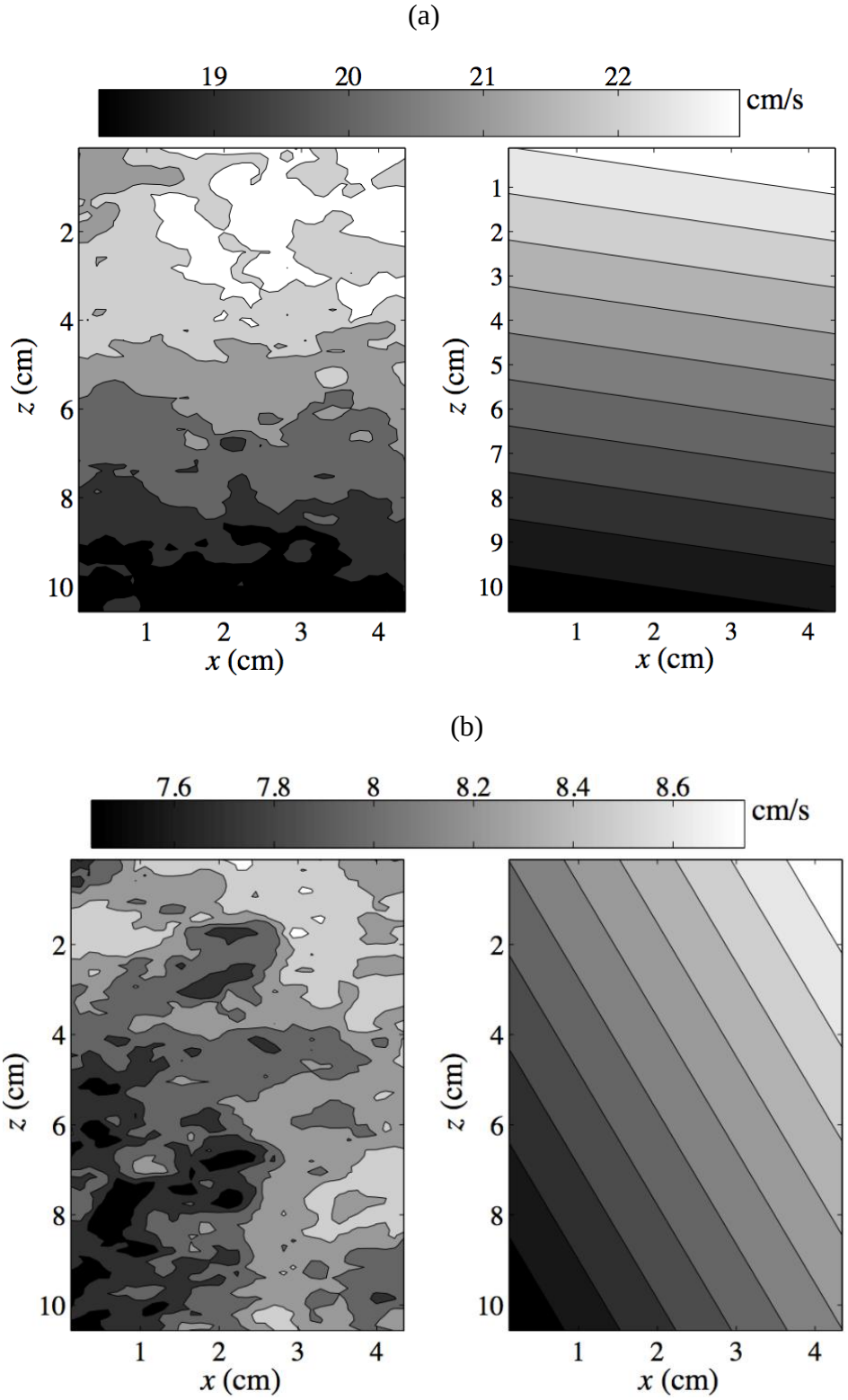

Figure 3-3. Comparison of measured instantaneous velocity field (left) and fitted velocity field (right) with a solid-body platform movement. (a) horizontal velocity component; (b) vertical velocity component.

(a)

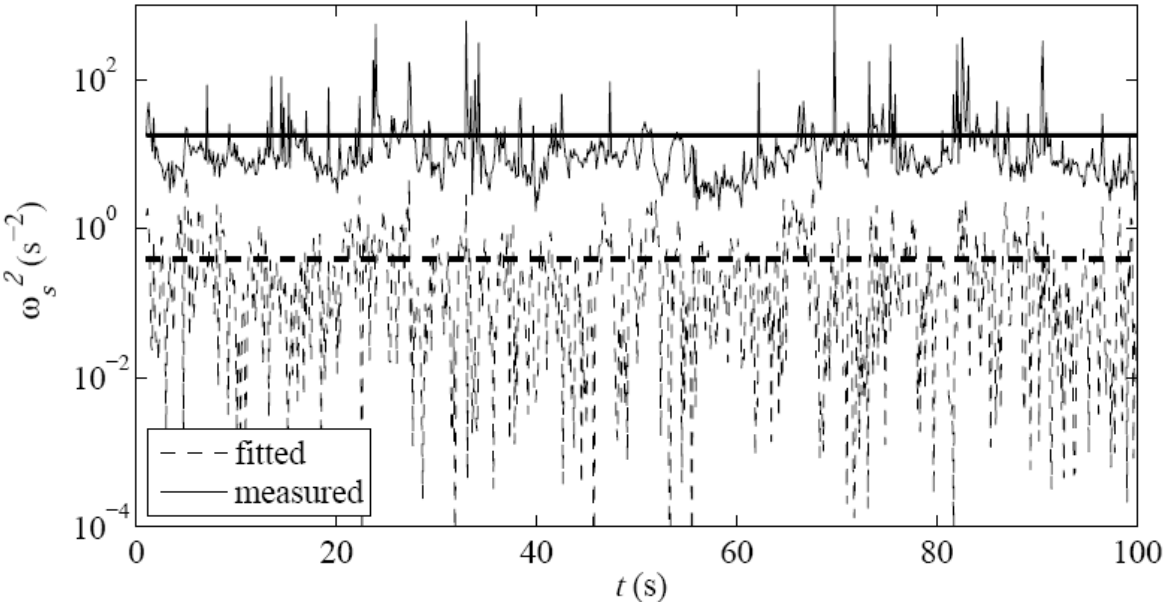

(b)

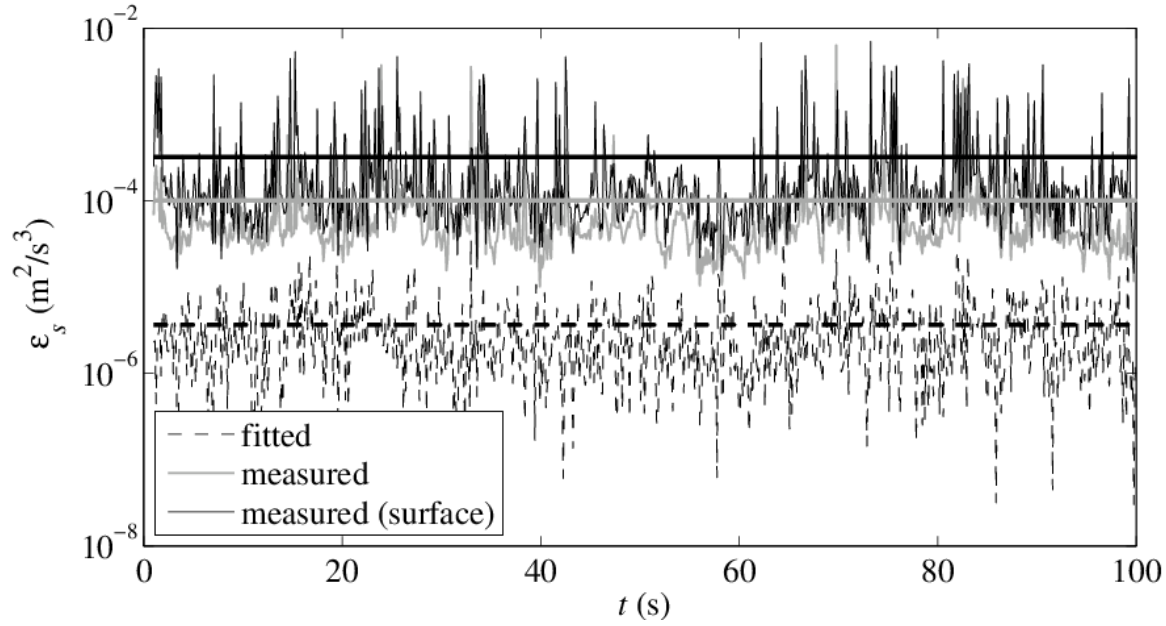

Figure 3-4. Comparison between turbulent characteristic signals of the measured velocity field and the fitted velocity field that represents the platform motion. (a) time series of the mean square of out of plan vorticity; (b) time series of the dissipation rate of TKE. Note: horizontal lines represent averages of corresponding signals.

In order to further evaluate the effect of artificial platform rotation on turbulence structure measurements, a regression analysis was performed for each measured instantaneous 2D velocity field with a velocity field reconstructed by the combination of a 2D linear translation and a solid body rotation. The reconstructed velocity field was considered as the relative velocity distribution between the system platform and the fluid. A least-square fit was applied to the measured velocity field with 5 parameters: the 2D coordinates of the center of rotation, the two translational velocity components and the angular speed. Figure 3-3 shows an example of the comparison between the measured velocity field and the fitted solid body movement velocity field. The fitted angular speed should be considered as an overestimation of the platform rotation, as it may contain swirling motion of "eddies" that are larger than the size of the FOV of the PIV image and smaller than the size of the platform. Following this step, the out-of-plane vorticities based on measured and fitted velocity fields were calculated respectively.

Figure 3-4(a) shows the time series of the mean square of the out of plane vorticity averaged over every velocity field over a 100-second period acquired during run 6 that represents the strongest platform motion among all 6 runs. As shown in figure 3-4(a), the mean square vorticity of the measured velocity field is about two orders of magnitude larger than that of the fitted velocity field representing the platform motion. Indeed, the vorticity of the fitted platform motion seldom exceeded the hypothetical worst case, i.e., $\omega_{sys} = 1.1\ s^{-1}$ (see figure 3-4(a)). The dissipation rates of TKE were also calculated for the two velocity fields (following equation (7)), and the comparison is shown in figure 3-4(b). It is evident that the artificial dissipation rate due to platform motion was on average about two orders of magnitude smaller than the directed

calculated dissipation rate. In this figure, the dissipation rate immediately below the water surface (within 2 cm) is also plotted in addition to the mean dissipation rate averaged over the entire FOV. The calculated near surface dissipation is also two orders of magnitudes higher than that of the artificial platform motion. Therefore, I can conclude that the platform motion has a negligible impact on the measurement of small-scale turbulence structures near the surface.

3.4 PIV data processing

A fundamental component of the UWMPIV system design is the laser "beam sweep" [*Gray et al.*, 1991; *Kawahashi and Hosoi*, 1989; 1991], which provides adequate particle illumination while avoiding particle image "motion blur"[*Liao et al.*, 2009; *Wang et al.*, 2012]. Longer sweeping time can increase the brightness of particle images, but at the cost of a longer time lag (Δt) between two consecutive particle exposures. For PIV interrogation analysis, larger values of Δt may cause significant loss of correlation between sub-image pairs due to the "out-of-plane" particle motion or excessive "in-plane" distortion. This problem usually becomes worse as the strength of turbulence increases. In this study, the sweeping time was carefully adjusted and tested before each deployment to achieve the best balance between the image quality and the correlation of PIV interrogation. The distance between the camera housing and the laser "sheet" was also adjusted according to water turbidity conditions to optimize clarity and focus of particles in the laser plane. Consequently, the resolution of the PIV images varies from one data set to another (see Table 1).

Table 3-1. Environmental parameter and UWMPIV parameter

Run	Start time	U_{10} (m/s)	PIV sampling rate (Hz)	Sweeping time (ms)	Resolution $(\mu m/pixel)$	FOV $(cm \times cm)$
1	08:17, Aug, 24	4.9	8	4	55	7.48×5.63
2	19:33, Sep, 26	calm	8	14	110	14.96×11.26
3	20:48, Sep, 29	10.0	6	7	110	14.96×11.26
4	21:12, Oct, 14	7.6	12	11	110	14.96×11.26
5	09:41, Nov, 3	14.3	8	4	117	15.91×11.98
6	17:44, Nov, 4	2.68	8	4	117	15.91×11.98

Figure 3-5 (a) shows a pair of sample images (Run 1). The image was constructed as the image intensity difference between one pair of images separated by Δt in time, hence a black particle image represents the exposure of the particle at an earlier time while a white particle images represent its exposure at a later time. The air-water surface was clearly visible due to the higher density of natural particles (plankton particles or micro air bubbles) at the water surface. Figure 3-5 (b-d) are sample image pairs recorded during Runs 2, 3 and 5. For runs wind speed smaller than 10 m s^{-1}, the digital signal of the surface is clear enough that it can be tracked by an ad-hoc image processing procedure: first, I divide each image horizontally into several vertical panels, and the width of each panel is set to 30~50 pixels (3~5 mm in this study). Then the image intensity is averaged over the horizontal direction for each panel to produce a mean intensity distribution along the vertical direction. A peak can be detected from the mean intensity profile, and the location of the peak intensity is considered as the surface at the central line of the panel. Any stray points due to bright large particles under the surface are filtered out. Eventually, the water surface is reconstructed through a 4th order polynomial curve fitted over these detected surface locations. The ad-hoc surface

tracking algorithm did not work well for Runs 3 and 5 since the signal of the surface was quite noisy due to the disruption of the surface at high wind speed (e.g., see Figure 3-5 (c) and (d)). For Run 5, wind shear was relatively high; wrinkles on the surface were visible in all images. Occasionally, wind gust reached >16 m s^{-1}, and small "white caps" could be observed. As a result, air bubbles were entrained below the water surface, as shown in Fig 5 (d). For these Runs, more comprehensive image-processing algorithms are needed to track the water surface automatically. In the present study, surface locations were identified manually image by image (marked and then interpolated) for Runs 3 and 5.

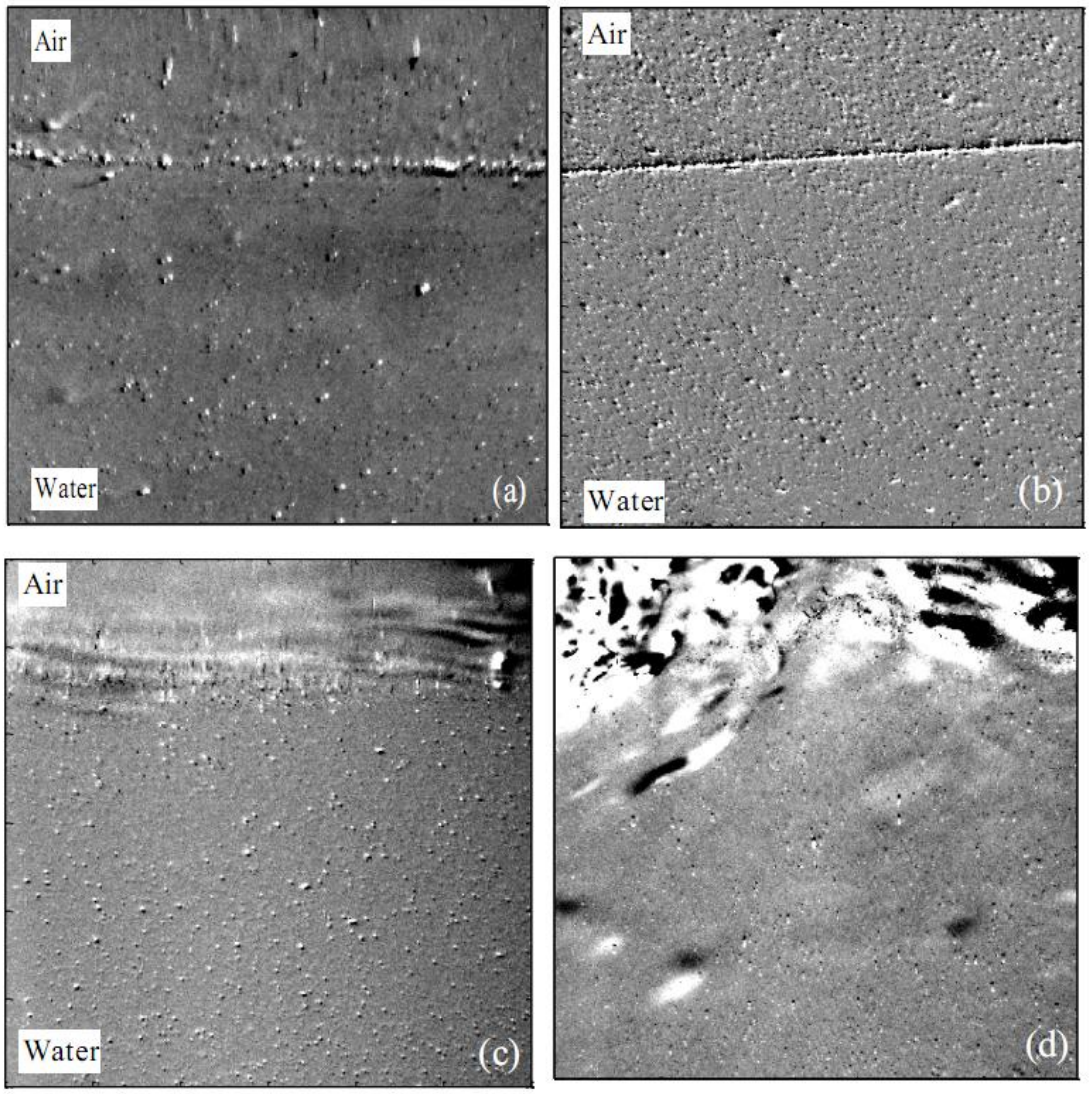

Figure 3-5. Samples of PIV image pairs (zoomed into the near-surface region). (a) Run1, a sub-window of the size 21.9 mm × 16.5 mm; (b) Run 2, 43.5 mm × 43.5 mm; (c) Run 3, 66 mm × 66 mm; (d) Run 5, 70.5 mm × 70.5 mm

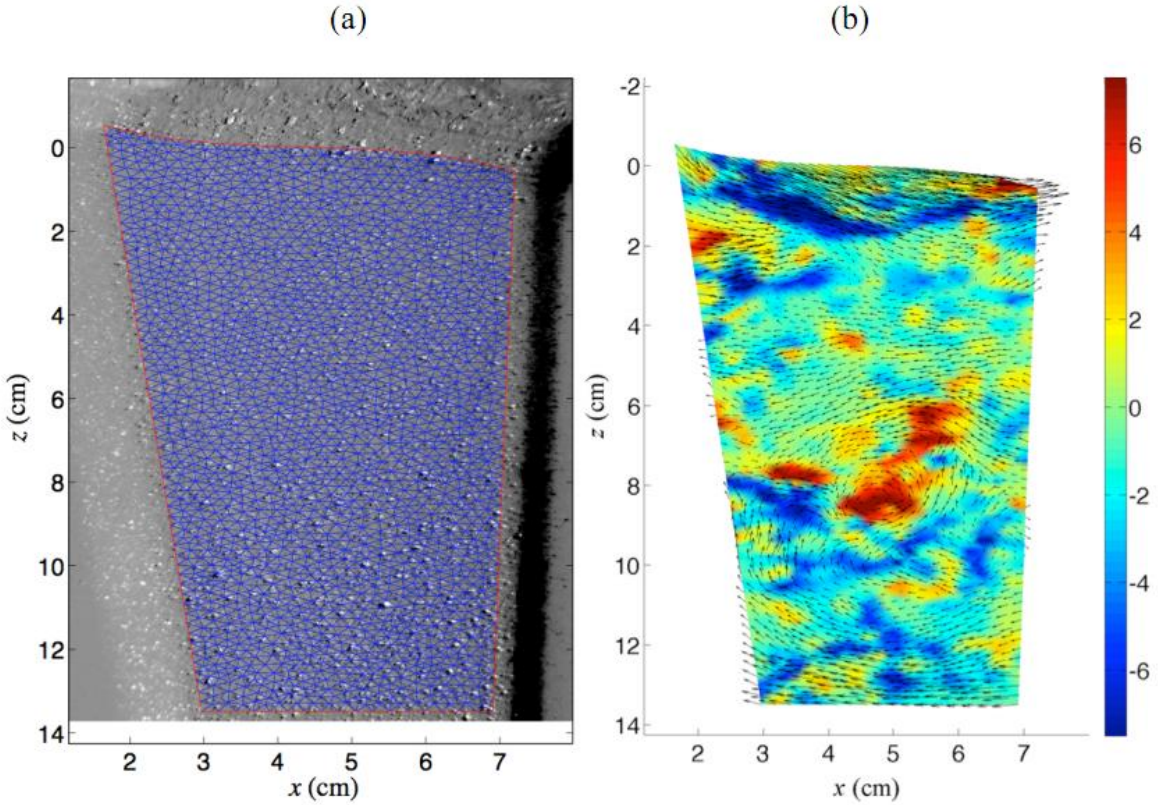

Figure 3-6. (a) A sample image pair with triangular PIV mesh; (b) The instantaneous velocity vector map superimposed on the calculated vorticity map. The unit of the color bar is (s^{-1}).

Due to the movement of the water surface within the FOV, PIV interrogation was applied on a dynamic unstructured triangular mesh. The triangular mesh is generated with the Partial Differential Equation toolbox of Matlab (Mathworks, Inc.). First, the boundary of the mesh domain was determined, which includes the reconstructed water surface and the edges of the laser "sheet". Then, a triangulation algorithm was applied to generate a mesh for the domain with a predefined nominal mesh size (15 image pixels, or 0.8~1.8 mm, depending on the actual FOV for the presented cases). Figure 3-6(a) shows an example of the triangular mesh generated for PIV interrogation. The 2-D velocity

component was evaluated at each grid node using an in-house Matlab program based on the PIV interrogation algorithm developed by *Liao and Cowen* [2005]. The PIV interrogation algorithm is a multi-pass procedure, and the sub-window size of the final pass being used was 24 × 24 image pixels, or 1.1 × 1.1 ~ 2.3 × 2.3 mm physically for the cases presented here.

Figure 3-6 (b) shows a sample of PIV interrogation results (obtained in run 6, the open water experiment), with an instantaneous out of plane vorticity map superimposed on the instantaneous velocity vector field. In this example, the spatially averaged velocity components over the mesh domain are subtracted from the instantaneous velocity to reveal vortex structures. Further statistical analysis shows that higher vortex intensity was usually observed close to the wavy water surface, while the frequency of occurrence and the intensity of vortice structures decreased away from the water surface. Occasionally, strong vortices can be observed at relatively deeper positions, which might be the result of vortex production and transport by the wave orbital motion. In laboratory studies conducted by *M H K Siddiqui and Loewen* [2007], the vorticity magnitude above a certain threshold value was considered as an index of the occurrence of microscale breaking events.

For statistical analysis, velocity maps evaluated on the triangular mesh were interpolated onto a fixed structured mesh with the top boundary always aligned with the moving water surface. By doing so, I define the vertical coordinate $z = 0$ at the surface, with z increasing downward with depth. A large number of PIV maps (1000~2000 image pairs) were sampled and analyzed to obtain the statistics of turbulence characteristics, with the spatial coordinates aligned with respect to the moving water surface ($z = 0$).

Wave heights were also estimated from each PIV measurement. Under the "zero-fetch" condition, waves were not well developed. Dominant waves were high frequency short gravity waves with wave heights <10 cm. Due to its inertia, the floating platform was not significantly affected by these small waves. The wave height was then estimated from the location of the water surface recorded in PIV images, and the dominant wave period was obtained from spectral analysis of the time series of the estimated surface elevation. Figure 3-7 presents a sample result of time series of surface elevation and the surface elevation spectrum for Run 3. For the open water Runs, an ADV and two pressure sensors were moored on a large ship to record pressure and wave induced velocity at the depth of about 1 m. These measurements were used to estimate wave field parameters through the PUV method [*Gordon and Lohrmann*, 2002]. The resultant wave parameters and turbulence parameters are listed in Table 2 for Runs 1, 3, 4, 5 and 6.

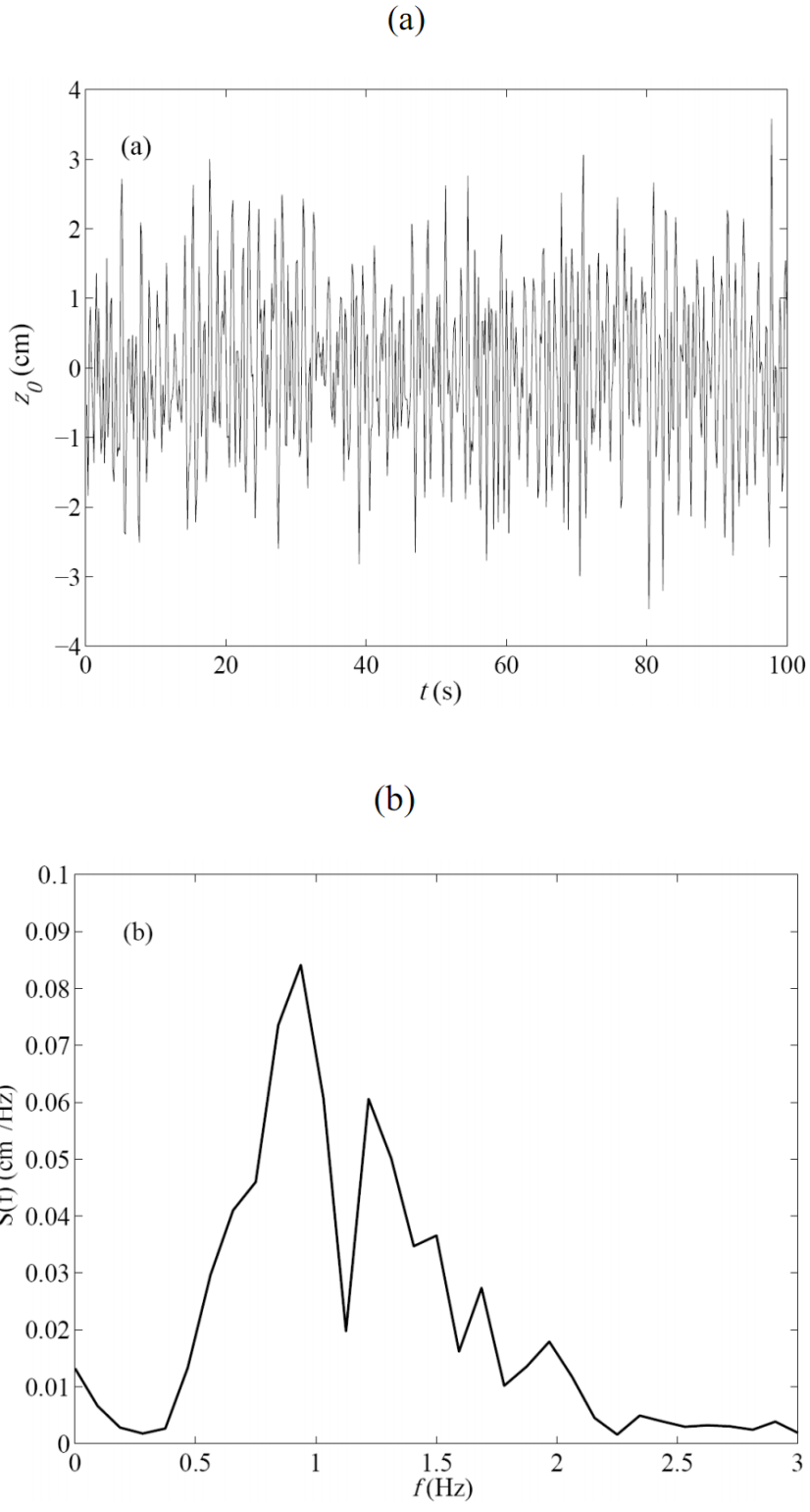

Figure3-7. A sample result of wave analysis obtained from PIV images (Run 3). (a) the time series of surface elevation; (b) the wave elevation spectrum.

Table 3-2. Wave field parameters and turbulence parameters (note: the turbulent kinetic energy k in the definition of Turbulent Reynolds number Re_L is calculated as: $k = (u'^2 + 2w'^2)/2$)

Run	Significant wave height, H_s (cm)	Characteristic wave angular freqency, ω_c (rad/s)	Turbulent Reynolds number, $Re_L = k^2/(\varepsilon\nu)$	Reynolds number based on wave parameters, $Re_w = (a^2\omega_c)/\nu$	Kolmogorov length scale, $\eta = (\nu^3/\varepsilon)^{1/4}$ (m)
1	2.18	8.64	98	4,104	2.7×10^{-4}
3	4.75	5.89	283	13,304	2.6×10^{-4}
4	2.29	10.61	310	5,550	3.0×10^{-4}
5	8.66	6.28	607	47,177	1.6×10^{-4}
6	35	1.85	79	188,000	2.5×10^{-4}

3.5 TKE dissipation rate

Determining the vertical profile of dissipation rate is of interest as it relates to the mixing process in the surface layer. Under breaking wave conditions, *Terray et al.* [1996] proposed a three-layer structure, with the top layer exhibiting an approximately constant dissipation rate, where turbulence is produced directly from wave breaking. Below this layer (about 60% of significant wave height, H_s), a rapid decaying region with $\varepsilon \sim z^{-2}$ scaling is present, with the combined effect of wave and wind forcing. The thickness of this region depends on H_s and the wave age. The third layer is found to have a scaling similar to the wall turbulence, i.e., $\varepsilon \sim z^{-1}$. For a water surface covered by micro-breakers, *M H K Siddiqui and Loewen* [2007] used laboratory PIV measurements to determine a dissipation rate of $\varepsilon \sim z^{-0.7}$ in the top layer. They also observed $\varepsilon \sim z^{-2}$ in the transition region, with a thickness of $3.6H_s$ to $7.2H_s$ for young wind waves. There are

very few field data available to describe turbulence immediately below the water surface. The floating UWMPIV system presented here provides a unique approach to reveal the structures of dissipation rate and other statistics in the very top layer of the ocean/lake surface. Although such measurements are still highly challenging under high wind and bubble entraining conditions, for low to moderate wind speeds, the quality of obtained images was extremely good. Even under more turbulent conditions (e.g. Run 5), good statistical analysis was still possible after filtering out noisy images.

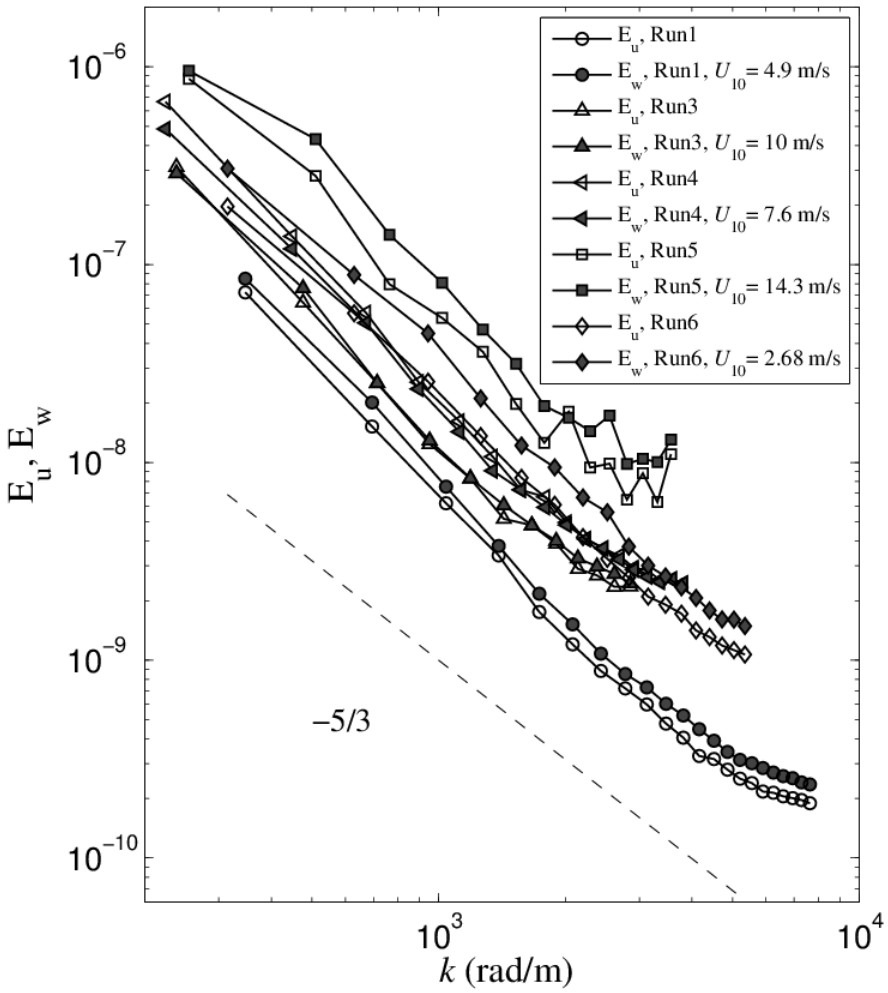

Figure 3-8. Wave-number velocity spectra of two velocity components measured at the depth z = 20 mm

Ensemble-averaged 1D velocity spectra along the horizontal direction (E_u and E_w for the horizontal velocity component *u* and the vertical component *w*, respectively) were calculated. Figure 3-8 shows the wavenumber spectra at a depth of about 20 mm from the water surface under different wind speed conditions. A -5/3 slope was observed in both the horizontal and vertical velocity spectra, suggesting the existence of an inertial sub-range. Higher signal noise was also found under a higher wind shear situation. The spectra demonstrated that the measured turbulence for runs 3, 5 and 6 were likely isotropic at this depth, since the average ratios of E_w to E_u within the inertial sub-range were very close to 4/3. For other cases, this ratio was generally lower than 4/3.

From the wavenumber spectra, the dissipation rate can be estimated by fitting the inertial sub-range with the -5/3 power law:

$$E_u = \frac{18}{55}\left(\frac{8\varepsilon}{9\alpha}\right)^{2/3}\kappa^{-5/3} \tag{6}$$

where κ is the wave number and the constant α is set to 0.4 [*Hinze*, 1975; *M H K Siddiqui and Loewen*, 2007; *Veron and Melville*, 1999]. In addition, another independent estimate of dissipation rate was determined by a "direct method" based on calculating the local in-plane velocity gradients from PIV measurements [*Doron et al.*, 2001; *Liao et al.*, 2009]:

$$\varepsilon_D = 3\nu\left[\overline{\left(\frac{\partial u'}{\partial x}\right)^2} + \overline{\left(\frac{\partial w'}{\partial z}\right)^2} + \overline{\left(\frac{\partial u'}{\partial z}\right)^2} + \overline{\left(\frac{\partial w'}{\partial x}\right)^2} + 2\overline{\frac{\partial u'}{\partial z}\frac{\partial w'}{\partial x}} + \frac{2}{3}\overline{\frac{\partial u'}{\partial x}\frac{\partial w'}{\partial z}}\right] \tag{7}$$

The comparison of estimated dissipation rates between the two methods averaged over the top 5 cm of water column is shown in Table 3 except for Run 2, when the turbulence was very low under quiescent environmental conditions. The results from the

"spectra fitting method" were systematically ~10% greater than those from the "direct method" for runs 3-5. Similar comparisons were reported by *Doron et al.* [2001](53% higher) and *M H K Siddiqui and Loewen* [2007] (44% higher). For Run 1 and Run 6, the "spectra fitting method" resulted in smaller dissipation rates than the "direct method".

Table 3-3. Comparison of surface shear velocity and dissipation rate of TKE

Run	$u_{*_w} = \sqrt{-\overline{u'w'}}_{\max}$ (cm/s)	$u_{*_w} = \sqrt{\frac{\rho_a C_D U_{10}^2}{\rho_w}}$ (cm/s)	$u_{*_w} = (\kappa z \varepsilon_{LOW})^{1/3}$ (cm/s)	$\varepsilon_D(z = 0 \sim 5cm)$ (direct method) (m^2/s^3)	$\varepsilon(z = 0 \sim 5cm)$ (spectra fitting) (m^2/s^3)
1	0.87	0.61	0.58	2.264×10^{-5}	1.715×10^{-5}
3	1.28	1.26	0.79	8.587×10^{-5}	9.912×10^{-5}
4	1.06	0.90	0.56	4.326×10^{-5}	4.768×10^{-5}
5	2.30	2.00	1.23	4.798×10^{-4}	5.036×10^{-4}
6	0.34	0.35	1.16	1.727×10^{-4}	9.739×10^{-5}

In order to further compare the two methods, vertical profiles of dissipation rates for all runs were plotted (Fig. 9). Profiles estimated from the two methods agree well in shape, with matches being better under higher wind stresses.

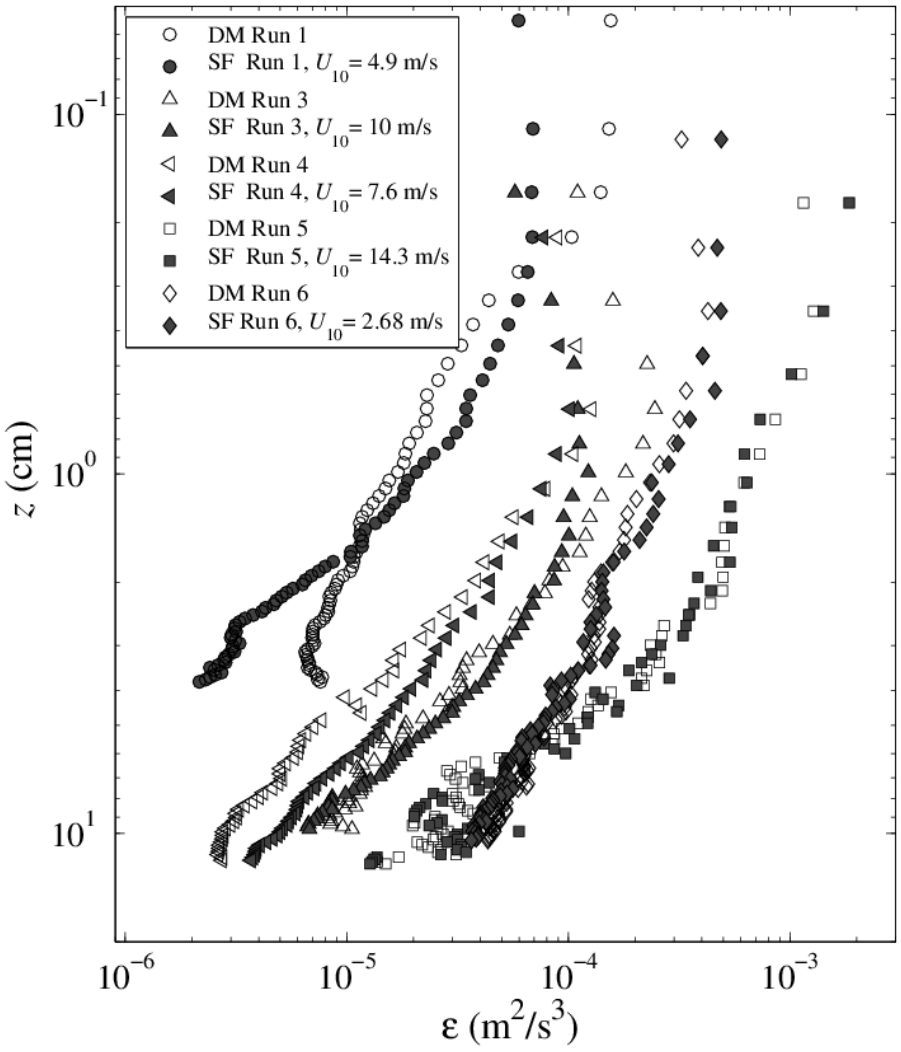

Figure 3-9. Vertical profiles of the dissipation rate of TKE, estimated with the spectral fitting method (SF) and the "direct" method (DM).

Vertical profiles of dissipation rate with the "direct method" estimation are also shown in Figure 3-10 with a log-log scale. Two power law relations, $\sim z^{-1}$ and $\sim z^{-2}$, are plotted as references. Measured dissipation rate in this study covered a wide range from 10^{-6} $m^2 s^{-3}$ to 10^{-3} $m^2 s^{-3}$. In general, all profiles exhibited power-law behaviors, $\varepsilon \sim z^{-n}$ with the exponent n ranging between 1 and 2. A thin layer with nearly constant dissipation rate was observed immediately below the air-water interface. For all runs, the

thickness of the thin layer was less than 1 cm. Below this thin layer, wall turbulence scaling behaviors were observed for runs 1~5. A least-square fitting with the power law was applied to these cases, with the fitted exponent *n* being 1.30, 1.31, and 1.43 for Runs 1, 3, and 4, respectively. For the case of run 5, two power law layers can be distinguished, with the dissipation rate decaying more rapidly ($\varepsilon \sim z^{-2.0}$) at deeper positions, i.e., (z > 4 cm). The slower decaying layer in the top 4 cm, where the enhanced near-surface dissipation might be attributted to microscale breaking, scales approximately with $\varepsilon \sim z^{-0.72}$, which is very close to Siddiqui and Loewen's (2007) laboratory observation,. For the open lake case (run 6) with a much weaker wind shear and older wave age, the dissipation rate decays more slowly with depth (n = 0.82). The difference in the exponent may be an indication of different turbulence production and transport mechanisms. For a high wind condition, near surface turbulence is dominated by surface shear. When waves are present, turbulence might be a product of energy transfer from wave orbital motion to turbulent fluctuations. Nonlinear interaction among waves, surface current and turbulence may also significantly affect the vertical structures of dissipation rate.

It is worth noting that the thin layer of nearly constant dissipation rate immediately below the water surface might be an indication of a higher mixing rate within this layer due to microscale breaking. This rapid mixing in this upper layer could have a significant influence on the transport of momentum, heat and gases. More investigations are needed to reveal the mechanism and scaling of turbulence near the surface.

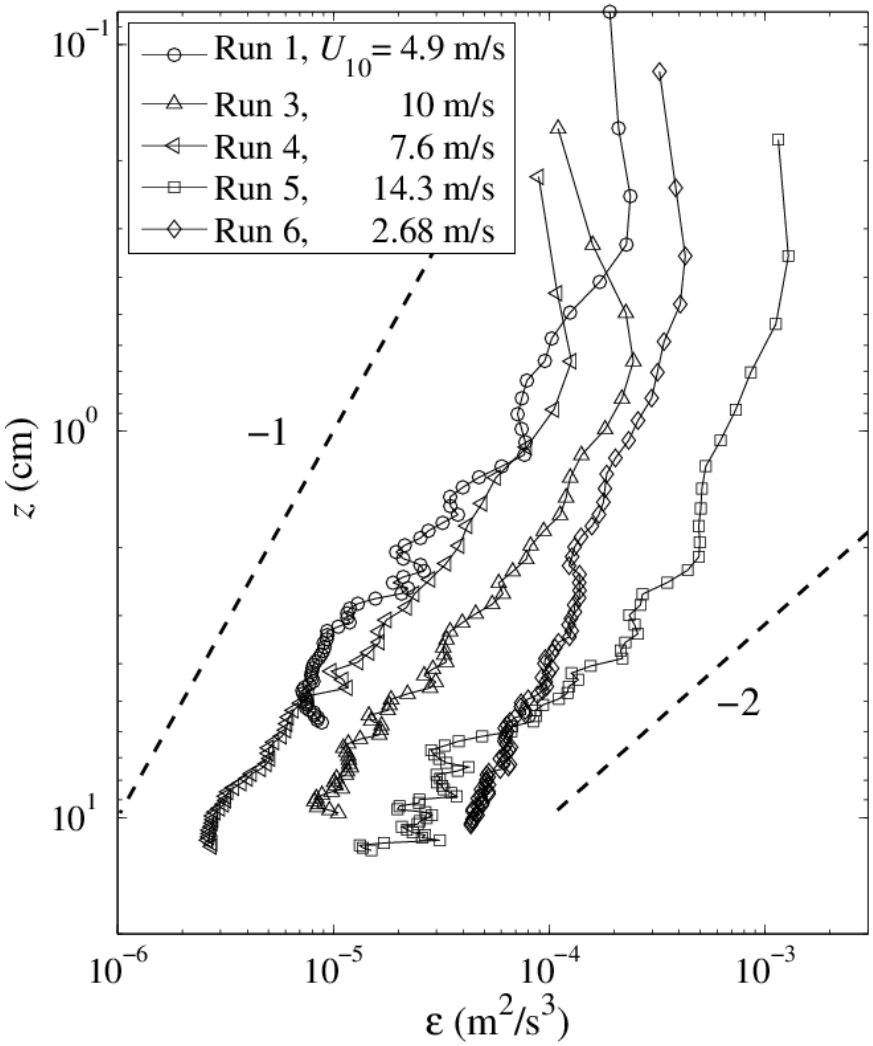

Figure 3-10. Vertical profiles of dissipation rate of TKE on a log-log scale.

3.6 Reynolds shear stress and surface shear velocity

Surface shear velocity, u_{*w} is an index of interface shear stress on the water side, and is a crucial property that regulates the transfer of mass, momentum and energy. It can be defined as

$$u_{*w} = \sqrt{\tau_i / \rho_w} \tag{8}$$

where τ_i is the shear stress at the air-water interface and ρ_w is the density of water. It is difficult to make an accurate estimate of the shear velocity in field studies. One common method is to fit the wind velocity profile $U(z)$ in the air side "wall layer" following "Charnock's Law" [*Charnock*, 1955]:

$$\frac{U(z)}{u_{*a}} = \kappa^{-1} \ln\left(\frac{gz}{u_{*a}^2}\right) + C \tag{9}$$

where $u_{*a} = \sqrt{\tau_i / \rho_a}$, is the air side shear velocity. A more empirical method is to use wind speed measured at 10 m height, U_{10}, to estimate the shear stress through the drag law:

$$u_{*a} = \sqrt{C_D U_{10}^2} \tag{10}$$

where, C_D is drag coefficient, which is an empirical parameter that depends on surface roughness, fetch, waves, and wind speed. In this study, the drag coefficients for run 1~5 were calculated as functions of wind speed [*M Yelland and Taylor*, 1996] as follows,

$$\begin{aligned} 1000 C_{D10} &= 0.29 + \frac{3.1}{U_{10}} + \frac{7.7}{U_{10}^2} (3 \le U_{10} \le 6 m/s) \\ 1000 C_{D10} &= 0.60 + 0.070 * U_{10} (6 \le U_{10} \le 26 m/s) \end{aligned} \tag{11}$$

For the open water case (i.e. run 6), due to the influence of "virtual" roughness generated by gravity waves on surface stress eases, I applied the empirical parameterization $C_{D10} \approx 0.0044 U_{10}^{-1.15}$ suggested by *Wuest and Lorke* [2003] for weak wind (U_{10} < 3 m/s). The resultant drag coefficients for runs 1, 3~6 are 0.0012, 0.0013, 0.0011, 0.0016 and 0.0014, respectively.

With the wind shear estimation, shear velocity on the water side can be obtained through:

$$u_{*w} = \sqrt{\frac{\rho_a u_{*a}^2}{\rho_w}} \tag{12}$$

u_{*w} can also be estimated by fitting the vertical profile of the dissipation rate with the "law of the wall" (LOW) scaling for cases under a relatively low or moderate wind speed,

$$u_{*w} = \left(\kappa z \varepsilon_{LOW}\right)^{1/3} \tag{13}$$

LOW scaling implies equilibrium between turbulence production and dissipation, and $\varepsilon \sim z^{-1}$ near the water surface. For a wave dominant boundary layer, this scaling has been shown to underestimate the decay rate of TKE dissipation [*Agrawal et al.*, 1992; *Melville*, 1994].

In this study, I applied a "direct" method to calculate the profile of Reynolds stresses, which uses the estimates of surface shear velocity. First, an empirical approach is adopted to decompose turbulent fluctuations from the raw data, which include wave orbital velocities, mean current and platform motions. This empirical approach assumes that the integral length scale of turbulence near the water surface is smaller than the FOV of PIV images (i.e., it would scale with κz if the law of wall applied). It is also assumed that the wavelength of surface waves is much larger than the FOV. Therefore the horizontal mean velocity over the FOV of one PIV image is considered as an estimate of the combined velocity of current, wave and platform motion, and the deviation from the mean is considered as turbulent fluctuations. In practice, the instantaneous vertical profile of mean velocity (or low-pass filtered velocity) was obtained by spatially averaging each row of the 2D velocity field at different depths below the water surface. In addition, the instantaneous mean profile was further smoothed in time with a running

average over the time series of these profiles. The low-pass filtered mean velocities are denoted as $U(z,t)$ and $W(z,t)$. Then the instantaneous turbulent fluctuations were determined by subtracting the reconstructed mean profile. As a result, Reynolds stresses can be directly calculated through the cross-correlation of the fluctuating velocity components.

Figure 3-11 (a) shows the profiles of Reynolds shear stress for wind shear dominant runs (e.g. runs 1, 3, 4 and 5) and the open water run 6. Figure 3-11 (b) shows the profiles of Reynolds shear stress normalized to u_{*w} obtained from equation (10) and (12) (i.e., estimated from wind shear/drag), versus the normalized depth with respect to the estimated significant wave heights (see Table 2). The non-dimensional Reynolds shear stress profiles are very similar in shape, although they do not seem to collapse onto a universal scaling. For higher wind conditions (e.g. runs 3, 4, 5), the turbulence is dominated by surface wind shear, which shows good agreement with the wall turbulence scaling, e.g., the ratio of the near surface Reynolds stress to u_{*w}^2 equals approximately 1.0. Profiles normalized with u_{*w} and the viscous length ν/u_{*w} result in a slightly better scaling than with the wave height, except for the two low wind cases (run 1 and 6) (Fig. 11(c)).

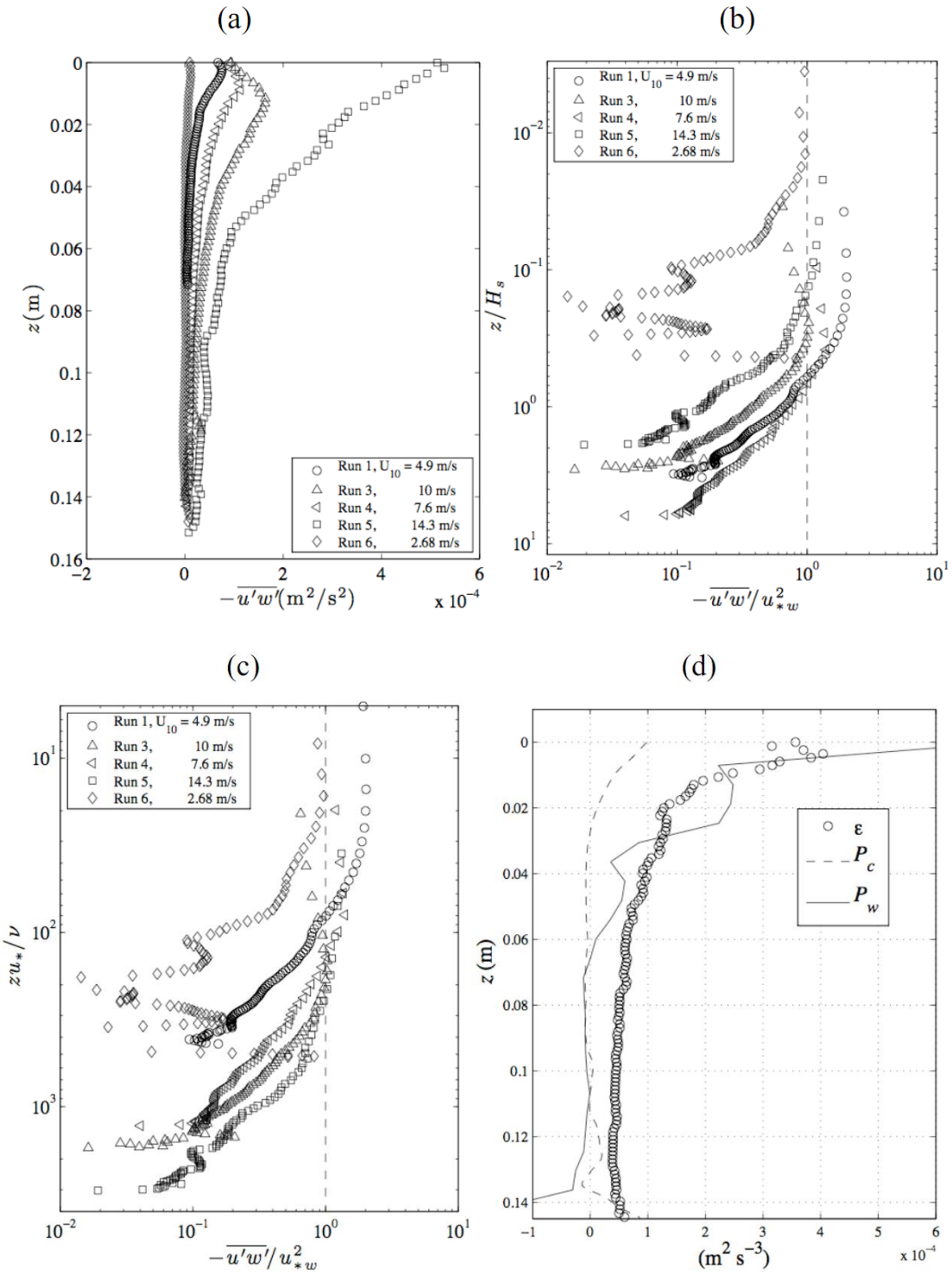

Figure 3-11. Vertical profiles of Reynolds shear stresses. (a) un-scaled; (b) non-dimensionalized by the surface shear velocity (estimated from wind drag) and the significant wave heights. (c) non-dimensionalized by the surface shear velocity and the viscous length scale. (d) Production and dissipation of TKE for run 6.

According to the profiles of Reynolds shear stresses (Fig 11(a)), I denote the maximal value along the vertical profile for each run as the estimate of the surface shear velocity squared. The estimated shear velocities are compared with those obtained through wind drag estimates (equations (10) and (12)). Meanwhile, I performed another estimation by forcing the LOW scaling (equation (13)) to the measured profiles of dissipation rate in the upper layer (z = 0.4 ~ 4 cm) for each run. A comparison of results is shown in Table 3. For runs 3~5 when the surface wave heights were small, the surface shear velocity estimated from Reynolds shear stress is very close to, but systematically larger than, that from the wind drag estimation (the ratio ranges from 1.02 to 1.18), while the LOW estimation is systematically smaller than the wind stress estimation (the ratio ranges from 0.62 to 0.63). The LOW estimation assumes that the Reynolds stress in the wall scaling region (z = 0.4 ~ 4 cm for case 3~5) is constant and equal to the shear velocity squared. However, measured data in this layer showed that Reynolds shear stress clearly decreases with depth, and it should be smaller than the shear velocity squared at the surface. This might explain the underestimation following the LOW estimation. Given the fact that the three estimates were from independent measurements, the agreements from observations are very good. It suggests that turbulence decomposition with respect to spatial mean is a valid approach for this study.

For run 6 on the open lake, surface shear velocity from the ensemble average Reynolds stress matched well with the wind drag estimate. However, the LOW dissipation approaches significantly overestimated the surface shear velocity. This is an indication that other sources of turbulence exist in addition to the direct wind input. The turbulence might be a direct result of the wave orbital velocity combining with effects of

wind, wave, current-wave and wave-wave interactions. It should be noted that the Reynolds shear stress does have a sign. For a shearing dominant turbulent flow under an equilibrium condition, the sign of the Reynolds shear stress $-\overline{u_i' u_j'}$ is usually the same as the mean velocity gradient, $\frac{\partial U_i}{\partial x_j}$, so the production term, $-\overline{u_i' u_j'}\frac{\partial U_i}{\partial x_j}$, is positive. This implies that the Reynolds stresses arise from shear induced "eddies". The sign of mean velocity gradients alternates between positive and negative in a wave induced orbital velocity field. Figure 3-11(d) presents profiles of dissipation and turbulence production terms with two different approaches, where

$$P_c = -\overline{u'w'}\frac{\partial \overline{U}}{\partial z} - \overline{w'w'}\frac{\partial \overline{W}}{\partial z} \tag{14}$$

is the production with ensemble averaging, which represents effects of wind induced mean current and/or Stokes drift, whereas

$$P_w = -\overline{\langle u'w' \rangle}\frac{\partial \langle U \rangle}{\partial z} - \overline{\langle w'w' \rangle}\frac{\partial \langle W \rangle}{\partial z} \tag{15}$$

represents production that includes the effects of wave induced velocities. The bracket "< >" denotes spatial averaging of the instantaneous velocity field in the horizontal direction. The ensemble averaging over the spatial mean is applied to evaluate the mean production. Vertical binning over every 0.5 cm depth interval was also applied to the instantaneous profiles of <*U*> and <*W*> in order to obtain smoother profiles for the calculation of their vertical gradients. Turbulence production due to the mean flow (P_c) is much smaller than the dissipation rate over the entire depth, so it is not the major source of turbulence. Turbulence production due to waves (P_w) is approximately in balance with dissipation for top 5 centimeters, but decreases rapidly as it goes deeper.

These observations suggest that under a low wind shear, wave induced motion itself can contribute significantly to turbulence production, which occurs in a relatively thin layer under the air water interface. At a deeper position, enhanced dissipation rates may arise from turbulent transport of the Reynolds stresses from the production region, and this needs to be evaulated with further investigations.

Overall, the presented results suggest that the turbulence structure in a wind wave surface boundary layer is close to wall turbulence under low to moderate winds, while turbulence can be greatly enhanced by waves, which agrees with the laboratory observation of *Cheung and Street* [1988].

3.7 Conclusions

I have shown that a free-floating PIV system is capable of measuring near-surface turbulence structures. This has significant implications for the quantification of gas exchange across the ocean-atmosphere interface. With an oscillating and deforming wind wave surface on an ocean or lake, it is extremely difficult to accurately capture the structures of small-scale turbulence with traditional point-wise flow measurement instruments, such as the ADV. An advantage of PIV measurements is that small-scale turbulence properties, such as dissipation rate and vorticity, can be directly obtained through calculating the instantaneous spatial velocity gradients. It has been also demonstrated that, due to the intermittent nature of turbulence at the dissipative scales, velocity gradient statistics are dominated by spatially sporadic but strong local straining and rotational motions (see the filamentary structures on the vorticity map shown in

figure 3-6(b)), and they are much greater than the rotational speed of the floating platform created by surface waves. Therefore measured statistics such as the dissipation rate will not be significantly affected by the platform motion. Because the moving air-water interface is visible on most recorded PIV images, the position of the surface can be tracked either automatically through imaging processing, or manually through hand drawing. So the ambiguity of the vertical depth with respect to the moving surface can be resolved. These advantages make the floating PIV system a unique tool to characterize very detailed profiles of turbulence immediately below the air-water interface under non-breaking conditions.

Calibrating and exploratory experiments have been conducted in Lake Michigan to investigate the surface layer hydrodynamics with a nearly "zero-fetch" wind condition in the lake harbor and wavy surface conditions on the open lake. Experiments were conducted under a wide range of wind shear conditions (wind speed varied from <1 to about 14.3 m s^{-1}) to quantify near surface turbulence during the wind-wave generating and growing period. Vortices produced by high wind shear were observed near the water surface. Wavenumber spectra of velocities demonstrated -5/3 slopes of the inertial sub-range. The dissipation rates of TKE were estimated through the spectral fitting method and through the "direct" method by calculating the spatial gradients of velocities. Good agreement was found between the two methods. Vertical profiles of dissipation rate showed a thin layer (< 1 cm) of nearly constant values beneath the water surface for all cases. Profiles of dissipation beneath this thin layer can be well described by a power law decaying trend with depth, i.e., $\varepsilon \sim z^{-n}$. For "zero-fetch" wind shear cases n was found to be approximately 1.0, suggesting a "law of the wall" scaling for turbulence. For

the high wind case (wind speed = 15 m s^{-1}), another power law layer was found below the wall layer, with *n* approximately equal to 2.0, indicating a more rapid decay with water depth. The profile of dissipation for open lake, wavy conditions also exhibited a power law dependency, with the decaying power *n* being significantly smaller than 1.0.

Another advantage of PIV is that turbulence can be decomposed from the measured instantaneous velocity field, which consists of currents, waves and the platform motion. Considering the residual of the spatial filtering as the turbulent fluctuation, i.e., a concept similar to the "large eddy simulation" (LES) approach, I was able to calculate the Reynolds stresses directly. For wind shear dominated cases measured under the "zero fetch" condition, the estimated shear velocity from the measured profiles of Reynolds shear stress agreed well with the estimates from the surface wind shear stress. They also scaled well with shear velocities estimated from the profiles of dissipation rates following the "law of the wall". These comparisons suggest that the turbulence decomposition approach is valid.

Measurements in the open water case with low wind and moderate surface waves indicated that surface waves are a significant source of turbulence. The near-surface vertical structures of dissipation and Reynolds shear stress can not be described by the "law of the wall" scaling. More field experiments are needed to investigate near-surface turbulence budgets under waves, and the free-floating PIV system will be a valuable tool for this purpose. Coupled with measurements of air/water gas gradients and gas flux measurements, such as those derived with the eddy covariance method, I hope this instrument can provide new insights into the fundamental physics of near surface

turbulence and its role in controlling the fluxes of mass, momentum and energy across the lake-atmosphere and ocean-atmosphere interfaces.

Chapter 4

Experimental Study on Turbulence Structure Immediately Below the Air-Water Interface

4.1 Experiments

The primary data presented in this chapter was collected in an open lake environment (outside of Milwaukee Harbor) from November 2011 to November 2012 on Lake Michigan (denote as run "W" in this chapter). For all "W" runs with relatively large waves, the deployment sites are about 1.2 km away from the shore with a nominal water depth of 10 meters. Besides FPIV system, two pressure sensors and a Nortek ADV were moored on the R/V to record simultaneously the pressure and wave induced velocity at about 1 meter depth below the air-water interface for W1. PUV method [*Gordon and Lohrmann*, 2002] was applied to estimate wave field parameters in this dataset. During the experiments, wind speed, wave height, as well as wave age were recorded. For all "W" runs, the wave height was typically larger than the FOV of PIV images. In addition, a series of field deployments at the inner harbor of Lake Michigan (Milwaukee River)

were conduced prior to open lake experiment from August to November 2011 (denote as run "T"). One can consider run T as the cases under effects of very young waves with almost zero fetch condition. Table 1 summarizes the environmental conditions and experimental configuration parameters.

For all "T" runs, the FPIV system is loaded to the measured sites from the dock area of harbor or a small boat. For open lake run "W", the instrument was launched from the deck of R/V Neeskay or Osprey. Prior to deployment, the instrument need to be calibrated (to get resolution of CCD camera) and carefully adjusted (e.g. focus condition, sweeping time of laser, the position of floating fenders, etc) to meet different environmental conditions, such as, surface wind forcing, background light, water turbidity, etc. In summary, 2-4 sets of images were acquired in each run. 2000-4000 image pairs were collected in each dataset at sampling rate of 6-12 Hz, which corresponded to measurement duration of about 10-15 minutes.

Table 4-1: Summary of Floating PIV parameters and statistical characteristics for each run[1]

Run	PIV sampling rate (*Hz*)	Sweeping time (*ms*)	FOV (*cm*×*cm*)	Resolution (*μm/pixel*)	U_{10} (*m/s*)	Significant wave height (cm)	Wave age, c_p / u_*	Kolmogorov length scale, $\eta = (\nu^3/\varepsilon)^{1/4}$ (m)
T1	12	11	14.96×11.26	110	7.6	2.29	26.7	3.0×10^{-4}
T2	6	7	14.96×11.26	110	10.0	4.75	15.9	2.6×10^{-4}
T3	8	4	15.91×11.98	117	14.3	8.66	9	1.6×10^{-4}
W1	8	4	15.91×11.98	117	2.68	35	1127	2.5×10^{-4}
W2	6	4	17.59×13.24	129	8.09	40	463	2.1×10^{-4}
W3	6	4	17.59×13.24	129	10.9	47	270	2.1×10^{-4}

[1] u_* is friction velocity in water side in definition of wave age.

4.2 Data analysis

The main purposes of the FPIV deployment in this chapter is to measure vertical profiles of turbulent characteristics immediately below the air-water interface. The air-water interface can be clearly identified for cases under low to moderate wind speed conditions, as higher density of natural particles (plankton, sediment or micro air bubbles) accumulate on the surface. For these cases, the surface location can be tracked by an ad-hoc image processing algorithm. However, for cases with strong wave motion and surface scatter due to air entrainment, a more complicated image processing algorithm might be required for locating water surface. In the present study, surface location is traced manually image by image. Details of the surface locating and reconstruction procedures can be found in chapter 3. The estimated maximum error for water surface location is about 50 image pixels, or 6 millimeters according to the PIV resolution. In this study, the triangular mesh was generated (see chapter 3) in the determined computational domain with a predefined nominal mesh size (15 image pixels, 1.76 mm). The mean effective area of a triangular mesh is equivalent to a square of about 8×8 pixels.

A multi-pass anti-aliasing interrogation algorithm [*Liao and Cowen*, 2005] was applied to evaluate 2-D instantaneous velocity at each grid node. In this study, the sub-window size of the final pass was set to 24×24 pixels, or 2.8×2.8 mm physically. Ensemble average analysis was applied to statistically investigate the turbulent characteristics under the waving water surface. In order to obtain vertical profiles, the coordinate system was transformed from moving unstructured system to a fixed structured one. For each column of the structured mesh, I realign all the columns into the

fixed coordinate system with $z = 0$ indicate water surface and z increases downward with depth, following the same definition of coordinate system as in chapter 3.

4.3 A typical vortices evolution snapshot

Vortices with strong vorticity were observed in near surface region. Since strong shearing motions exist near the air-water interface, reliable vortex statistics need to be quantified as the evidence of strong swirling motion rather than significant vorticity [*Adrian et al.*, 2000]. To illustrate eddy structure, two dimensional velocity gradient tensor D^{2D} is calculated to quantify the swirling strength in 2-D instantaneous velocity field [*Chong et al.*, 1990].

$$D^{2D} = \begin{bmatrix} \frac{\partial u}{\partial x} & \frac{\partial u}{\partial z} \\ \frac{\partial w}{\partial x} & \frac{\partial w}{\partial z} \end{bmatrix} \tag{1}$$

In this case, D^{2D} either has two real eigenvalues (λ_r) or a pair of complex conjugate eigenvalues ($\lambda_{cr} \pm \lambda_{ci}$). Therefore, the local eddies are defined in iso-regions of $\lambda_{ci} > 0$. Figure 4-1 shows the time sequence of eddy evolution during 1 second. The vortex structure was clearly seen being transported and deformed. A group eddies with high swirling strength rotate clockwise in the FOV of PIV images and meanwhile stretched by local shear motion into several individual eddies.

The breaking down process on these eddies by local shear is consistent with high turbulent dissipation, which is related to the interfacial gas transfer when approaching the air-water interface. From the experiment results, the evolution of turbulent eddies is

typically of very short time scale, which is controlled by combined effect of wind shear and surface waves.

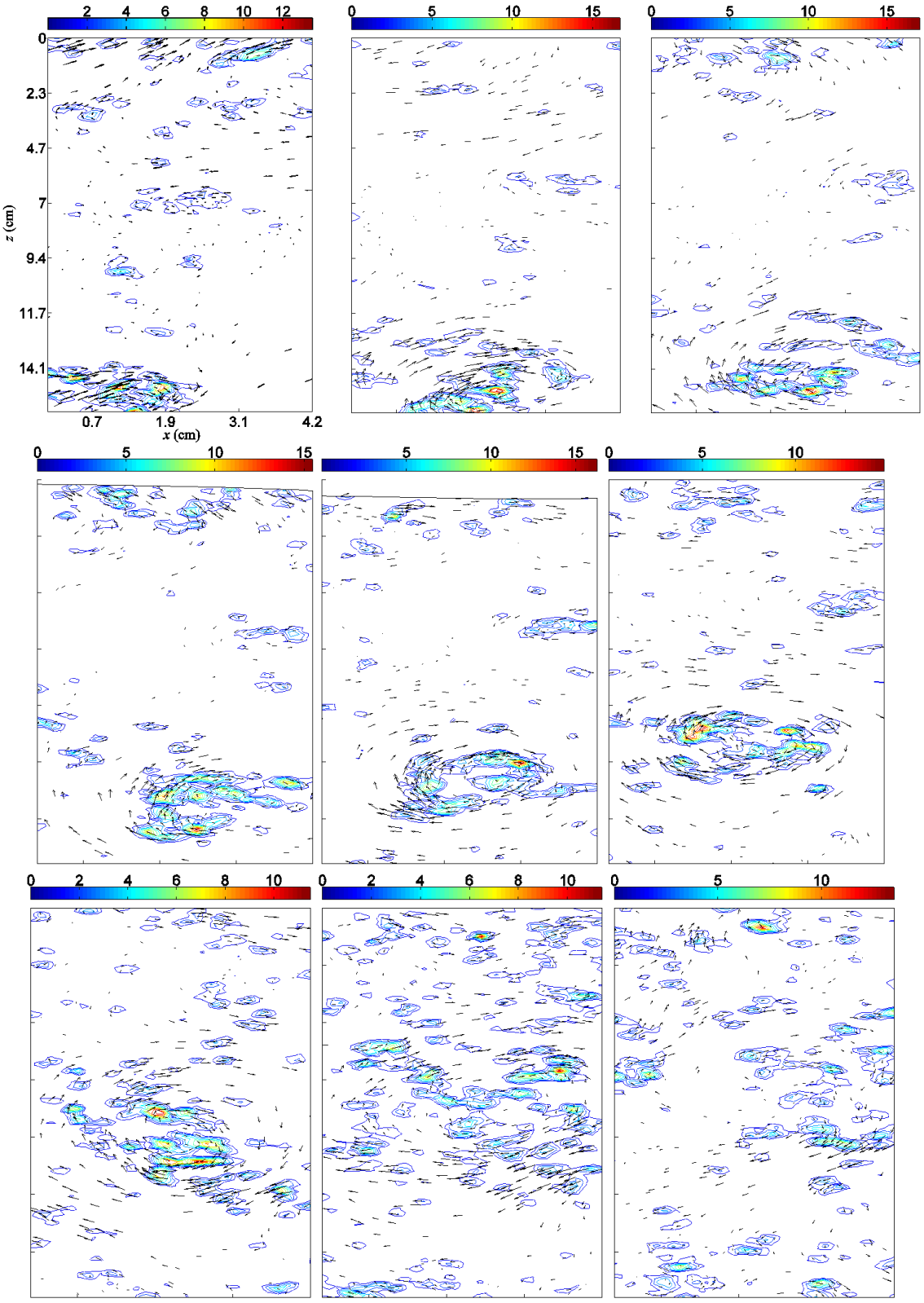

Figure 4-1: Evolution process of identified near surface vorteices. Velocity vector of "local eddies" is superimposed. The unit of colorbar is s^{-1}

4.4 Dissipation rate estimation

The dissipation rate of TKE for Newtonian fluids is defined,

$$\varepsilon = 2\nu \left\langle s_{ij} s_{ij} \right\rangle \tag{2}$$

where the rate of strain tensor s_{ij} contained nine local velocity gradients to be measured or estimated. Therefore, to obtain the spatial distribution of dissipation rate with this definition requires measurement of the 3 components of velocities in the 3 dimensional space with high resolution. Although the technology exists, such as a 3D3C PIV system, it has only been done in laboratory settings. Field measurements of dissipation rate usually invoke the Kolmogorov's similarity hypothesis of isotropy, and rely on the existence of the inertial subrange, where the velocity spectra or the structure function scale with the dissipation rate only. With the high resolution 2D PIV technique, there exists a number of methods to estimate the dissipation rate with less assumptions than a point-wise measurement device.

4.4.1 Vertical profiling with "direct method"

The "direct method" is widely used for estimating dissipation rate for a 2-D PIV system [*Doron et al.*, 2001; *Liao et al.*, 2009; *K Siddiqui and Loewen*, 2010], since 4 in-plane local velocity gradients can be directly measured from PIV data (e.g. $\frac{\partial u}{\partial x}$, $\frac{\partial u}{\partial z}$, $\frac{\partial w}{\partial x}$, $\frac{\partial w}{\partial z}$ in this study). Additionally, $\frac{\partial v}{\partial y}$ can be estimated from continuity equation. Only

out-of-plane gradients of *u* and *w* need to be modeled with assumption of local isotropy. In this study, "direct" estimation of dissipation rate of TKE is given by

$$\varepsilon_D = 3\nu\left[\overline{\left(\frac{\partial u'}{\partial x}\right)^2} + \overline{\left(\frac{\partial w'}{\partial z}\right)^2} + \overline{\left(\frac{\partial u'}{\partial z}\right)^2} + \overline{\left(\frac{\partial w'}{\partial x}\right)^2} + 2\overline{\frac{\partial u'}{\partial z}\frac{\partial w'}{\partial x}} + \frac{2}{3}\overline{\frac{\partial u'}{\partial x}\frac{\partial w'}{\partial z}}\right] \quad (3)$$

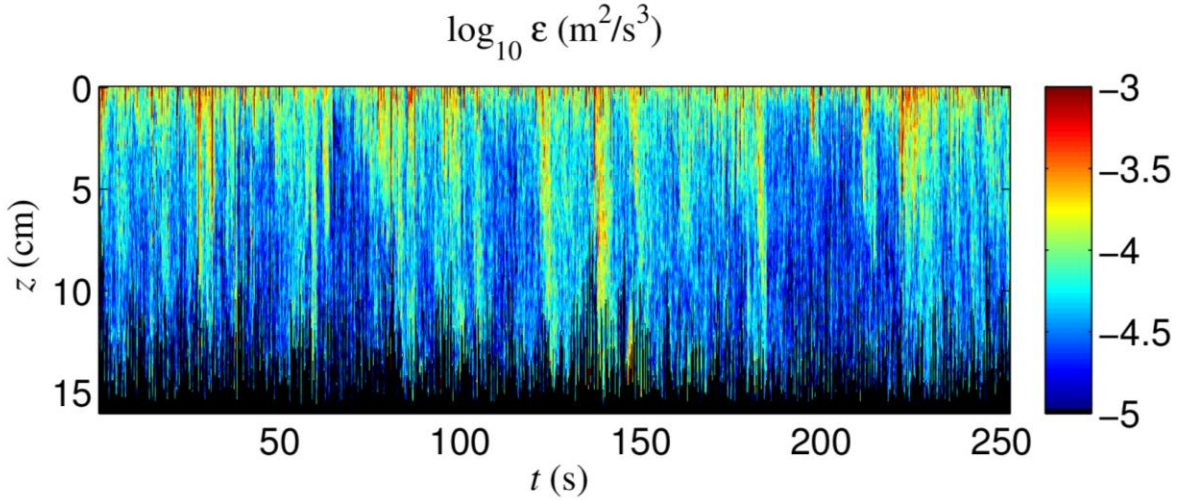

Figure 4-2: Time series vertical profile of turbulent dissipation rate immediately below the air-water interface (Run W1). $z = 0$ represents the air-water interface after vertical mapping. Black area indicates no data at that depth below the water surface.

The instantaneous turbulent dissipation was calculated in each grid points of triangular mesh and transformed to a structured mesh for each PIV sampling snapshot. Figure 4-2 shows a time series of dissipation rate of TKE profile immediately below the detected air-water interface. Because of the moving water surface, the sampling distance below the water surface varies responding to the instantaneous wavy lake surface. The black area means no data acquired at such distance below the water surface. The result shows the high intermittency near the air-water interface. Two orders of magnitude

differences were observed in the top 15 centimeters. The dissipation rate time series profile clearly shows the stronger turbulent level near the water surface (Figure 4-3).

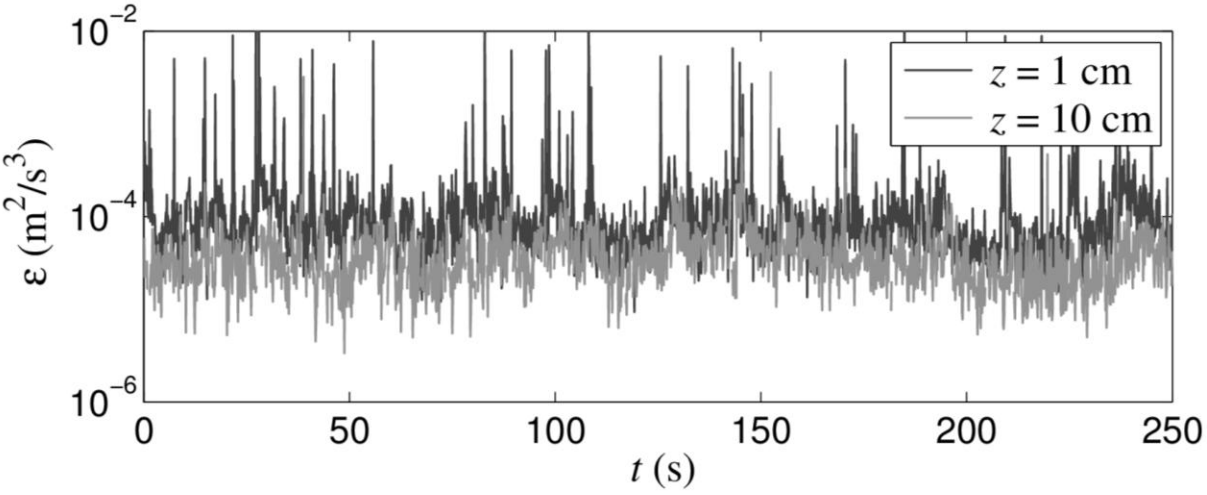

Figure 4-3: Time series of dissipation rate at two different depths below the air-water interface (Run W1): z = 1 cm and z = 10 cm

In order to investigate the near surface turbulence wave interaction, the vertical profile of dissipation rate for all runs was compared in figure 4 with log-log plotting. The turbulent dissipation varies from order of magnitude of 10^{-6} to 10^{-3} m^2/s^3 depending on different wind shear and wave field. A thin layer with nearly constant dissipation rate was observed immediately below the air-water interface. For all runs, the thickness of the thin layer is less than 1 cm. Below this thin layer, the vertical dissipation rate profile approximately follows the power law with depth as $\varepsilon \sim z^{-n}$. As the reference, n = 1 and 2 are also plotted in figure 4-4.

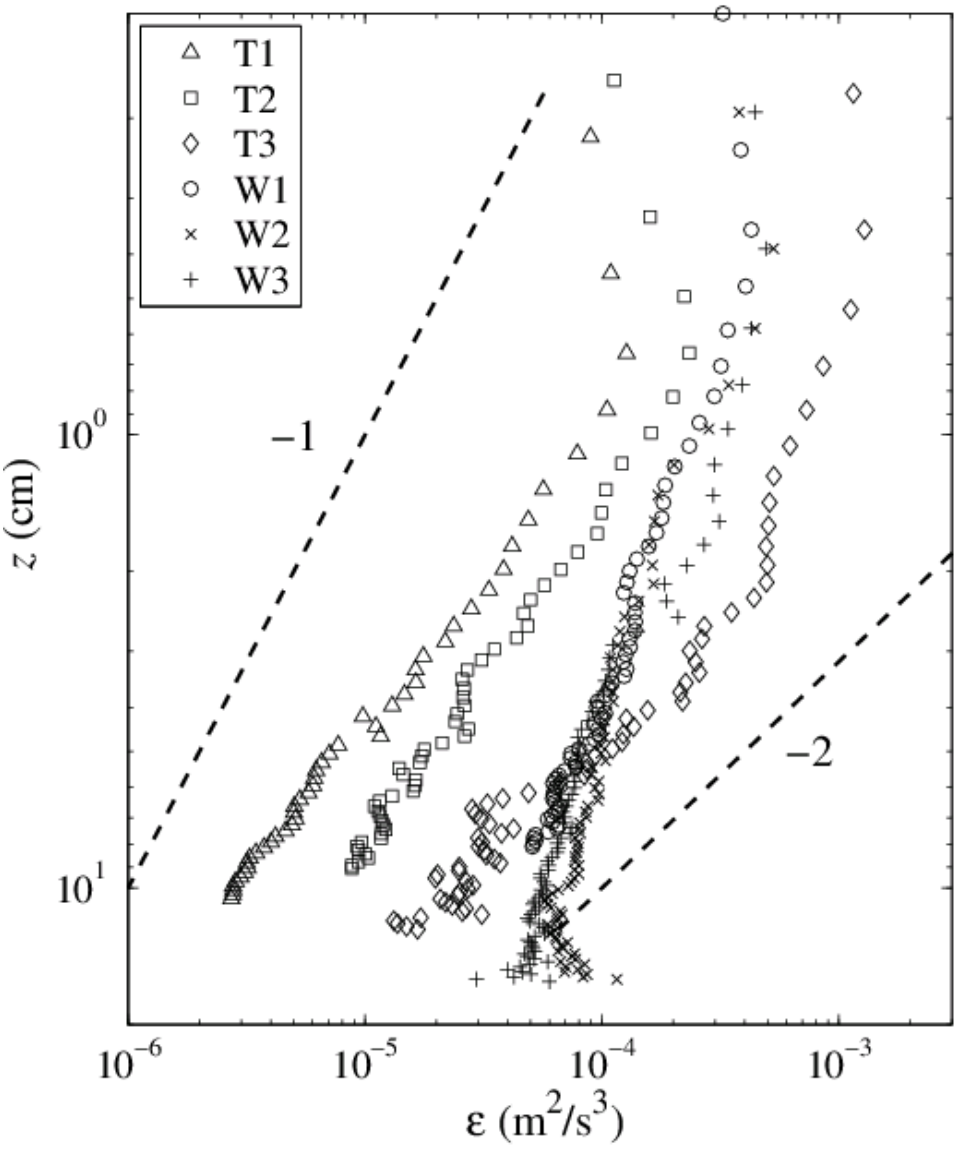

Figure 4-4: Vertical profile of dissipation rate by "direct" estimation

Shown in figure 4-4, the dissipation rate profiles for runs W can be clearly distinguished from runs T. Slower decay rate of turbulent dissipation rate was observed in the measured region under effect of surface waves. *M H K Siddiqui and Loewen* [2007]

argued that the small n indicates the thin layer in the presence of micro-breaking waves. In their laboratory study, n = 0.7 in the enhanced turbulent dissipation region (about $0.4H_s$). For "T" runs, the power scaling n is close to 1 similar to wall turbulence behavior. The difference in the exponent n might be an indication of different turbulence production and transport mechanisms. For a high wind condition, near surface turbulence are dominated by the surface shear. When waves are present, turbulence might be a product of energy transfer from wave orbital motions to turbulent fluctuations. Meanwhile, nonlinear interaction among waves, surface current and turbulence may significantly affect the vertical structures of dissipation rate. As can be seen in figure 4-4, with the increasing the distance away from the air-water interface, the turbulent level in run W trends to be larger than T3 with wind speed of 14.3 m/s as the result of slower decaying rate. The evidence clearly shows the effect of waves on near surface turbulence structure.

4.4.2 Discussion on different methods for dissipation rate estimation

(a) Linear fitting in inertial sub-range from 1-D velocity spectra

The most popular mean in estimating dissipation rate in field is linear fitting in the inertial sub-range (IR) based on velocity spectra data. For single-point measurement, wave number spectrum can be obtained from the transform of frequency spectrum based on the advection velocity (ship movement if device moored on a ship, current speed if drifting device is used). For PIV data, the wavenumber spectra is directly obtained since

2-D spatial velocity domain can be resolved without invoking Taylor's frozen turbulence hypothesis. This method relies on the assumption of fully developed, homogeneous and isotropic turbulence in the IR such that the corresponding wave-number spectrum exhibits -5/3 slope.

In this study, the dissipation rate was determined from the relation,

$$E_{11}(k_1) = \frac{18}{55}\left(\frac{8\varepsilon_{LF}}{9\alpha}\right)^{2/3} k_1^{-5/3} \tag{4}$$

where E_{11} is the 1-D spectrum density based on Fourier transform of horizontal velocity (representing the superscript 1) as a function of horizontal wave-number k_1, and constant α=0.4 [*Veron and Melville*, 1999]. The dissipation rate can also be estimated by vertical velocity spectrum E_{33}. Isotropic turbulence will be shown if,

$$E_{11}(k_1) = \frac{3}{4}E_{33}(k_1) \tag{5}$$

Figure 4-5 shows log-log scale plot of 1-D horizontal wave-number for both horizontal and vertical velocity spectrum (represented by $3/4E_{33}$) with kolmogorov scaling for three different depths below the water surface (z = 1, 5 and 10 cm). Higher energy level is clearly shown in the figure when approaching the interface. -5/3 slope indicating the kolmogorov universal scaling in sub-range is observed in near surface turbulence structure. Dissipation rate was estimated through linear fitting in the IR from both horizontal and vertical spectrum, denoted as ε_{LF11} and ε_{LF33}.

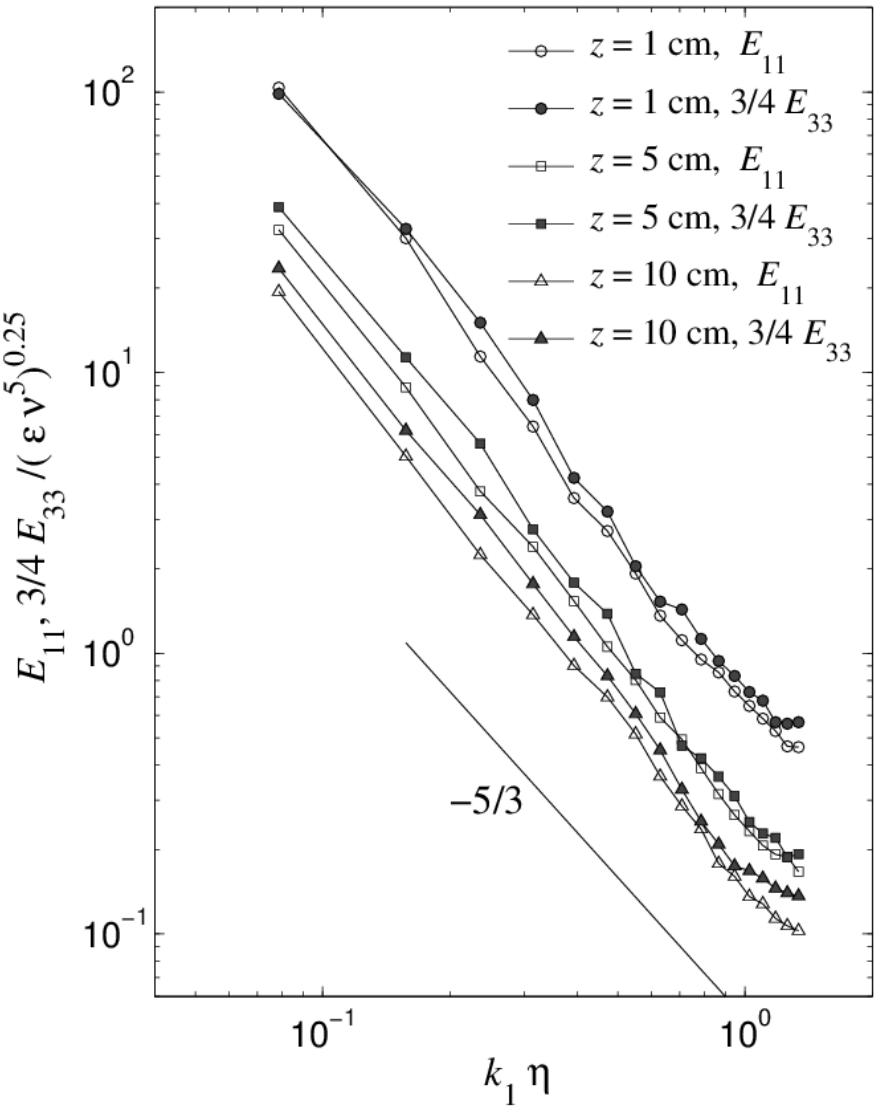

Figure 4-5: Nondimensional 1-D velocity spectrum at different depth from the air-water interface (Run W1)

For ideally isotropic turbulence, the 1-D velocity spectrum plotting for E_{11} and $3/4E_{33}$ should be collapse with the same energy level. As is evident in figure 4-5, near surface turbulence shows $3/4E_{33}>E_{11}$ in the observed wave-number range, although they

are very close. However, the local isotropic turbulence is hard to conclude by the mean of this feature. The ratio of $3/4E_{33}$ and E_{11} is 1.03, 1.23 and 1.23 for z = 1, 5 and 10 cm, respectively. Since the FOV limited the range of wave-number, the data do not reach the integral length scale. *Nimmo Smith et al.* [2005] applied an extended method for PIV analysis by local advection velocity in a bottom boundary layer in a costal ocean. However, this method is not suitable for near surface turbulence since strong wave orbital motion and short time scale of turbulence evolution. At the high wave-number end of observed spectrum (250 rad/m < k < 300 rad/m), *Doron et al.* [2001] reported spectral "humps" when velocity components are parallel to wave-number direction, i.e., $E_{11}(k_1)$ and $E_{33}(k_3)$. The laboratory study in near surface region also demonstrated this "bottleneck effect", which is explained by unbalanced spectral flux of energy at low wave-number with the rate of dissipation at dissipassive length scale [*Drazen and Melville*, 2009]. In this study, the spectral "humps" were not clearly observed. Although the high wave-number end in spectra is ~$O(10^3)$, the present data does not reach smallest length scale due to high turbulent level near the surface (dissipation rate is ~$O(10^{-4}$ $m^2/s^3)$).

(b) structure function fitting

Structure function (SF) fitting method can be used to estimate dissipation rate based on the Kolmogorov's second similarity hypothesis. The second order velocity structure function is defined as the covariance of difference in velocity between two points,

$$D_{ij}(r,z) = \mathrm{cov}[\Delta u_i, \Delta u_j] = \overline{[u_i(x,z) - u_i(x+r,z)][u_j(x,z) - u_j(x+r,z)]} \quad (6)$$

$D_{ij}(r,z) \approx 2\overline{u_i' u_j'}$ is a valid assumption for the case that velocity at two points are uncorrelated (r is larger than integral length scale of the turbulence) and the wave induced velocities at the two points are approximately equivalent (r is much smaller than the wavelength the surface waves). Figure 4-6 shows an example of second order structure function as the function of r in log-log scale for h = 1, 5 and 10 cm.

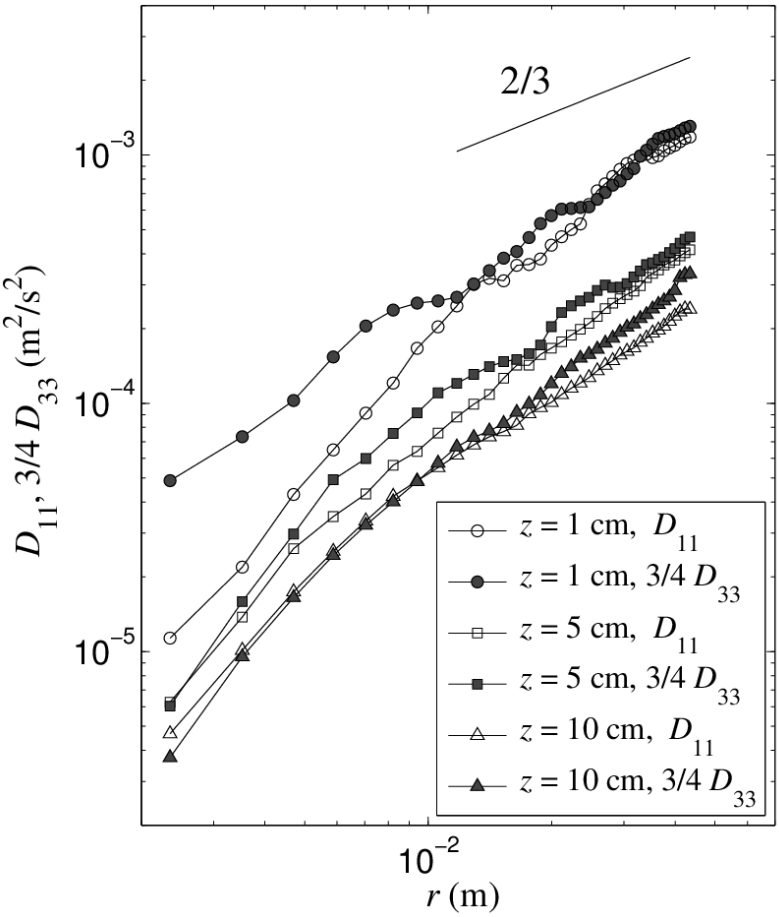

Figure 4-6: Second order structure function at different depth from the air-water interface (Run W1)

In the IR, the second order structure functions has the form,

$$D_{11}(r,z) = C_2(\varepsilon_{SF}(z)r)^{2/3} \tag{7}$$

In equation (7), $C_2 = 2.12$ [Sreenivasan, 1995] where the Reynolds number (based on Taylor micro-scale) is large enough. Practically, the dissipation rate can be resolved by linear fitting of second order structure function plotting with $r^{2/3}$ [J Gemmrich, 2010]. Both horizontal and vertical second order velocity structure function were used to estimate dissipation rate, denoted as ε_{SF11} and ε_{SF33}.

(c) Large eddy PIV method

Large Eddy PIV analysis approach was proposed by *Sheng et al.* [2000] to estimate dissipation rate of TKE, since PIV interrogation algorithm are based on the sub-window selection, which is similar to Large Eddy Simulation approach (LES). The idea is that the resolution of PIV velocity resolution (typically grid size for structured mesh) can be treated as the "resolved size" in LES. The assumption of the dynamic equilibrium of the energy transferred from the production length scale to the dissipation length scale is applied in large eddy PIV analysis. The instantaneous velocity field can be separated into two parts,

$$u_i = \overline{U}_i + \breve{u}_i \tag{8}$$

where $\overline{U}_i$ is the resolved scale velocity by PIV measurements, and $\breve{u}_i$ is the unresolved scale out of the resolution of PIV results. The LES equation can be obtained by filtering of the incompressible continuity equation and the Navier-Stokes equation,

$$\frac{\partial \overline{U}_i}{\partial x_i} = 0 \tag{9}$$

$$\frac{\partial \overline{U}_i}{\partial t} + \frac{\partial (\overline{U}_i \overline{U}_j)}{\partial x_j} = -\frac{\partial \overline{P}}{\partial x_j} + \nu \frac{\partial^2 \overline{U}_i}{\partial x_j^2} - \frac{\partial \tau_{ij}}{\partial x_j} \tag{10}$$

where $\tau_{ij} = \overline{u_i u_j} - \overline{U}_i \overline{U}_j$ is the sub-grid-scale (SGS) stress tensor. In this study, Smagorinsky model was applied to model SGS stress, given by,

$$\tau_{ij} = -C_s^2 \Delta^2 \left|\overline{S}\right| \overline{S}_{ij} \tag{11}$$

where Smagorinsky constant C_s = 0.17, and Δ is the window size of PIV analysis. For triangular mesh, Δ is defined,

$$\Delta = \sqrt{\frac{A_{ROI}}{N}} \tag{12}$$

where A_{ROI} is the area is region of interest, N is total number of triangular meshes. In this study, the LES filter size was calculated for each PIV image pair and averaged, that is, 0.095 mm.

The resolved scale rate of strain tensor $\overline{S}_{ij}$ is defined,

$$\overline{S}_{ij} = \frac{1}{2}\left(\frac{\partial \overline{U}_i}{\partial x_j} + \frac{\partial \overline{U}_j}{\partial x_i}\right) \tag{13}$$

For 2-D PIV analysis, only 4 of 9 components of $\overline{S}_{ij}$ can be measured, that is,

$$\frac{\partial \overline{U}_1}{\partial x_1}, \frac{\partial \overline{U}_1}{\partial x_3}, \frac{\partial \overline{U}_3}{\partial x_1}, \frac{\partial \overline{U}_3}{\partial x_3} \tag{14}$$

To estimate remaining terms of $\overline{S}_{ij}$,the continuity and isotropy is assumed such that,

$$\frac{\partial \overline{U}_1}{\partial x_2} = \frac{\partial \overline{U}_2}{\partial x_1} = \frac{\partial \overline{U}_2}{\partial x_3} = \frac{\partial \overline{U}_3}{\partial x_2} = \frac{1}{2}\sqrt{\left(\frac{\partial \overline{U}_1}{\partial x_3}\right)^2 + \left(\frac{\partial \overline{U}_3}{\partial x_1}\right)^2} \tag{15}$$

$$\frac{\partial \overline{U}_2}{\partial x_2} = -\frac{\partial \overline{U}_1}{\partial x_1} - \frac{\partial \overline{U}_3}{\partial x_3} \tag{16}$$

Therefore,

$$\left|\overline{S}\right| = \sqrt{2\overline{S}_{ij}\overline{S}_{ij}} \tag{17}$$

Based on PIV data and SGS model, the dissipation rate of TKE can be estimated by Reynolds averaged SGS dissipation rate,

$$\varepsilon_{LES} \approx \left\langle \varepsilon_{SGS} \right\rangle = -2\left\langle \tau_{ij}\overline{S}_{ij} \right\rangle \tag{18}$$

(d) comparison and discussion

From the different approaches discussed above, total six estimation of ε were evaluated. Mean value of ε for entire FOV is summarized in Table 2 and vertical profile is shown in figure 4-7. In general, the vertical profiles are very close in shape although there are not collapsed. The structure function fitting gives larger estimation than other methods. The overall difference of independent methods is quite small. The largest difference of estimation for entire FOV is between 1-D spectrum fitting at horizontal direction and structure function fitting at vertical direction (Table 2).

Table 4-2: comparison of mean dissipation rate of entire FOV estimation from different methods (m^2/s^3), Run W1

ε_D	ε_{LF11}	ε_{LF33}	ε_{SF11}	ε_{SF33}	ε_{LES}
1.371×10^{-4}	1.193×10^{-4}	1.431×10^{-4}	2.447×10^{-4}	2.899×10^{-4}	1.383×10^{-4}

For "direct method", least assumption is invoked in estimation of dissipation rate. On the other hand, this method is very sensitive to the PIV interrogation window size, since local velocity gradient is based on finite differences. In principle, more accurate estimation is expected for smaller grid size. However, the smaller window size increases measurement noise of velocity difference of adjacent grids. The tradeoff need to be determined with direct method estimation, which is extremely difficult in field measurements due to large variation of flow condition and spatial resolution of PIV system. In this study, direct method estimation is considered to be valid, since grid size of velocity vector map is averaged about 0.1 mm $< 5.5\eta = 0.14$ mm.

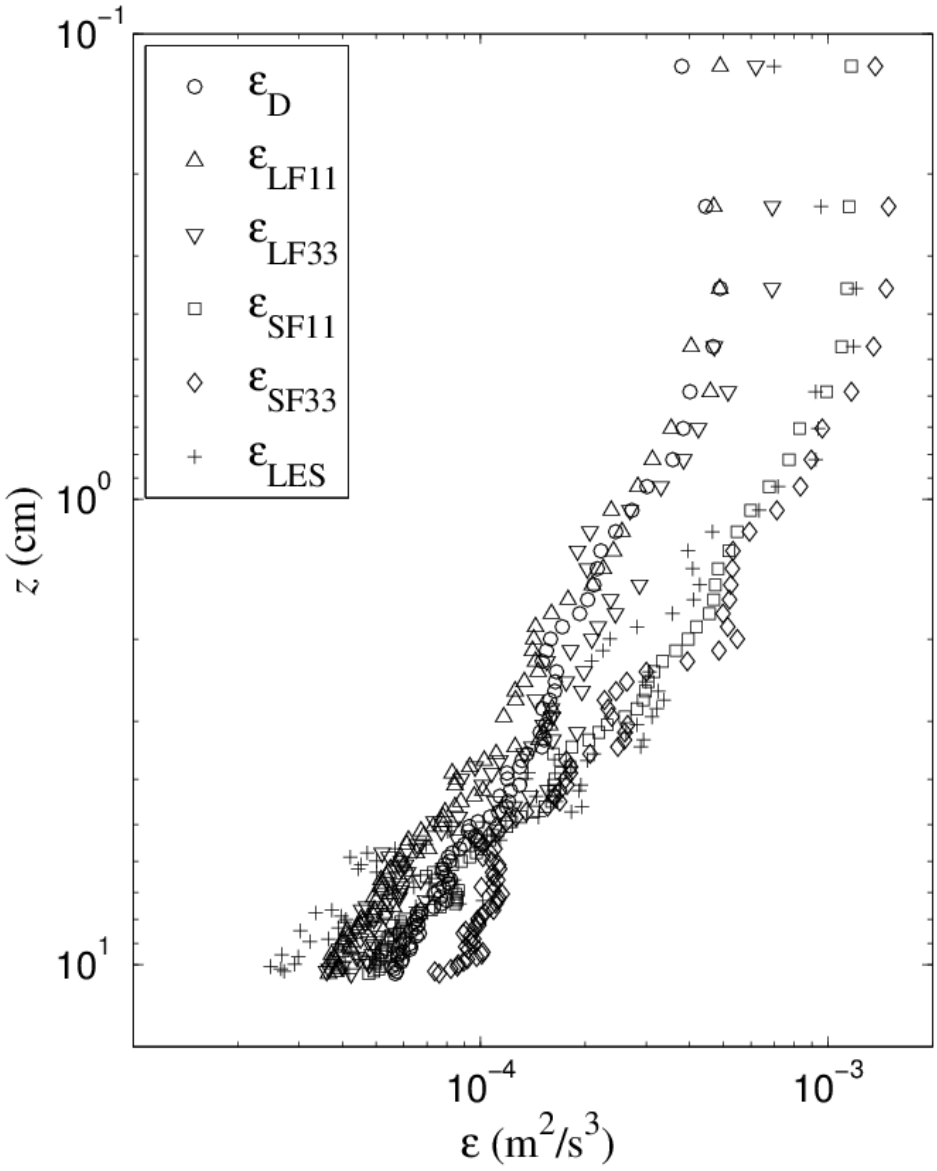

Figure 4-7: Comprasion of dissipation rate vertical profiles in log-log scale plotting from different methods (Run W1).

For 1-D velocity spectrum fitting and structure function fitting, the local isotropic turbulence is assumed in IR. Figure 4-5 shows a large region of IR indicated by -5/3 slope, which is need for 1-D velocity spectrum fitting. In theory, the spectrum fitting method is highly dependent on resolved IR. Typically, the high wave-number end of the

IR $k \approx 0.1/\eta$ (figure 4-5), while the low wave-number end of the IR varies depending on the turbulence anisotropy. For shear flow, the well defined IR relies on the turbulent level (i.e., Reynolds number), mean shear time scale and separation decades ($\log_{10}(L_s/\eta)$) between integral length scale (L_s) and Kolmogorov length scale (η) [*Bluteau et al.*, 2011]. If considering the near surface turbulence as wind-induced shear flow, the integral length scale is bounded by air-water interface hence L_s/η is small. Consequently, the width of IR is reduced by increasing low wave-number end. However, in this study, the IR is well observed even very close to the interface, such that the dissipation rate estimation from linear fitting of 1-D velocity spectrum is reliable. In the coastal ocean bottom boundary layer study [*Doron et al.*, 2001], they argued that the wave contaminate dissipation rate estimation based on spectral fitting, because the range of wave-number covered the scale of wave induced motion in their experiment. In this study, the turbulent level is quite strong and waves are fairly developed such that the dominant wave scale is out of the fitted wave-number range.

Similarly, structure function fitting method relies on the observation of IR. Since the velocity difference is calculated from large separation distance (~ O(cm)), the bias error issue from velocity spatial derivatives is negligible compared with direct method. The requirement of spatial resolution is relaxed and less sensitive to the sub-windows size of PIV analysis in SF fitting [*de Jong et al.*, 2009], therefore the dissipation rate estimation from SF fitting is an alternative approach, especially for coarse resolution measurement [*J Gemmrich*, 2010]. With a single beam Doppler sonar measurement, *J Gemmrich* [2010] implemented a vertical SF fitting to estimate near surface turbulence under breaking waves since no horizontal data available. Consequently, the structure

function data (4 data points at z = 0.03 m) near the interface is less and hence measurement noise would be a great issue. For PIV measurement, the instantaneous 2-D velocity map is available for calculating both horizontal and vertical SF to estimate turbulent dissipation (figure 4-6).

In the LES PIV analysis, the dissipation rate estimation is highly dependent on the sub-grid size Δ. Various Δ leads large uncertainty on dissipation rate estimates. *de Jong et al.* [2009] pointed out that dissipation rate estimation is independent of Δ in the IR. The advantage of LES PIV method is its suitability of the lack resolution measurement by modeling the kinematic viscosity by a sub-grid viscosity, where direct method is not reliable. Additionally, LES PIV method is independent on isotropic turbulence assumption in the IR rather than 1-D velocity spectrum fitting and SF fitting. The only matter is large separation of L_s and η. In figure 4-9, Δ = 0.095 mm gives close estimates with other direct and indirect methods.

In summary, all methods give close estimation on turbulence dissipation rate immediately below the developing progressive waves. The accuracy of different methods rely on the instrumentation setup and flow condition, such as, natural particle density, resolution of PIV analysis (depends on FOV and CCD size of camera), Reynolds number, turbulent anisotropy, etc. In field measurement, the measurement environment varies and cannot be well controlled before deployment. Therefore, a proper method should be chosen afterwards case by case. In principle, PIV measurement is more robust and accurate in estimating dissipation rate other than fixed point or two dimensional (time and single direction space) measurements.

4.4.3 Phase dependence on wave dominant field (W1)

Under breaking wave condition, the near surface turbulence is dominated by ejection of energy from breakers. Similarly, when waves occasionally break or micro-break by strong tangential stress on wave crest, strong turbulence is generated. Laboratory and field studies on phase dependence of turbulence dissipation rate confirmed higher turbulent level under wave crests [*J Gemmrich*, 2010; *K Siddiqui and Loewen*, 2010]. In laboratory study, PIV is an excellent technique to investigate phase dependent turbulent structure, since it can provide "direct" measurement of water surface in the case that the wave length is small enough compared of the FOV of PIV images [*Peirson*, 1997]. For resolving phase coverage, the FOV of PIV image is expected to be large to better estimate phase angle of sample area. This can be well controlled in laboratory studies. However, due to limitation of CCD array in the PIV camera system, the resolution for large FOV is consequently coarse. As the result, the PIV data substantially underestimate the dissipation rate, since 99% of dissipation takes place in the region of wave-number smaller than $5.5\eta^{-1}$ [*Cowen and Monismith*, 1997].

In field studies, it is almost impossible to accomplish the "direct" phase measurement with PIV since the sea surface wavelength is too large even under short fetch. In this case, Hilbert Huang Transform (HHT) [*N E Huang et al.*, 1998] can be used to resolve the phase angle and local amplitude for water elevation signals. The Hilbert transform of input signal $X(t)$ is defined,

$$H(t) = \frac{1}{\pi} P \int_{-\infty}^{\infty} \frac{X(t')}{(t-t')} dt' \qquad (19)$$

where P indicates the Cauchy principal value. $X(t)$ and $H(t)$ form the complex conjugate pair, so analytic signal $Z(t)$ can be defined,

$$Z(t) = X(t) + iH(t) = a(t)e^{i\theta(t)} \tag{20}$$

where, $a(t)$ is local amplitude and $\theta(t)$ is corresponding phase angle, defined as,

$$a(t) = \left(X^2(t) + H^2(t)\right)^{1/2} \tag{21}$$

$$\theta(t) = \tan^{-1}\left(\frac{H(t)}{X(t)}\right) \tag{22}$$

It should be noted that original Hilbert transform is only suitable for narrow banded signals. According to HHT, the raw near surface velocity data need to be decomposed into finite number of intrinsic mode functions (IMF), since the raw signal is broad banded. Empirical mode decomposition (EMD) method can be applied in the raw signal to get IMFs. After pre-process, the Hilbert transform on each IMF gives sharp identifications of imbedded structures. In this study, the HHT method is proposed to be applied to identify the phase dependence on near surface turbulence under propagating surface waves. For example, surface elevation signal can be represented in Hilbert expansion form,

$$\eta(t) = \sum_{n=1}^{N} a_n(t)\exp(i\theta_n(t)) \tag{23}$$

where N is total number of IMFs for decomposed signals.

However, for present PIV study, the water elevation wasn't recorded during experiment. Alternatively, the wave orbital velocity was used to analyze the phase angle for each instantaneous snapshot in this study. Assuming that the water elevation is due to wave orbital motion and uncorrelated with turbulence, local surface elevation can be

estimated from the horizontal velocity signal [*J R Gemmrich and Farmer*, 2004]. Since the PIV system is almost aligned with wave propagating direction, the determination of phase angle based on horizontal velocity is valid.

In practice, the horizontal velocity signal was averaged in entire FOV of PIV image since both wave length and height is large comparing to the FOV. Then, EMD method was applied to decompose the original signal into several IMF modes. In this study, totally 10 IMF modes were obtained in this pre-processing. Therefore, HHT can be applied to each mode to obtain the instantaneous local amplitude and phase angle. The dominant instantaneous wave frequency and phase angle can be obtained based on dominant IMF amplitude. Furthermore, to test the physical meaning of each IMF mode, a Fourier transform was performed to obtain the spectrum for individual IMF mode. To demonstrate the physical meaning of EMD method, figure 4-8 shows the horizontal velocity spectrum of the individual IMF modes in frequency domain from ADV data. The -5/3 slope line is also presented in figure to show the region of IR for ADV measurement. Total 18 IMF modes were obtained and the first 12 modes and original velocity signal were plotted in log-log scale. It should be noted that the ADV is moored on one side of the R/V, consequently the raw velocity signal contains the wave motion, turbulence, ship motion, and measuring noise. For separated IMF modes, each mode contains a certain time scale with increasing trend from the first to last mode. For example, the mode 1 interpret the most of turbulent dissipation range and measurement noise, the inertial sub-range is included in the first modes indicated by -5/3 slope. The time scale associated with dominant wave motion is located from mode 6 to 10.

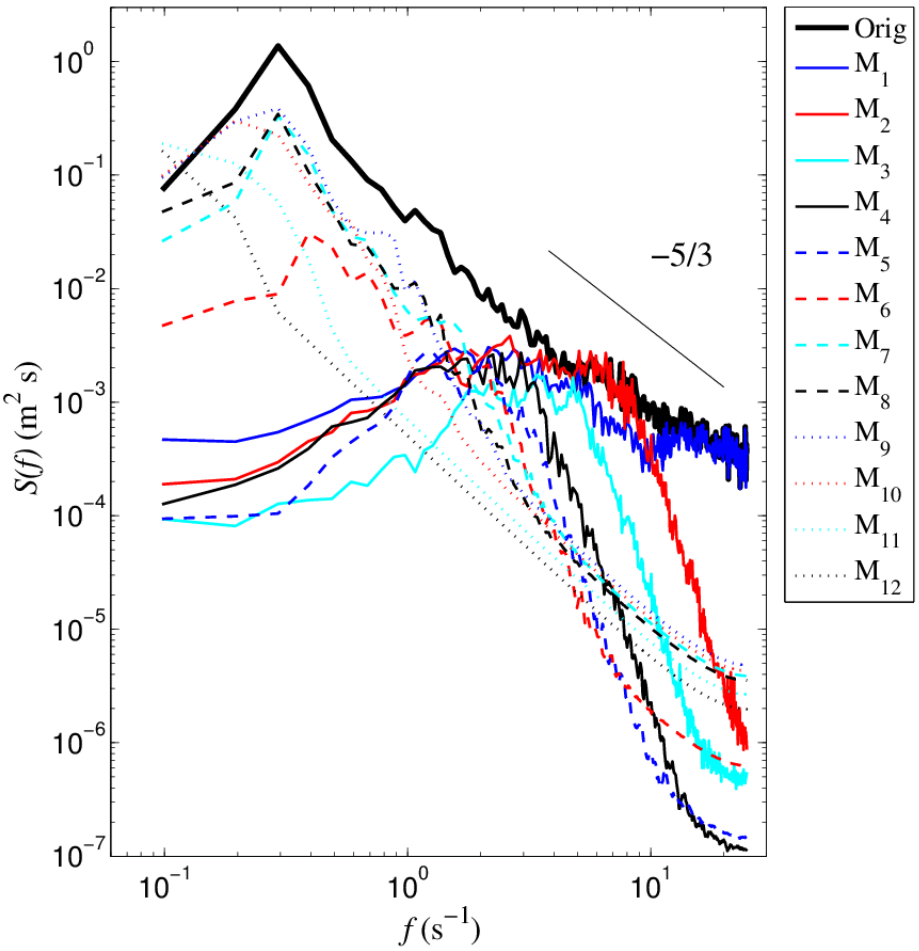

Figure 4-8: ADV horizontal velocity spectrum in frequency domain for seperated IMF modes from EMD method (Run W1)

For PIV data, similar trend is obtained but with less IMF modes (10 modes in total). It is noting that the sampling rate of PIV (8 Hz) is much smaller than ADV data (50 Hz), so that the time scale is not as well separated as ADV. In general, the most of energy are constricted in first two modes and large wave motion is contributed by mode 7. All other modes have no contribution to the local maximum amplitude $a_n(t)$. Based on the EMD methods and HHT process, 20 degree bin was selected to separate the region of

wave crest or trough for each PIV image. Then instantaneous dissipation rate was phase averaged corresponding to the dominant phase angle. Figure 4-9 shows the vertical profile of phase averaged dissipation rate in crest and trough region. Larger turbulent dissipation rate was observed under wave crest even without breaking waves. In this experiment, the enhanced dissipation rate under crest region is about 70% compared it in the trough region for entire FOV (vertically about 15 centimeters, over 7 minutes) of PIV analysis for 20 degree bin separation. It should be noted that only small portion of samples can be counted into the phase averaged calculation. Only about 10% of PIV images can be utilized to contribute phase average analysis for the following reasons. (1) a part of PIV images are excluded into vertical mapping because water surface is not shown in them; (2) another part of PIV images with very low water surface location in FOV cannot be counted into dissipation rate averaging, especially over 10 centimeters below the water surface; (3) the bandwidth of selected phase bin significantly affects the dissipation rate averaging. Larger bandwidth gives more samples at crest and trough region but less difference between dissipation rate, and vice versa. For example, the 40 degree bin leads the enhancement of dissipation rate at crest region decreasing to 24% but double the samples.

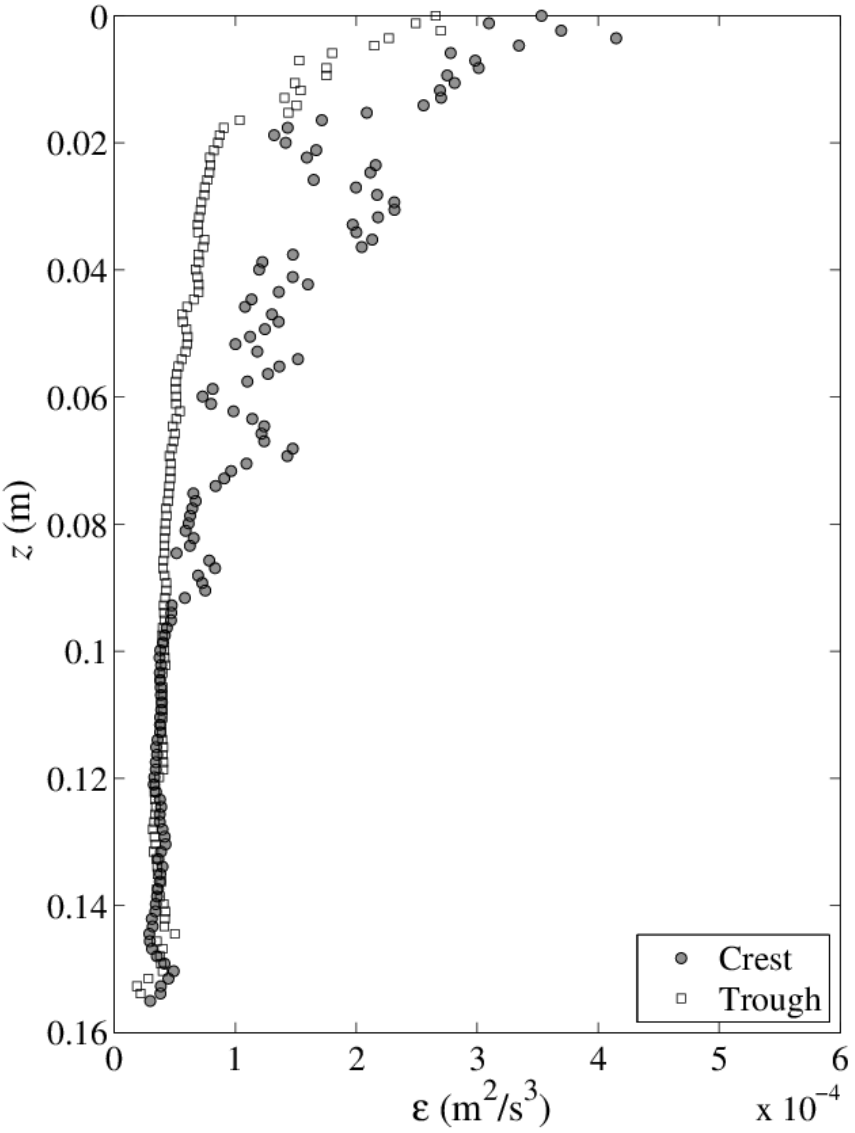

Figure 4-9: Phase dependence of vertical profile of TKE dissipation rate in crest and trough region (Run W1).

Enhanced shearing effect on water column with accelerating wind speed might be the direct energy source from the air side when approaching the wave crest. Strong turbulent energy might be transferred from micro-scale breakers associated with high level local vorticity. As shown in figure 4-8, the dissipation rate is strongly affected by

waves. In the meantime, the thickness of interaction layer should be distinguished with the different wave phase. The enhanced dissipation rate layer is thicker in the crest region (about 10 centimeters) than that in the trough region (about 2 centimeters).

4.5 Turbulence structure immediately below the air-water interface with existence of surface gravity waves

The existence of surface waves which is initialized by energy transported from wind renders complexities to the near surface turbulence characteristics and hence they are poorly understood. On the highly energetic ocean surface, the concept that turbulence is directly injected from breaking waves has been well accepted [*Terray et al.*, 1996]. Below the wave energy injection boundary, surface waves interact with current and turbulent structure in a complex way, leading to enhanced dissipation rate and wave related surface roughness [*Craig*, 1996; *Craig and Banner*, 1994].

The region where surface waves have great effect is denoted wave affected surface layer (WASL), in which the surface wave induced stress need to be account for transfer of energy among current, waves and turbulence [*Wuest and Lorke*, 2003]. In the wave breaking zone, the wave energy dissipates rapidly after breaking, following a power law relationship with time [*J R Gemmrich and Farmer*, 2004; *Rapp and Melville*, 1990]. During that process, the turbulent kinetic energy dissipation is independent with depth in the "turbulence injection" layer (thickness is about 60% of significant wave height) [*Terray et al.*, 1996]. In order to predict turbulent structure in WASL, the injection of TKE was introduced into one dimensional turbulent closure, which explains some field

observation results [*Burchard*, 2001; *Craig*, 1996; *Craig and Banner*, 1994; *Jones and Monismith*, 2008]. However, the model related parameters vary in a wide range while comparing with measured data such as surface roughness length, von Karman's constant, and wave energy factor [*Burchard*, 2001; *Jones and Monismith*, 2008].

In past several decades, the argument of similarity between near surface turbulence vertical structure and wall turbulence is of great interest. In wall turbulence, TKE production by Reynolds stress balance with viscous dissipation of TKE in the log-layer yield the law-of-wall (LOW) scaling,

$$\varepsilon_{LOW} = u_*^3(\kappa z)^{-1} \tag{24}$$

where κ =0.41 is von Kármán constant. Figure 4-10 shows the vertical profile of non-dimensional dissipation rate scaling with ε_{LOW}. All "T" runs seems like collapse together while runs W are very different.

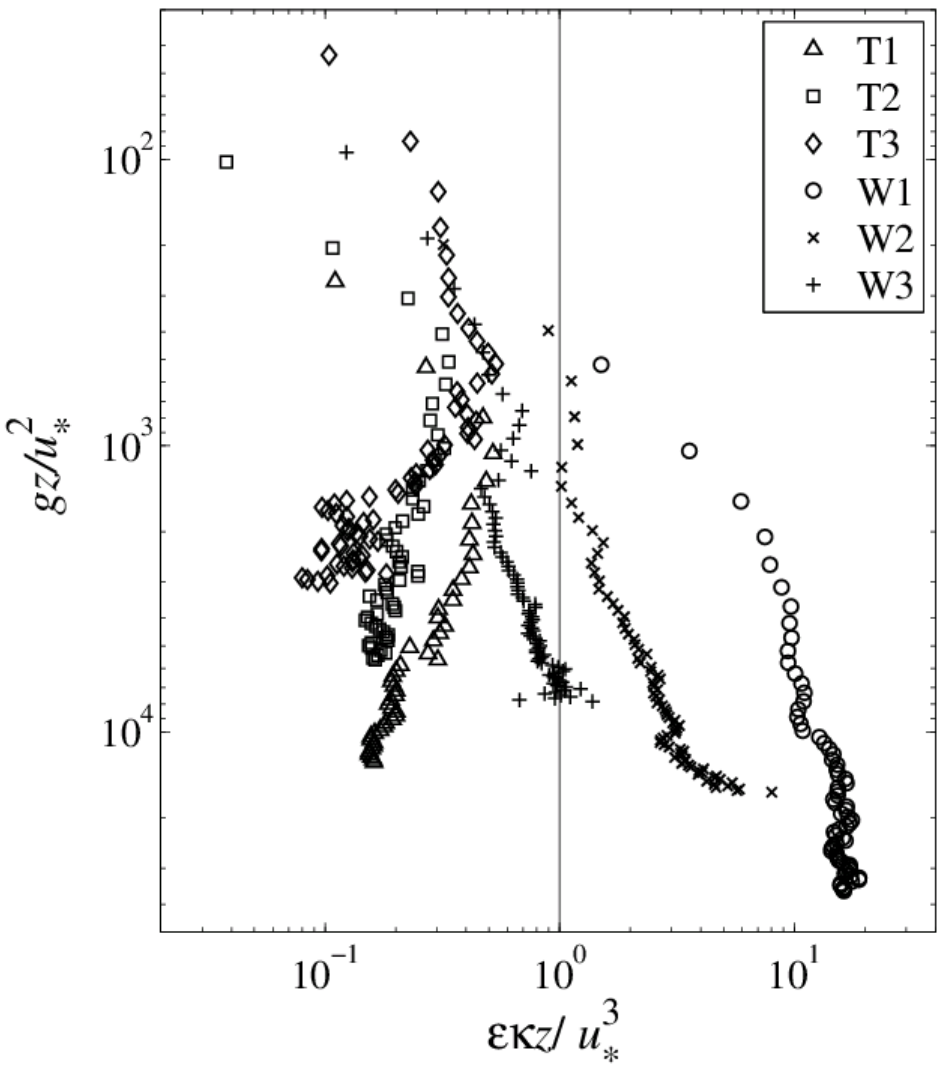

Figure 4-10: No dimensional plot of vertical profiles of dissipation rate, depth scales with the surface roughness length scale. The solid line indicates wall turbulence scaling.

The reason for scattered profiles is that energy is input downward from wind shear production for run T, which is similar to the classic wall turbulence generation mechanism. Therefore, the scaling of non-dimensional dissipation rate profile is close to $z = 1$. Moreover, because the energy of initiation of waves is also transported from wind

shear production such that the turbulent level for runs T is smaller than wall turbulence. The LOW applies for runs T indicated as the profiles collapse at the LHS of solid line (represent wall turbulence) in figure 4-10 with the scaling of friction velocity (calculated from wind drag law) and boundary roughness length scale. However, under sufficient effect of surface gravity waves, the momentum and energy input to turbulence is not only contributed from surface skin friction due to wind shear but also contributed from wave produced fluctuations of pressure and interactions with wave and current [*Anis and Moum*, 1995].

As can be seen in figure 4-10, the profiles scatter in the non-dimensional plotting with scaling of wall turbulence parameters for run W. Many hypotheses were made to explain the scaling rule of dissipation rate with depth in WASL. Stokes drift distort turbulence in surface layer and hence induced additional shear stress, which leads to a scaling rule of $\varepsilon_w \sim e^{2kz}$, where $k = 2\pi / L$ is wave number [*C J Huang and Qiao*, 2010]. In this case, dissipation decays with respect to depth faster when wave length is small. With the development of surface gravity waves, the decaying become slower and slower and reaches equilibrium state for mature sea. This relation was proved in the field observation with the depth on the order of meters [*C J Huang and Qiao*, 2010]. However, in the present study, this relation failed to predict dissipation rate at the region immediately below the air-water interface. The possible reason is that the turbulence generation mechanism very close to water surface combined the effect of wind stress, wind induced turbulence and wave-turbulence interaction. In the field observation of *Anis and Moum* [1995], two fitting were applied to extrapolate the surface dissipation rate. For their data, the surface dissipation rate from upper 6 meters fitting is 10 times larger than

that below 6 meters. However, the profile immediately below the interface was not provided for comparison.

Once wave amplitude reaches a critical value where breaking occurs, the wave energy injects to TKE directly with a constant vertical dissipation rate layer of 1-2H_s [Melville, 1994; Terray et al., 1996]. The enhanced dissipation rate due to wave breaking is about 1-2 orders of magnitude higher than ε_{LOW} [*Agrawal et al.*, 1992]. Additionally, with the interaction of developing waves or wave induced another turbulent source, the TKE dissipation rate enhancement is one order of magnitude higher than ε_{LOW} even without breaking. Meanwhile, the interaction maintains high turbulent level away from interface such that the slow decay rate comparing with LOW scaling. Consequently, the ratio of dissipation rate with ε_{LOW} in the wave dominant case become larger and larger as depth increases from the interface.

In this chapter, the concept of energy injection was adopted from the surface as described in *Craig and Banner* [1994]. In the original presentation of energy injection, the injection of turbulent kinetic energy comes from the wave breaking. In this study, no significant wave breaking was observed during the measurements. However, the micro-scaling wave breaking, which is featured as superposition of bore-like crest with capillary waves riding along the forward face of longer waves [*M H K Siddiqui et al.*, 2004], was observed at the water surface. In light of strong vorticity induced by existence of micro-breaking waves at the air-water interface [*M H K Siddiqui et al.*, 2004], I suggest to analyze data following the similar way. Therefore, the original model for turbulent structure in WASL (below the wave breaking zone) should be directly adopted to this

study as modeling of turbulent structure immediately below the air-water interface without significant wave breaking.

One dimensional Mellor-Yamada 2.5 level turbulent closure model was employed with an additional transport term in TKE equation, i.e., $-\frac{\partial}{\partial z}\left(lqS_q \frac{\partial}{\partial z}\left(\frac{q^2}{2} \right) \right)$, indicating the downward transport of energy from surface. In this model, turbulent kinetic energy flux from air-sea interface can be approximately scaled with the cubic of water side surface friction velocity u_* such that,

$$\frac{\partial}{\partial z}\left(lqS_q \frac{\partial}{\partial z}\left(\frac{q^2}{2} \right) \right) = \alpha u_*^3 \tag{25}$$

where S_q is model constant; q is turbulent velocity scale, defined as square root of twice the TKE, $q = \sqrt{2k}$; l is mixing length, defined as $l = \kappa\left(z_0 + |z|\right)$; and wave energy factor α is related to sea state. For fully developed sea, $\alpha \approx$ 100-150 [*Craig*, 1996].

Craig [1996] provided the analytical solution for steady-state as follows,

$$q = u_* \left(b^3 + \alpha c \left(\frac{z_0}{z_0 + |z|} \right)^{3m} \right)^{1/3} \tag{26}$$

in which,

$$b = \left(\frac{B}{S_M} \right)^{1/4},\ c = \left(\frac{3B}{S_q} \right)^{1/2},\ m = \left(3B\kappa^2 S_q \right)^{-1/2}$$

In this paper, the model parameters were set as follows,

B = 16.6, S_q = 0.2, S_M = 0.39; α = 150, κ = 0.4 and surface roughness length $z_0 = 0.6H_s$

From the relation $\varepsilon = \frac{q^3}{Bl}$, the turbulent dissipation rate at WASL can be written as,

$$\varepsilon = \frac{u_*^3}{B\kappa\left(z_0 + |z|\right)}\left(b^3 + \alpha c\left(\frac{z_0}{z_0 + |z|}\right)^{3m}\right) \tag{27}$$

Figure 4-11 plots the non-dimensional dissipation rate profiles for all runs in log-log scale with the analytical solution of 1-D turbulent closure model in WASL. The dashed line represents rigid boundary without wave affect and solid line represent wave effect due to downward transport from the air-water interface. In this non-dimensionalization scheme, dissipation rate is normalized with u_*^3 / z_0, where surface roughness length scale z_0 is related with significant wave height.

As can be seen in figure 4-11, when wind shear is large, the normalized dissipation rate tends to shift to the left due to large friction velocity. Although wave parameter is enclosed in this scheme, however, the profiles still scatter with each other. In this model, the energy flux superimposed from air-sea interface is also scaled with wind shear, based on the assumption that wave energy is extracted from wind input. In figure 4-11, the solid line represents the cases of fully developed sea, but the measured profiles represent different combinations of wind and wave parameters.

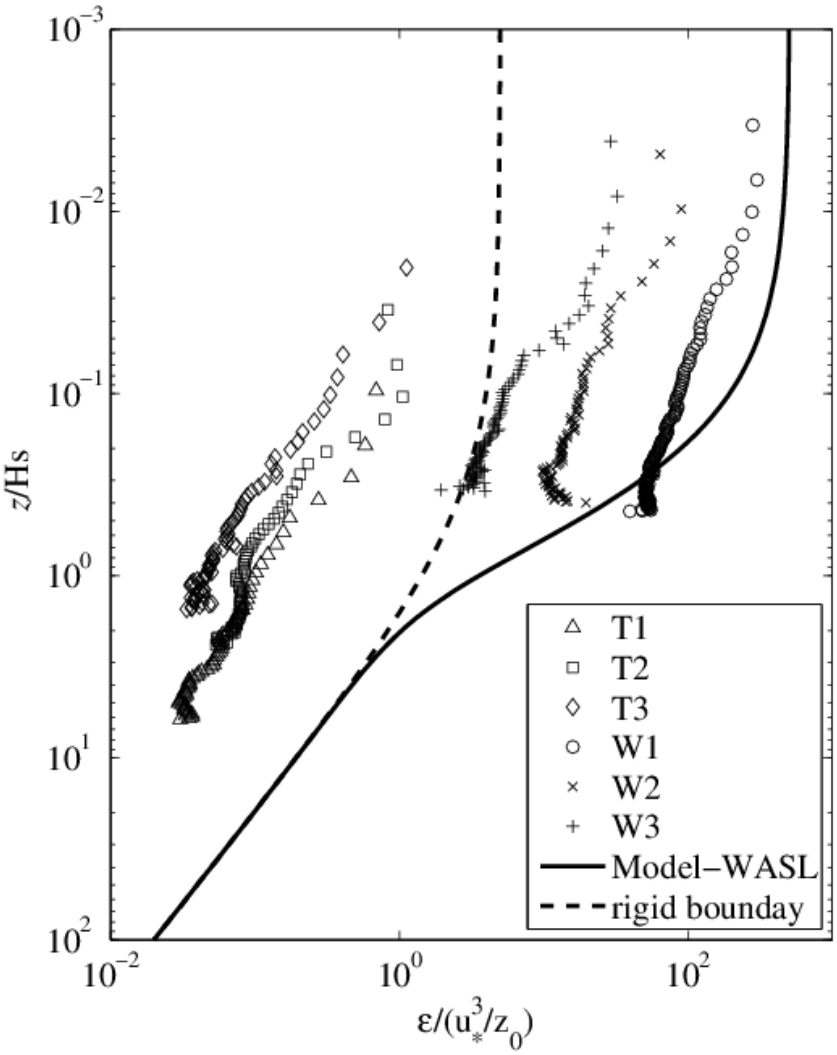

Figure 4-11: No dimensional plot of vertical profiles of dissipation rate, depth scales with the significant wave height. The dash line indicates wall turbulence scaling. The solid line indicates analytical solution of dissipation rate profile in the WASL model.

Terray et al. [1996] provided a dissipation rate scaling scheme, considering the development of wind waves, i.e., represented by wave age c_p/u_*. The vertical profiles of turbulent dissipation rate seem to collapse towards a universal form (figure 4-12), that is,

$$\frac{\varepsilon H_s}{\beta u_*^3} = A\left(\frac{z}{H_s}\right)^n \tag{28}$$

According to the linear regression in the log-log scale, the coefficients are determined as A = 0.017 and n = -0.83. In the field observation of *Terray et al.* [1996], A = 0.15 and n = -2, which corresponds to wave affected surface layer under breaking wave condition. *M H K Siddiqui and Loewen* [2007] measured dissipation rate profiles immediately below the air-water interface using PIV in a laboratory wind wave facility, and they observed a two-layer structure. At the surface layer immediately below the air-water interface, n = -0.7 was found in their laboratory experiments, which is close to n = -0.83 in the field observations. However, they did not provide the coefficient A in this layer. Below this layer, they found A = 0.035 and n = -2, which is in agreement of the second layer of *Terray et al.* [1996] but with a different coefficient A. *M H K Siddiqui and Loewen* [2007] argued that A is a function of wave age. In their laboratory experiments, the thickness of this top layer is 0.4 H_s. However, in this field observation, I did not see such two layer structures within 15 centimeters below the air-water interface. The top layer reaches up to $6H_s$ during the wind wave initiation period (i.e., "T" cases).

For the datasets presented in this chapter, wave age is only a characteristic parameter to describe the state of wind and wave condition. The full wave spectrum should be investigated due to the unknown interaction effect between turbulence and waves with a variety of spectral bandwidth. Although incomplete, the scaling law of equation (28) indicates that the energy transfer mechanism immediately below the air-water interface is similar to the injection diffusion effect from the wave breaking zone. Therefore, I suggest that micro-scale breaking wave delivers the turbulent kinetic energy from the surface "skin" and then diffuses downward to water column. The strength of

micro-breaking should be determined by the combination effects of wind and wave parameters (e.g. wind speed, wave height and wave age).

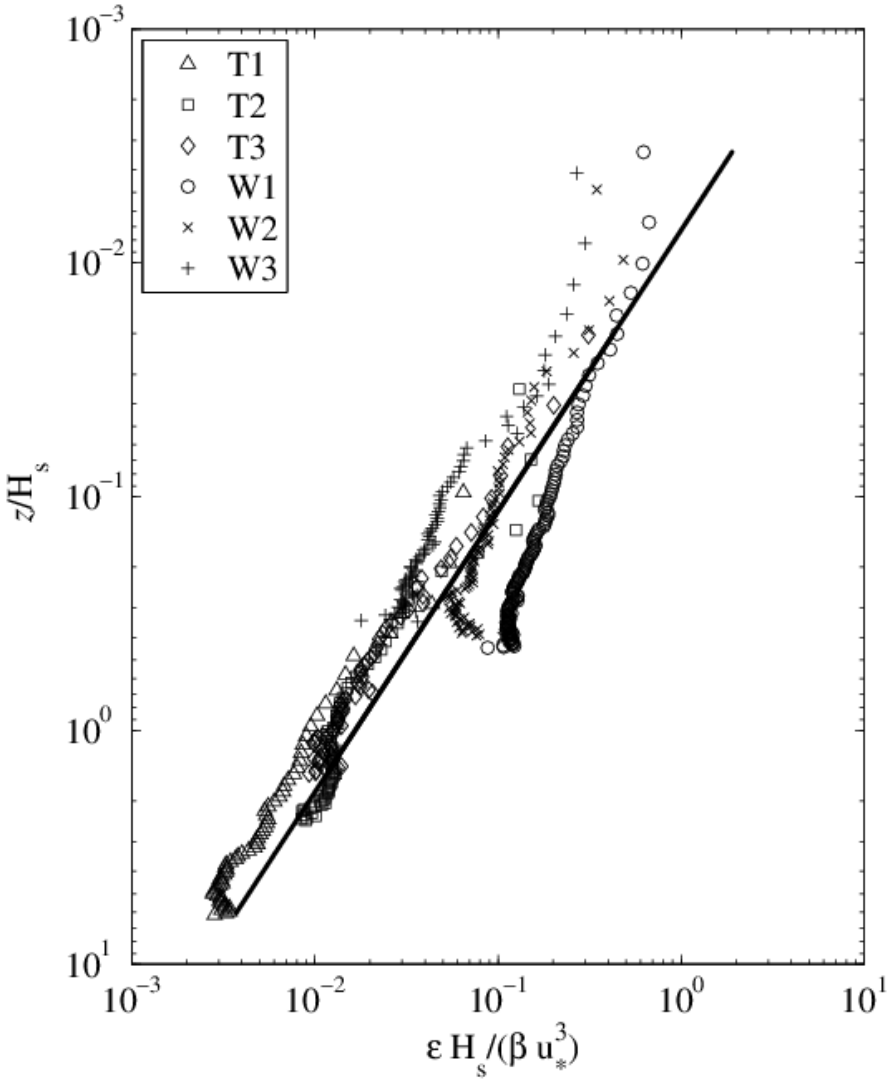

Figure 4-12: Vertical profiles of turbulent dissipation rate sacled with the friction velocity, significant wave height and wave age, following *Terray et al.* [1996]. The solid line is the linear regression line with the least square fit.

4.6 Small scale turbulence effect on air-sea gas transfer

Large amount of air-sea gas transfer occur at the presence of wave breaking events, when the air bubbles entrain into sea surface. Whitecap coverage was used to parameterize the gas exchange during wave breaking events, since bubble effects on gas exchange are dominant [*Woolf,* 2005]. The enhancement of gas transfer is also correlated with the enhanced turbulent level with high dissipation associated with breaking [*Melville,* 1996]. Wind speed or wind shear is more universal parameters for estimating global air-sea gas exchange [*Deacon,* 1977; *R Wanninkhof,* 1992]. However, in low wind shear condition, the mechanism of gas transfer across the air-water interface is dominated by near surface turbulence, represented by turbulent dissipation rate following small scale eddy model [*Zappa et al.*, 2001; *Zappa et al.*, 2007].

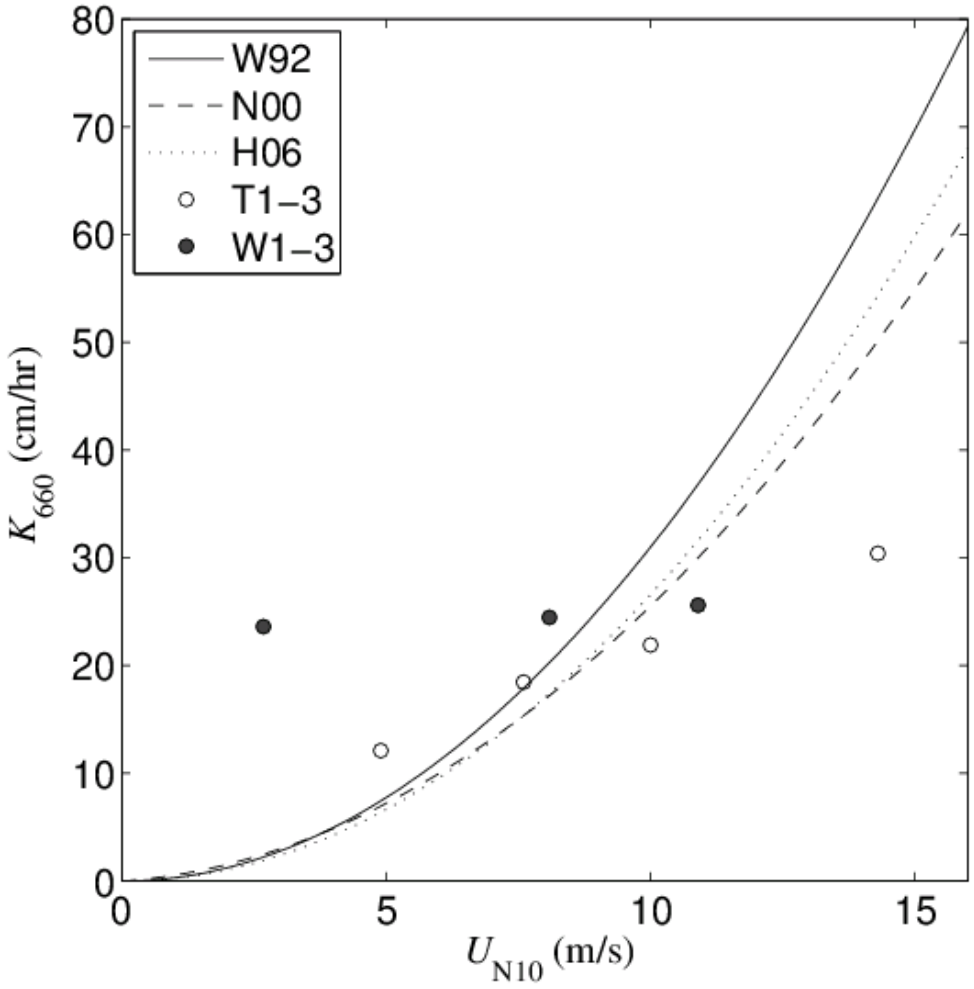

Figure 4-13: Comparison between wind speed model and small scale eddy model on estimating transfer velocity of CO_2 flux across the air-sea interface.

The factor α = 0.419 is a fitted constant from several environmental conditions [*Zappa et al.*, 2007]. The dissipation rate in small scale eddy model is measured value at z = 1cm below the air-water interface for all runs. For three wind speed models, W92 represents the short term or steady wind speed condition estimation [*R Wanninkhof*, 1992]; N00 represents the coastal area measurement in fetch limited environments [*Nightingale et al.*, 2000]; H06 relationship is obtained from SOLAS Air-Sea Gas

Exchange (SAGE) experiment in Southern Ocean [*Ho et al.*, 2006b]. The comparison in figure 4-13 shows close estimation of transfer velocity at moderate wind speed (5-11 m/s) with all models for Runs T1-2 and W2-3. Since runs T were conducted in the Milwaukee Harbor with almost "zero-fetch" condition, the dissipation rate can be considered as a representative of wind shear with very small wave effects. Transfer velocity estimation based on dissipation rate match the wind speed model very well except for T3 at wind speed of about 15 m/s. In T3, the result of small scale eddy model might be underestimated for following reasons. First, the smallest turbulent eddy scale turned to be very small consequently the PIV resolution is not fine enough to cover the dissipation range of energy cascade. Thus, near surface dissipation rate is underestimated by measurement limitation. Second, for intermittent wind gust, air bubbles enter the water column hence PIV analysis cannot be accomplished. In this situation, two consequences lead to underestimation of gas exchange: (1) the excluded contaminated PIV images contains significant intermittent turbulent dissipation directly injected from breaking waves, which lead to underestimation of near surface dissipation rate; (2) air bubble dominant gas exchange mechanism such that small scale eddy model estimation is not accurate.

For field experiments on air-sea gas exchange, most of data (both coastal area and open ocean) are concentrated in the wind speed range of 5-12 m/s [*Ho et al.*, 2011c]. In such environmental condition, the discrepancy of large amount empirical wind speed models and other theoretical methods (e.g. wind shear model represented by surface shear velocity) is acceptable. In low wind condition, wind speed modeled transfer velocity decreases rapidly since its quadratic relation with wind speed. However, near surface

turbulence controls gas exchange mechanism and small scale eddy model gives the better estimation of interfacial transfer velocity. As discussed above, the near surface turbulent dissipation is significantly enhanced by interaction with surface gravity waves or associated with micro-breaking events. As evidenced for Run W1 in figure 4-13, the transfer velocity estimated by small scale eddy model is almost 10 times larger than that of wind speed models for fully developed sea with weak wind speed. Therefore, the wind speed model could significantly underestimate global air-sea gas transfer, since the sea surface is covered by low to moderate wind condition most of the time [*Monahan*, 2006]. For example, 5 years statistical data of Martha's Vineyard Coastal Observatory (MVCO) from 2001 to 2005 shows the predominant wind speed distributed at 2-6 m/s in July-August with direction of costal ocean, which means infinite fetch enable the growth of surface waves and its impact on near surface turbulence. To conclude, I recommend that this significant enhancement should be considered into global air-sea CO_2 flux estimation in the future.

Chapter 5

Interfacial Gas Transfer Velocity and its Relationship with Statistics of the Near Surface Turbulence

5.1 Instrumentation and methods

In this chapter, a free floating PIV (FPIV) system and a floating chamber were employed to measure near surface turbulence and CO_2 flux across the air-water interface on Lake Michigan under different wind and wave conditions. Table 1 summarizes the environmental parameters in this study.

Table 5-1. Summary of environmental parameters in this study

Run	Wind speed (m/s)	Wind gust (m/s)	Air temperature (°C)	Water temperature (°C)
$T1-1$	2.35	3.04	7.74	11.45
$T1-1C$	3.21	4.23	7.11	9.13
$T1-2C$	3.21	4.39	7.32	9.13
$T1-3C$	2.74	3.94	7.31	9.13
$T2-1$	2.68	2.68	7.22	no data
$T2-2$	1.34	1.34	7.22	no data
$T2-3$	0.45	0.34	7.22	no data
$T2-4$	7.15	7.15	20.0	no data
$T2-5$	6.71	6.71	20.0	no data
$T2-1C$	calm	calm	6.11	no data
$T2-2C$	calm	calm	6.11	no data
$T2-3C$	calm	calm	6.11	no data
$W1-1$	10.90	14.13	22.58	18.78
$W1-2$	11.64	14.95	22.31	18.78
$W1-3$	7.84	10.19	21.09	18.78
$W1-4$	7.15	10.17	19.82	18.78
$W1-5$	8.69	12.58	19.16	18.78
$W1-1C$	8.81	10.74	18.34	17.25
$W1-2C$	8.35	11.07	18.24	17.25
$W1-3C$	7.78	10.02	18.10	17.25
$W2-1$	8.09	8.60	13.72	8.9
$W2-1C$	6.52	7.70	13.27	8.9

5.1.1 Free floating PIV system

In order to quantify the turbulent statistics immediately below the air-water interface, *Wang et al.* [2013] developed an *in situ* PIV system which is designed to follow the wavy water surface during measurement. Successful deployments have been made on Lake Michigan and detailed description of the FPIV can be found in Chapter 3 of this dissertation.

Different than the bottom PIV measurements [*Liao et al.*, 2009], the floating PIV measurements are ideally made based on a Lagrangian coordinate system. In theory, the system should follow the wavy surface perfectly to clearly track the air-water interface in each image pair. However, the wave following feature is not perfectly performed due to

the inertia of the system, especially in the sea swell condition. Therefore, not all the PIV images appropriately capture the air-water interface. The PIV images without the water surface were discarded in data analysis process. In this study, the number of the discarded images is small compared with the total images acquired (< 2% in relatively small wave fields, i.e. "T" conditions; < 20% in relatively large wave fields, i.e. "W" conditions, see section 3 and Table 1 for detail of "T" and "W"). (note: the "T" and "W" condition presented in Chapter 5 is independent with that in Chapter 4).

5.1.2 Floating chamber system

The floating chamber system was used to measure the flux CO_2 based on mass balance inside of chamber,

$$F(t) = S^{-1}\frac{dC}{dt} \tag{1}$$

where C is the moles of CO_2 in the chamber at time t, and S is the surface area of water covered by the chamber. The time interval, dt, is 5 seconds. A time series of the transfer velocity of CO_2 across the air-water interface, $k_{600}(t)$, was calculated from this flux measurement by solving the standard equation for CO_2 flux,

$$k_{600}(t) = \frac{F}{K_0(p\mathrm{CO}_{2w} - p\mathrm{CO}_{2a})}Sc^{1/2} \tag{2}$$

where the gas transfer velocity is normalized to the value of CO_2 at 20 ℃ for fresh water (Sc = 600), Sc is the Schimidt number, F is flux of CO_2 obtained evaluating the rate of change of CO_2 concentration in the FC from equation (1), K_0 is the solubility coefficient

of CO_2 in water, pCO_{2w} and pCO_{2a} are partial pressure of CO_2 in water and air, respectively. The detailed description of the FC can be found in *Wang et al.* [2013b].

5.2 Measurements

5.2.1 Study sites

All field measurements for this study were conducted on Lake Michigan and Milwaukee river harbor from September to November 2012. Two primary categories were selected in this study with and without wave motions. The environmental conditions without large wave motion were conducted in Milwaukee river harbor, denoting "T" to refer near surface turbulence measurements. For relatively large wave motion, I denote "W" to emphasize the wave effect. All "W" runs were carried out on Lake Michigan (outside of the Harbor). Run T1 was carried out in the harbor but with relatively large surface area. Run T2 was conducted in an embayment of Kinnickinnic River connected to the harbor.

5.2.2 Sampling

In order to quantify the gas exchange/near surface turbulence relationship and evaluate the artificial effect of the FC on near surface turbulence, two configurations ("covered" and "un-covered") are designed in this study. In "covered" configuration, the FPIV is placed underneath the FC to measure the dissipation rate in the sample area

where transfer velocity is measured. Figure 5-1 shows a picture of "covered" configuration of FPIV/FC system. In this configuration, simultaneous measurement of the FC and the FPIV were carried out to investigate the relation of interfacial gas exchange and near surface turbulence. Continuous FC measurement over a short period (about 10 minutes) was made and data was recorded at each 5 seconds. In the meantime, the FPIV measured the turbulence inside of the FC covered area. The clocks of the two systems were synchronized before the deployments. The sampling frequency of the FPIV measurement (6-8 Hz) is much higher than that of the FC, because a large amount of PIV images were acquired for statistic analysis. During the "covered" measurements, the FPIV is assigned to sample for several bursts with each burst about 3-5 min. The "covered" bursts are labeled "C". For example, T1-2C means the second PIV burst under the "covered" condition at deployment T1.

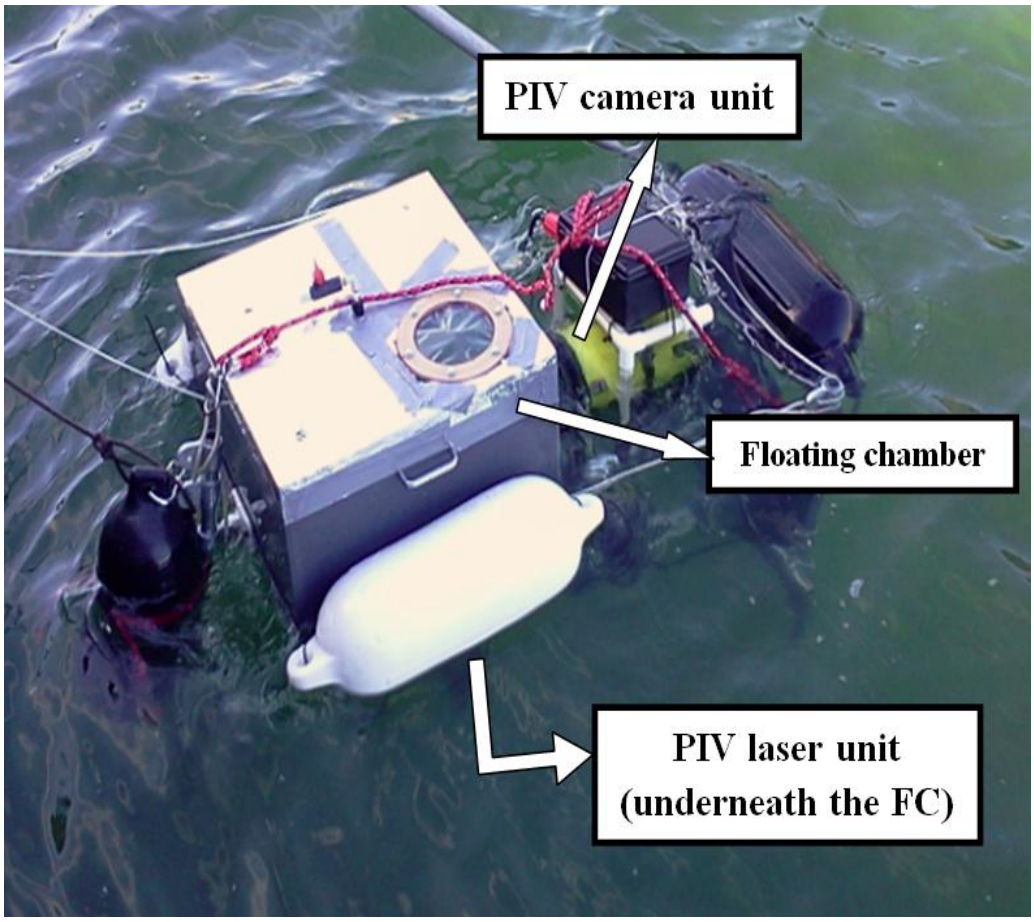

Figure 5-1: UWMPIV/FC system in Lake Michigan

In "un-covered" configuration, the FC was removed from the UWMPIV to measure the dissipation rate at natural aqueous boundary layer. Several bursts were conducted as well for statistical consistency. It should be noted the "un-covered" measurements were carried out immediately before or after the "covered" measurements. Then comparison was made to determine the artificial turbulence induced by FC. In this configuration, sample label rule applies except for "C". For example, W2-1 means the first PIV burst under "uncovered" condition at deployment W2.

In total four series of experiments were conducted in this study. However, the gas flux data of run W1 is not available due to malfunction of the FC during the experiment.

Therefore, the simultaneous measurements of the FPIV and the FC were not achieved. Fortunately, the FC disturbance effect on near surface turbulence can also be evaluated for this run.

5.2.3 Environmental data

Wind speed data were generally obtained from nearby observation tower. For run T2, the wind speed was measured by a wind sensor installed on the top of a building (maintained by Great Lakes WATER Institute). The height of the wind sensor is approximately 10 meters above the water surface. It should be noted that the accuracy of wind speed data for run T2 is questionable, because the "sheltering effect" might cause the variation of wind speed at the experiment location. Consequently, the wind gust might dominate the surface turbulence statistics for T2. For all other runs, the experiment sites were close to one of the NOAA real time meteorological observation sites (43°02'44''N, 87°52''44''W). The meteorological data were retrieved from this observation site. Water temperature was measured before and after each run for both "covered" and "un-covered" configurations. Average water temperature was taken for each run.

5.3 Results and discussion

5.3.1 Small scale eddy model (SEM)

Despite many sources generating turbulence close to the air-water interface in this study (current, wind shear, surface waves and artificial effect of FC), the dissipation rate is directly estimated with the *in situ* FPIV system, following "direct method" [*Doron et al.*, 2001],

$$\varepsilon_D = 3\nu\left[\overline{\left(\frac{\partial u'}{\partial x}\right)^2} + \overline{\left(\frac{\partial w'}{\partial z}\right)^2} + \overline{\left(\frac{\partial u'}{\partial z}\right)^2} + \overline{\left(\frac{\partial w'}{\partial x}\right)^2} + 2\overline{\frac{\partial u'}{\partial z}\frac{\partial w'}{\partial x}} + \frac{2}{3}\overline{\frac{\partial u'}{\partial x}\frac{\partial w'}{\partial z}}\right] \quad (3)$$

From the measured dissipation rate data, one can compare the time series of predicted transfer velocity based on the SEM with the measured one by the FC. Figure 5-2 shows the direct comparison of predicted *k* values with measured ones for one burst in T1, T2 and W2. The raw dissipation rate data was smoothed every 2 seconds in the plot. All *k* values were converted to transfer velocity of CO_2 at 20 ℃ in freshwater system (Sc = 600). The coefficient α is determined based on the best fit of correlation between measured *k* and the SEM predicted during the period of each burst. In figure 5-2, α is determined to be 0.2604, 0.1045 and 0.4298 for run T1, T2 and W2 respectively. Figure 5-2 shows good match between measured transfer velocity with the SEM prediction in such short time scale, especially for run T1 and T2.

The coefficient α varies case by case, although the dissipation rates are all taken immediately below the air-water interface. α for two T runs is much smaller but run W2 is close to the best fit value of *Zappa et al.* [2007] (α = 0.419) and *Vachon et al.* [2010] (α

= 0.43). In their experiments, the dissipation rate was measured at short distance below the water surface (tenth of centimeters). In figure 5-2, the applied dissipation rate was measured directly at the air-water interface. The measurement results on vertical dissipation rate profiles show a significant gradient close to the water surface (i.e., Chapter 3 and 4). Therefore, small α at T1 and T2 is not surprising, since strong turbulence present immediately below the water surface.

Moreover, it should be noted that α increases monotonically with the value of transfer velocity. The possible explanation is that α is not a constant value. It seemed to increase with the intensity of turbulence represented by near surface dissipation rate, or Reynolds number.

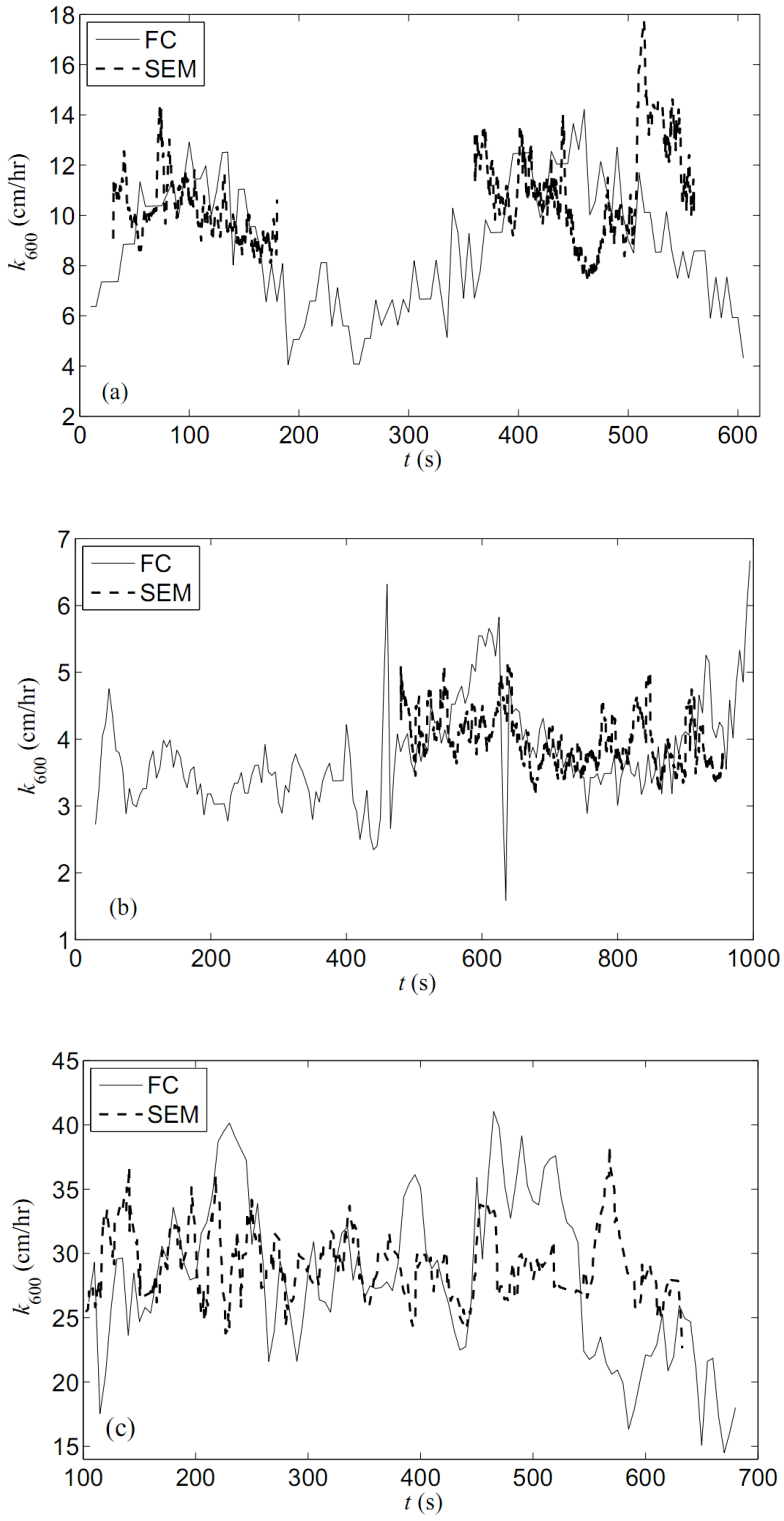

Figure 5-2: Direct comparison of time series of measured transfer velocity with the SEM prediction, dissipation rate data is measured at the air-water interface, (a) T1C (b) T2C (c) W2C

If considering the SEM as a universal model for gas transfer and parameterized by ε, ν and D only, the coefficient α may only be a function of ε. In light of this hypothesis, I re-analyzed the data to seek an empirical relation between α and ε. Figure 5-3 plots the relationship between the model coefficient with the near surface dissipation rate if there is any. Data from laboratory experiments of *Chu and Jirka* [2003] and from field observations of *Vachon et al.* [2010] were also included for analysis. For consistence with the field observations of *Vachon et al.* [2010], the dissipation rate represented in figure 5-3 were all evaluated at z = 10 centimeters away from the water surface. High frequency data measured in this study was broken into several sections based on the variation of ε, resulting in 16 pairs of averaged k_{600} vs. ε. The coefficient α was then calculated following equation (1) for each pair. Results from others were digitized and the coefficient α was also calculated for every data point. Good correlation was observed between α and logε in figure 5-3, with the coefficient of determination R^2 is 0.47 for all available data, and R^2 = 0.93 for our data alone. The log-linear regression was also made to the data when dissipation rate evaluated at the water surface (z = 0.5 cm) (see small panel in figure 5-3). Good correlation was also observed at the surface (R^2 = 0.91). This experiment also found that the vertical dissipation rate profile tends to be uniform at the short distance away from the water surface under the effect of the FC, compared with the natural aquatic systems ("uncovered" measurements). Therefore, the relationship between coefficient and dissipation can be evaluated while dissipation rate was measured at short distance away from the interface.

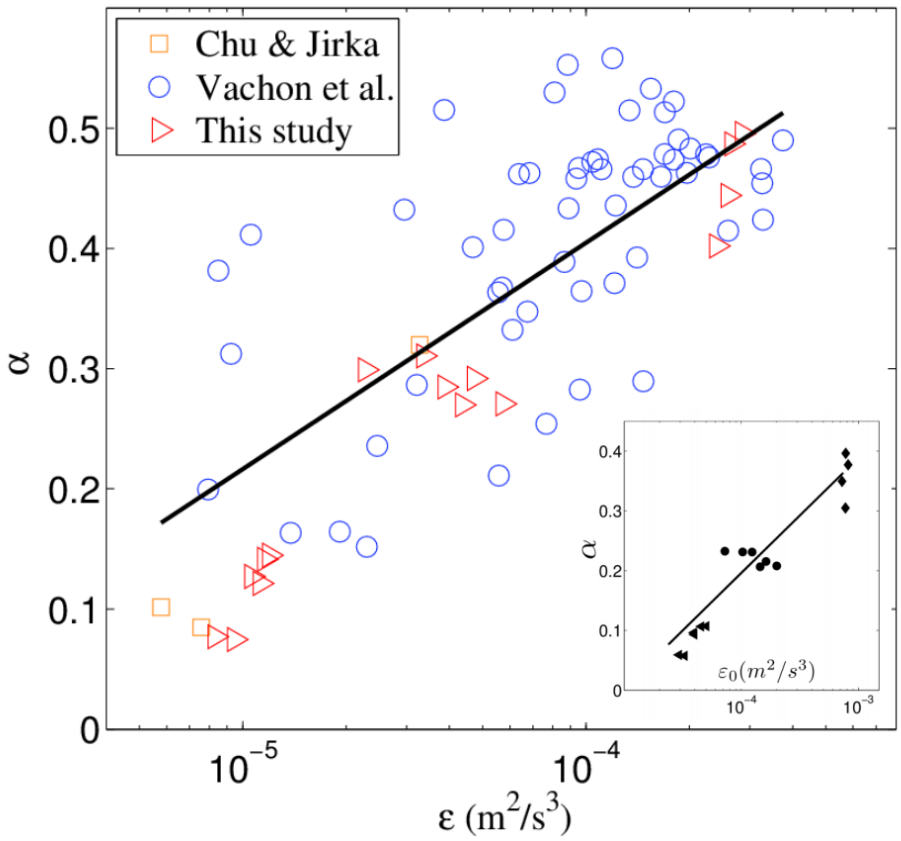

Figure 5-3: Log-linear relation between the coefficient α and the near surface turbulent dissipation rate. The solid line represents the log-linear relation $\alpha = 0.188 \log \varepsilon + 1.158$. The small panel represents log-linear relation between the coefficient α and the turbulent dissipation rate at the water surface

In addition, I also plot the relationship between the model coefficient and dissipation rate for the field observations of *Zappa et al.* [2007], shown in figure 5-4. Data in *Zappa et al.* [2007] can be further divided into four groups with different environments, including a micro-tidal estuary of the Parker River (Denoted as Parker), a tidal freshwater Hudson River (Hudson), a modeled ocean of the Biosphere 2 with near-surface turbulence produced by raindrops (Biosphere) and a coastal ocean near Duck, NC, USA (Duck). All data from *Zappa et al.* [2007] showed a large scatter with no clear correlation. However, a closer inspection indicated that 11 out of 16 data points from

Duck still agreed well with the observed log linear relation, while the other 5 data points were about 4~5 times higher than those predicted by the relation. For Biosphere data, 4 out 5 seemed to fall onto the same log-linear trend, but one point with a lower dissipation rate (about 4×10^{-6} $m^2 s^{-3}$) was much higher. The log-linear relation failed to describe observations in Hudson and Parker. These observations suggested that a relation between the coefficient α and ε may depend on the mechanism of turbulence generation. Duck experiments were conducted in a similar environment to this study and that of *Vachon et al*. [2010], i.e., coastal ocean/lake with near-surface turbulence primarily controlled by wind shear and waves, hence showed the similar trend. Hudson and Parker data were obtained in a river/estuary environment with near-surface turbulence affected by tidal current and wind. Turbulence was generated by rainfall in Biosphere experiments and the available data may not be adequate for us to draw a conclusion. Due to large uncertainty of dissipation rate measurement and applicability of the SEM in extreme environments, such as high surfactant aquatic system (e.g., rivers), that field data was not used for analyzing the relation between the coefficient and the dissipation rate.

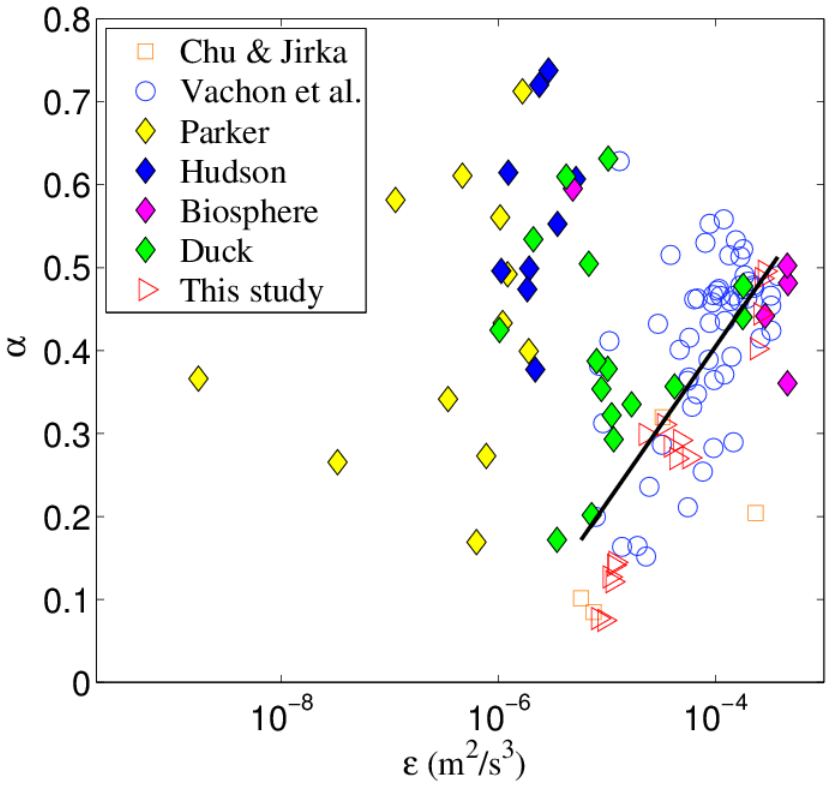

Figure 5-4: Log-linear relation between the coefficient α and the measured turbulent dissipation rate. The solid is the same as in figure 5-3.

I applied the empirical equation $\alpha(\varepsilon) = 0.188 \log \varepsilon + 1.158$ to the SEM and re-calculate transfer velocities, which are compared with measured transfer velocities in figure 5-5 (b), It is clearly shown that the dissipation rate dependent $\alpha(\varepsilon)$ provides a better estimation than a constant α (figure 5-5(a)), improving R^2 from 0.75 to 0.80. The improvement is more significant for a lower turbulence level, i.e., if I limit the analysis to data with $\varepsilon < 9 \times 10^{-5}$ m^2/s^3 (or equivalently transfer velocity $k_{600} < 18$ cm/hr), R^2 would be improved from 0.27 to 0.60.

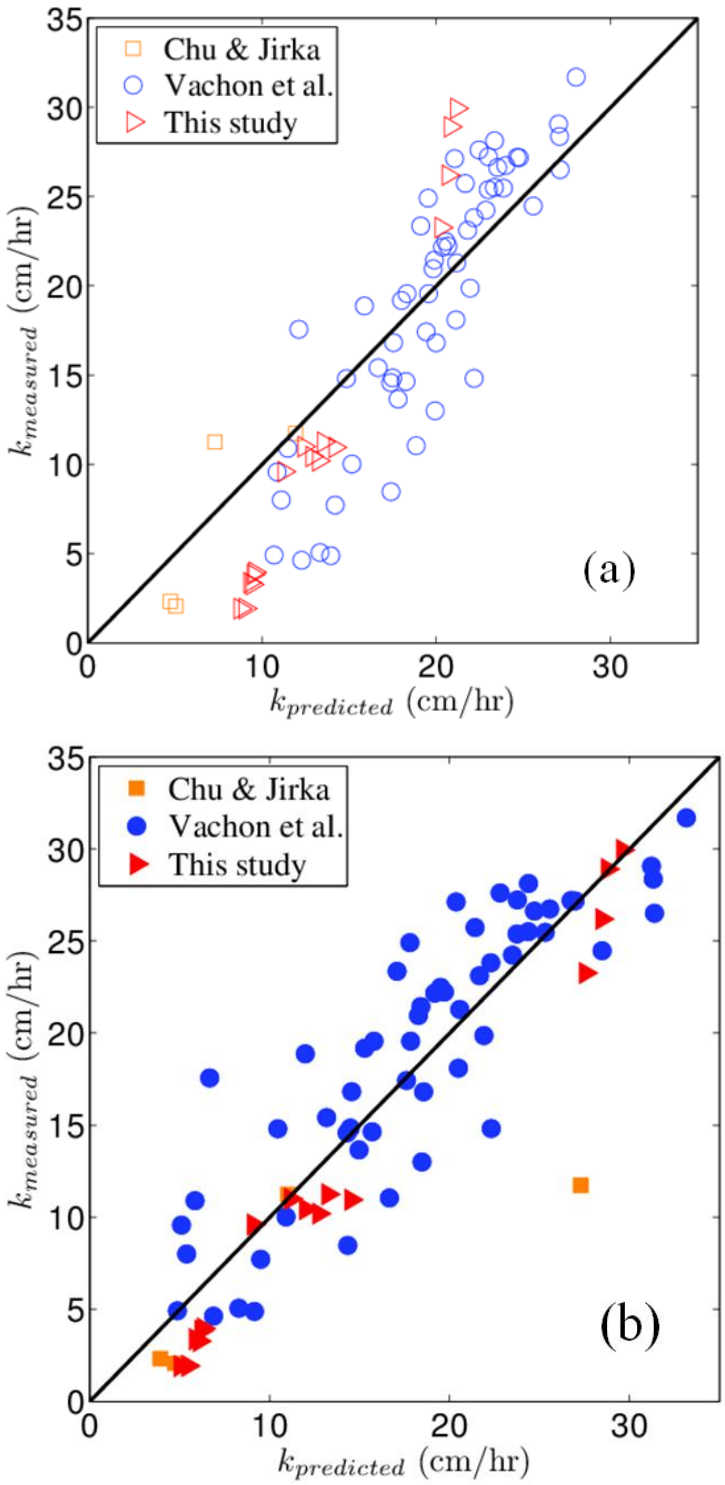

Figure 5-5: comparison between measured transfer velocity and the SEM prediction (a) coefficient is constant (b) coefficient depends on dissipation rate, following regression equation: $\alpha(\varepsilon) = 0.188 \log \varepsilon + 1.158$

Analysis clearly shows that the coefficient in the SEM is not a constant, and it is related to the turbulence level in aquatic system. It is noted that the relationship between coefficient and dissipation rate varies with the location where the dissipation rate was measured. As shown in field studies on near surface turbulence structure [*Wang et al.*, 2013] and literatures [*M H K Siddiqui and Loewen*, 2007; *Teixeira*, 2012; *Terray et al.*, 1996], strong gradient exists for the vertical profile of the near surface dissipation rate, and the scaling with z is not universal, which is likely dependent on the mechanism of turbulence generation on the surface. In this study, turbulent dissipation rate close to the interface (e.g. z~ 0 cm) is more likely correlated to the wind shear but would be significantly affected by surface waves away from the interface but still within the wave affected surface layer (e.g. z ~ 10 cm). Consequently, the accuracy of the SEM application might be significantly affected by appropriate location where the dissipation rate would be measured.

5.3.2 Surface divergence model (SDM)

Several laboratory experiments showed evidence of the surface divergence model (SDM) on estimating interfacial gas transfer velocity for both wind shear turbulence and mechanical generated turbulence [*Asher et al.*, 2012; *Turney et al.*, 2005]. The SDM is expressed as equation (3) in Chapter 1. In this study, I also provide the verification of the SDM from *in situ* measurement of the surface divergence. *Asher et al.* [2012] argued that not every divergence and convergence event extends the surface layer to the air-water

interface and contributes to the interfacial gas exchange. They compared the renewal time scales of water surface temperature and PH value within 0.3 millimeters of the water surface and found that the divergence and convergence events do not completely renew the interface. Following the concept of the depth of divergence (defined as the location of zero-velocity at the divergence direction because of surface "blocking" effect), the divergence term should be measured immediately below the air-water interface (within the thickness of the divergence depth).

The root mean square of surface divergence term was evaluated at the water surface following equation (5) in Chapter 1. Following the similar procedure shown in section 5.4.1, the time series of predicted transfer velocity from the SDM are plotted (figure 5-6) and compared with that of the FC measurements for the same bursts shown in figure 5-2.

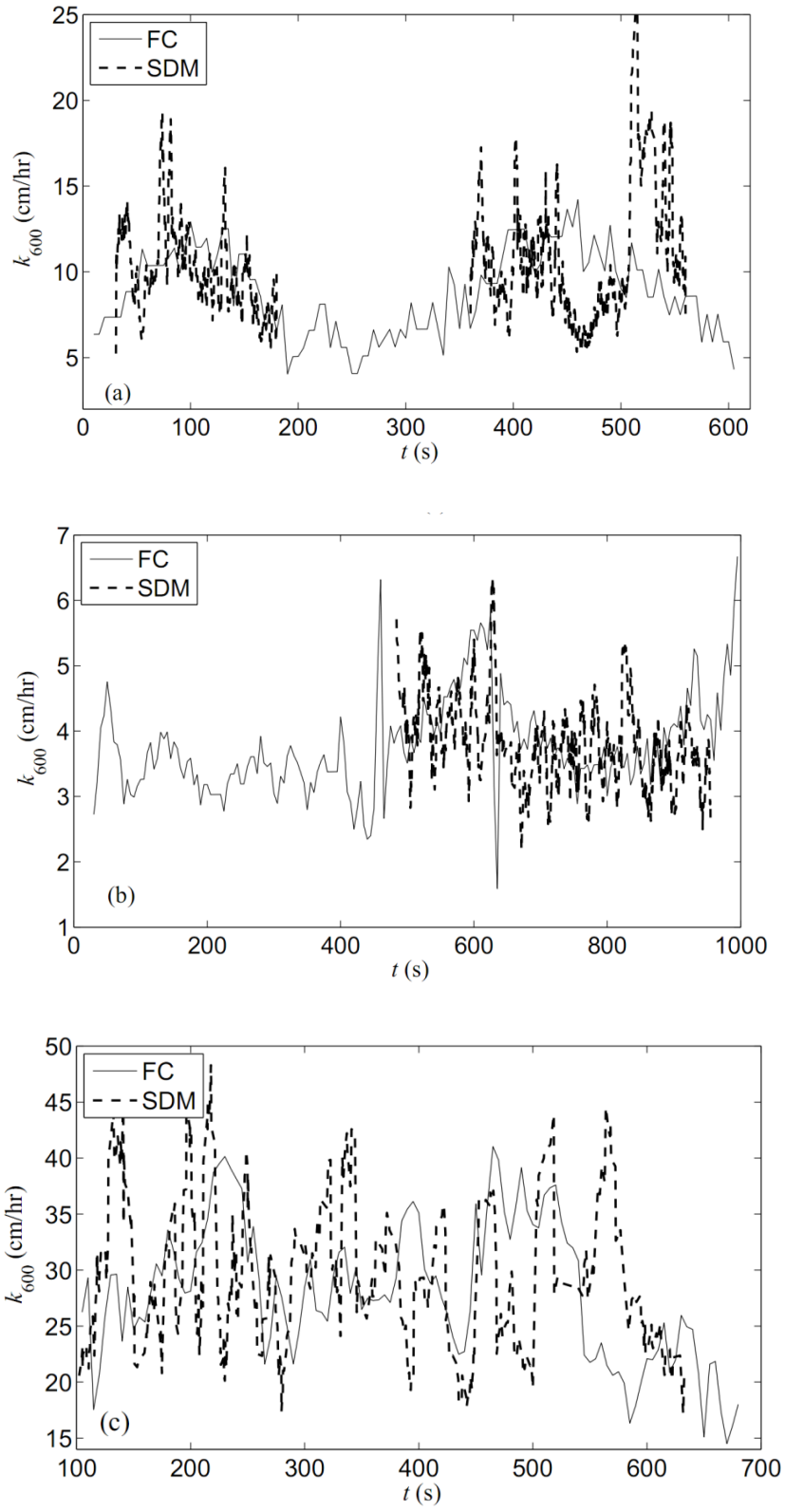

Figure 5-6: Direct comparison of time series of measured transfer velocity with the SDM prediction, (a) T1C (b) T2C (c) W2C

In general, the predicted *k* match well with the FC measured value in the acceptable range of variations. Compare to the SEM prediction in figure 5-2, the results of the SDM show noisier signals. Surprisingly, from the similarity of overall trends of the SEM and SDM signals in figure 5-2 and 5-6, they should be correlated with each other. This might be a side evidence of local isotropic turbulence near the water surface, since dissipation rates receive contributes from two velocity fluctuation gradient components at both horizontal and vertical directions, while the surface divergence term is only subjected to the vertical velocity fluctuation gradient in the vertical direction (i.e., "upwelling" and "downdraft" motions) [*Banerjee et al.*, 2004].

Although figure 5-2 and figure 5-6 look similar, the model coefficient for the SDM is different from that of the SEM. In figure 5-6, the coefficient from the best fit of regression is 0.3806, 0.2101 and 0.3375 for cases T1C, T2C and W2C. Section 5.4.1 shows that the model coefficient in the SEM is a function of dissipation rate. However, the coefficient in the SDM is more likely a constant.

The results presented above show that both the SEM and the SDM provide reasonable predictions on interfacial gas transfer velocity. The similarity of time series plotting shows potential correlation between two models. In order to further investigate the relationship between two models, $Sc^{1/2}(\nu\varepsilon_0)^{1/4}$ is plotted against $Sc^{1/2}(\nu\bar{\gamma}_{RMS})^{1/2}$ for all cases (see figure 5-7).

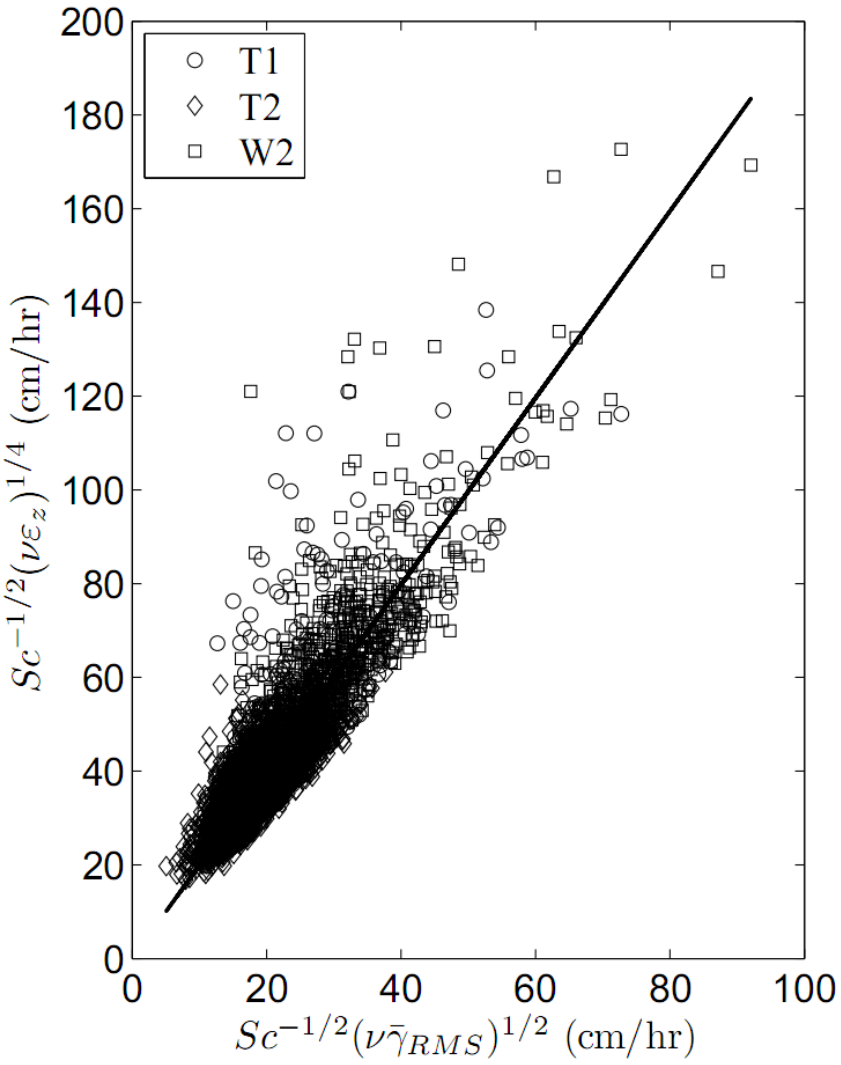

Figure 5-7: Relationship between the SEM and the SDM for all cases. The solid line represents linear regression of best fit with intercept = 0.

Strong correlation is observed (R^2 = 0.743) between the two models at the air-water interface. The slope of linear regression line represented in figure 5-7 is 1.99. If the concept of surface divergence was adapted to the whole water column (i.e., "upwelling" motions), the averaged profile of $Sc^{1/2}(\nu\bar{\gamma}_{RMS})^{1/2}$ at different depth is plotted with that of $Sc^{1/2}(\nu\varepsilon_z)^{1/4}$ in figure 5-8.

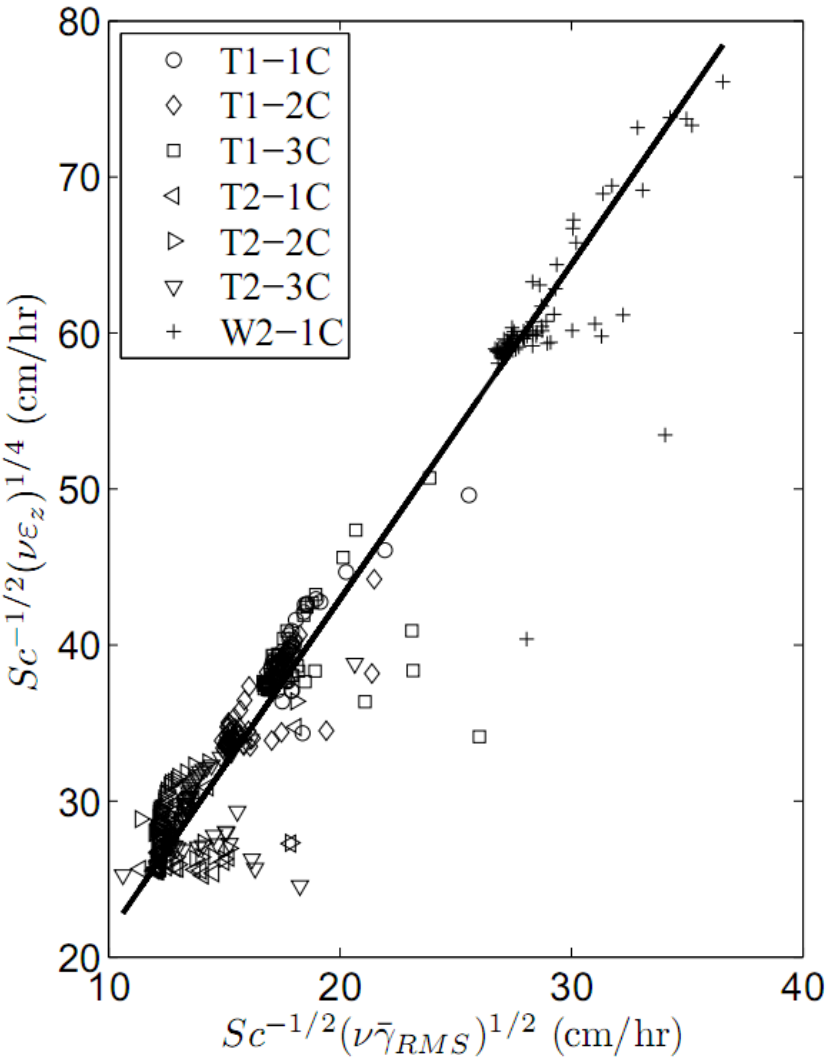

Figure 5-8: Relationship between vertical profiles of $Sc^{1/2}(\nu\varepsilon_z)^{1/4}$ and $Sc^{1/2}(\nu\bar{\gamma}_{RMS})^{1/2}$ for all cases. The solid line represents linear regression of best fit with intercept = 0.

The linear correlation is also observed with higher coefficient of determination (R^2 = 0.94). The slope of solid line in the profile plotting is 2.15, indicating the relationship between the ε_D with $\overline{\left(\frac{\partial w'}{\partial z}\right)^2}$. In isotropic turbulence,

$$\varepsilon_{iso} = 15\nu\overline{\left(\frac{\partial w'}{\partial z}\right)^2} \tag{4}$$

The ratio of $\varepsilon_{iso}^{1/4}$ and $\nu^{1/4}\bar{\gamma}$ is $15^{1/4}$ (approximately 1.97), which is very close to the value of the fitted slopes in figure 5-7 and figure 5-8. This result demonstrates an isotropic turbulence signature at near surface region. Chapter 3 shows 1-D velocity spectrum for E_{11} and $3/4E_{33}$ are close to the same energy level. Although the evidence of isotropic turbulence should not be able to be concluded, from the above analysis I suggest that isotropic turbulence assumption is suitable for estimating near surface dissipation rate (e.g. ADV measurements).

5.3.3 Chamber effects on estimation of interfacial gas transfer velocity

Floating chamber is a widely used device to measure interfacial gas flux and transfer velocity in a variety of natural aquatic environments [*Alin et al.*, 2011; *Tokoro et al.*, 2007], although the accuracy of this technique is still questionable [*Eugster et al.*, 2003; *Kremer et al.*, 2003]. For the purpose of verifying the near surface turbulence modeling, the FC method is appropriate for this study since both transfer velocity and near surface measurements are highly local and correlated (inside of the chamber). Any artificial effects of the FC on natural aquatic system were captured by *in situ* FPIV measurements. However, due to discrepancy of the FC measurement and other techniques (e.g., eddy correlation method, tracer release technique), I further investigate the artificial effects of the FC on the statistics of near surface turbulence, which is directly related to the interfacial gas exchange.

As described in the experiment arrangement, two configurations were carried out for each case. All "uncovered" cases were performed after "covered" measurements. Several bursts were also taken for each case (see Table 1). Ideally, simultaneous measurements of the statistics of turbulence inside and outside of the FC should be done to make direct comparison. However, due to the limitation of the experiment arrangement, the measurements of two configurations were conducted consecutively.

The vertical profiles of TKE dissipation rate for all cases are plotted in log-log scale (figure 5-9). The solid line represent -1 power law of decaying rate of dissipation rate ($\varepsilon \sim z^{-1}$). Averaged dissipation rate profiles for all runs are plotted in figure 5-10.

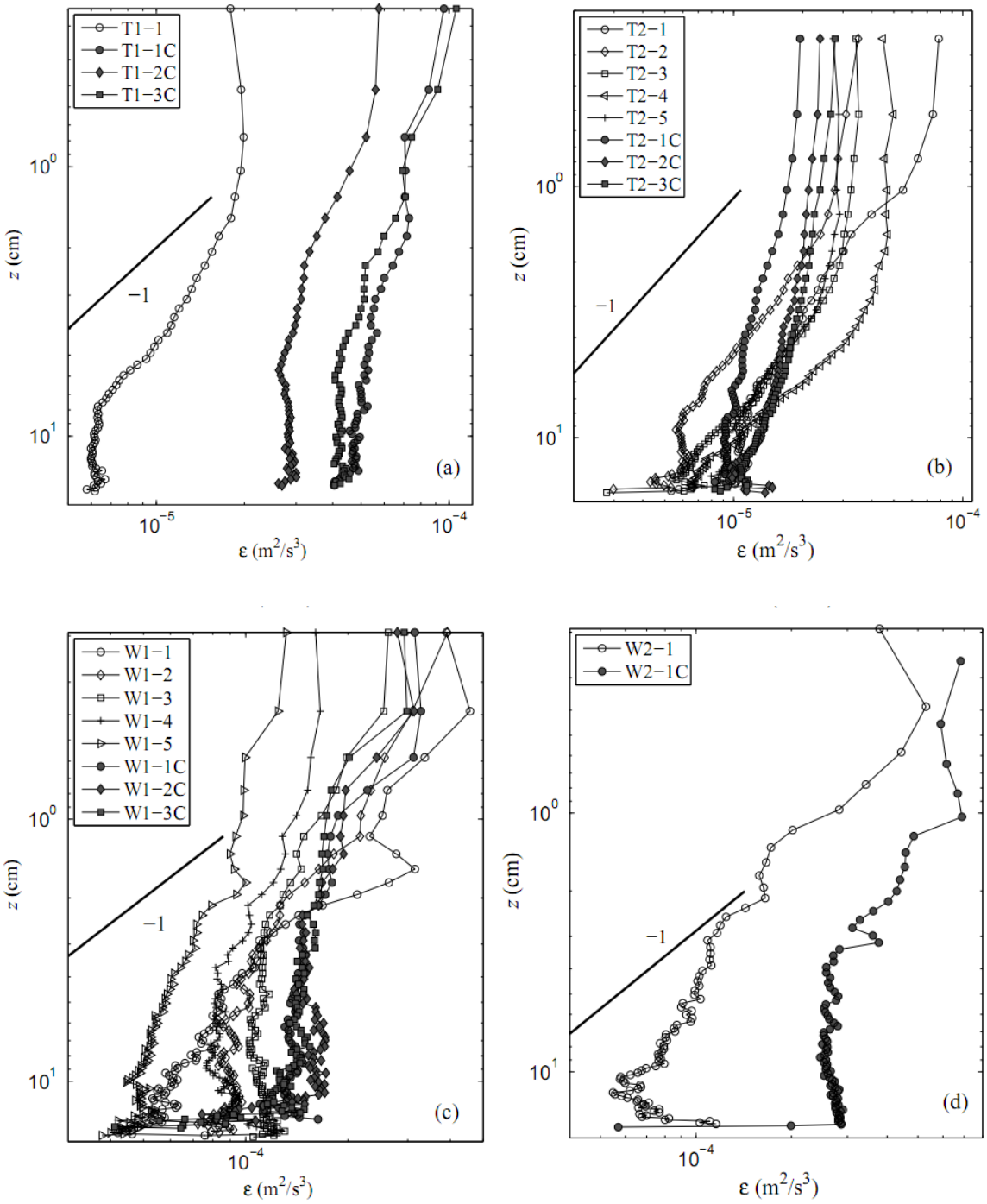

Figure 5-9: Comparison of vertical dissipation rate profiles inside and outside of the FC. The solid lines represent -1 power law decaying rate of $\varepsilon(z)$. (a) T1; (b) T2; (c) W1; (d) W2

Generally, all profiles show high ε close to the water surface with certain decaying rate away from the interface. The decaying rates are mostly smaller than wall turbulence behavior (i.e., -1 decaying rate in figure). As can be seen in figure 5-9, two major effects of the FC on near surface turbulence were observed in this study: (1) The chamber effect on enhancing near surface turbulence is apparent for all cases. The enhanced TKE dissipation rate (i.e., measured inside of the FC) is approximately within one order of magnitude larger than that in the natural system (i.e., measured outside of the FC) for all cases. (2) The FC generating artificial turbulence make the vertical profile of dissipation rate more uniform than that in the natural system (i.e., slower decaying rate of dissipation rate away from the air-water interface).

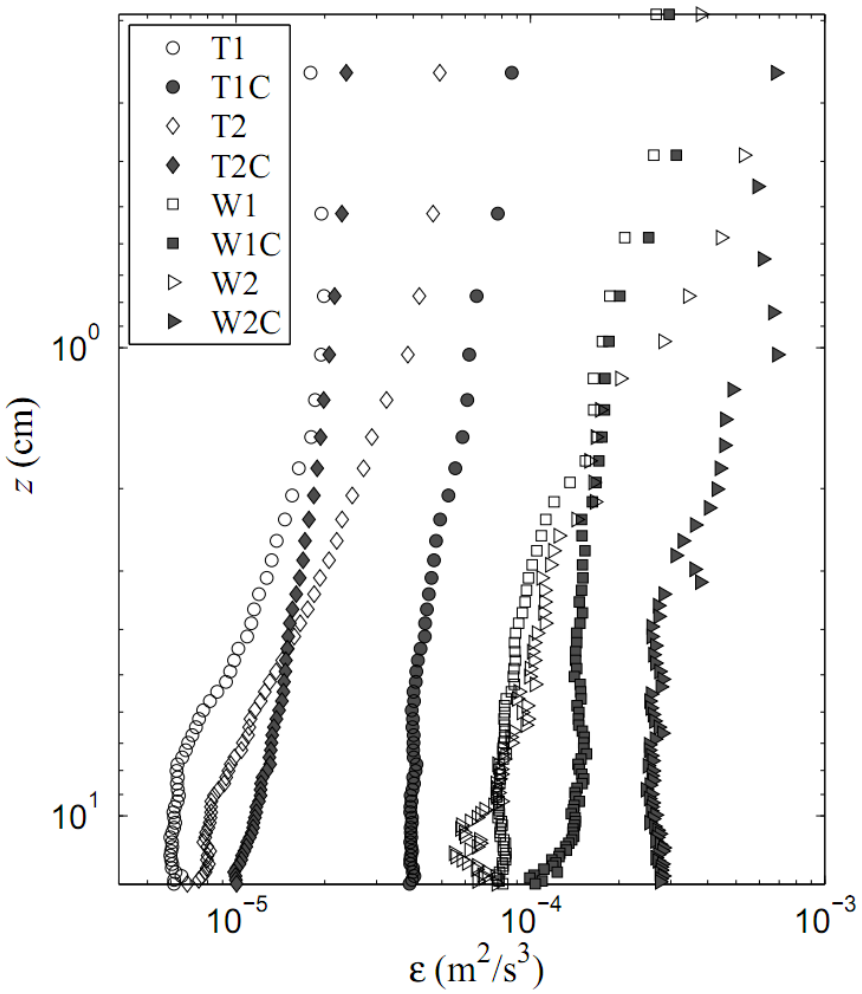

Figure 5-10: Averaged vertical profiles of dissipation rate based on "covered" or "uncovered" configurations.

Kremer et al. [2003] suggested that the FC method should be employed in case of low to moderate winds (i.e., < 8 ~ 10 m/s in their experiments) with limited fetch. In this study, T1 was carried out in low wind environment without significant surface waves. In this case, 3 ~ 6 times enhanced surface dissipation rate (ε_0) was observed for "covered" condition with respect to "uncovered" condition. Approximately 5 ~ 8 times difference of $\varepsilon(z)$ between two configurations was shown at z = 10 *cm* (see figure 5-9(a)). *Kremer et al.*

[2003] argued that the ideal FC deployment should drift with current of surface layer, since that could significant reduce the disruption to the aqueous boundary layer. In this study, the system was tethered on the vessel due to experiment limitation. Therefore, the movement of vessel would also generate disturbance on the surface layer that could be advected to the sampling area. A relatively small difference would be expected if the whole system is free drifting.

For case T2, a significant difference in the near surface turbulent dissipation rate was observed compared with that of T1, although no significant surface waves were present. Totally eight PIV bursts were carried out in case T2 and three bursts were measured for the FC covered area. For "uncovered" condition, $\varepsilon(z)$ decays rapidly away from the water surface almost following -1 decaying rate, although no significant decay shows at the topmost layer (i.e., $z < 1$ cm) (see figure 5-9(b)). The near surface turbulence behaves similar to the bottom shear wall turbulence, with the surface shear dominated by wind. At the topmost layer, the dissipation rate is almost constant because of the existence of surface capillary waves. For "covered" conditions, the dissipation rate decaying rate is much smaller than that in the real natural system (i.e., "uncovered" measurements). 2 ~ 3 times difference in the upper 10 cm layer was observed compared with that of 3 ~ 10 times difference for "covered" configurations. During this run, the wind changed rapidly such that the statistics of near surface turbulence were largely controlled by the environmental forces in a very short time scale (several minutes or less). It should be noted that the wind data for this run might not be accurate enough for direct comparison. But certainly, the wind speed for "covered" configurations was far smaller than that of "uncovered" configurations during the measurements. As can be seen in

figure 5-9(b), $\varepsilon(z)$ at z = 10 cm for "covered" configurations are comparable or even larger than that for "uncovered" configurations, which demonstrates direct evidence of enhancement effect or the FC on statistics of near surface turbulence.

For case W1 and W2, the near surface layer was covered by gravity waves with approximately one foot wave height, and moderate wind shear (see Table 1). The surface dissipation rate is on the order of 10^{-4} m^2/s^3, the enhancement due to the chamber effect is less than that for all T cases. Under waves-covered field with moderate to large wind speed, the near surface turbulence is generally strong at the surface layer (see Chapter 4). Several turbulence sources play different roles in this complex environment. Wave induced turbulence demonstrate low decaying effect from the water surface to the great deep (shown as smaller slope of dissipation rate vertical profile in figure 5-9 c and d). Furthermore, strong vortex structures would be generated by micro-scale wave breaking and hence enhanced gas transfer at the air-water interface. (It should be noted, in this study, I am not able to quantify the effect of micro-scale wave breaking). As the results, the disturbance of the FC on the topmost layer is not as significant as that for T cases. However, away from the air-water interface (e.g., z = 10 cm), the enhancement effect is clear seen in figure 5-9 c and d.

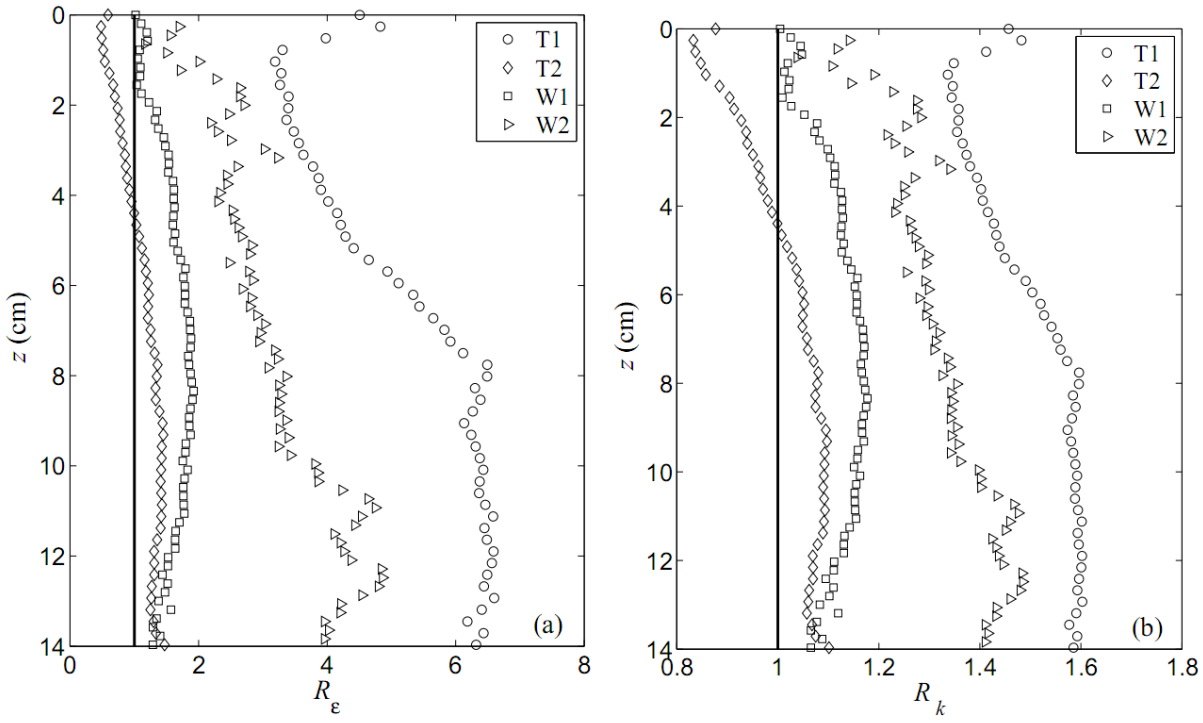

Figure 5-11: Plot of the enhancement ratio R against the depth z, the solid lines represent $R = 1$. (a) enhancement ratio of dissipation rate R_ε; (b) enhancement ratio of transfer velocity R_k.

In order to quantify the enhancement of the FC on transfer velocity, the enhancement ratio of dissipation rate and gas transfer velocity are plotted in figure 5-11, where the enhancement ratio R is defined as: $R_\varepsilon = \varepsilon(z)_{\text{covered}} / \varepsilon(z)_{\text{uncovered}}$ and $R_k = k(z)_{\text{covered}} / k(z)_{\text{uncovered}} = (\varepsilon(z)_{\text{covered}} / \varepsilon(z)_{\text{uncovered}})^{1/4}$ for dissipation rate and transfer velocity, respectively. The enhancement effect is clearly seen in figure 5-11. It is noting that only T2 shows underestimate of dissipation rate under "covered" configuration. The reason is due to the relatively calm environment force during the "covered" measurements, while wind gusts were quite strong during "uncovered" measurements.

Vachon et al. [2010] argued that the FC disturbance effect on near surface turbulence is related to the turbulent level, represented by measured dissipation rate in their study. The results are consistent with their observation showing relatively strong enhancement at low turbulence levels (e.g., case T1, $\varepsilon \sim 1\times10^{-5}$ m^2/s^3). However, the enhancement effect is not uniformly distributed at the surface layer. As can be seen in figure 5-11, the weaker enhancement effects are present at the water surface due to two reasons: (1) the natural turbulence is higher at the air-water interface representing larger denominator in the definition of enhancement ratio; (2) the most of artificial turbulence generated by the FC are due to the edge of chamber and wall effect of chamber. Since the FPIV measurements were located at the center of chamber, the artificial turbulence at the sampling area are most likely advected from the walls of the chamber. Therefore, the artificial turbulence close to the air-water interface should be weaker than that of the bottom area in this study. Consequently, the disturbance effect might be considerably overstated in the direct comparison of dissipation rate where it is measured at the short distance away from the interface (e.g., $z \sim 10$ cm in *Vachon et al.* [2010]). From the above analysis, this study suggests that the FC method is an acceptable technique for estimating interfacial gas exchange flux and transfer velocity, although overestimate is problematic. Importantly, the deployment of the FC requires careful attention because the disturbance effect could be magnified by any unnatural perturbations by movement of the nearby vessel from where the FC was deployed.

5.3.4 Comments on wind speed parameterization

Wind speed has been recognized as the primary proxy to model the interfacial gas exchange over a range of natural environments, especially for oceans and lakes with large surface area [*R Wanninkhof*, 1992]. Although the combination effect need to be considered for other turbulence sources in rivers (e.g., the stream current and water depth), wind speed is still the dominant driving factor of gas transfer across the air-water interface [*Ho et al.*, 2011a].

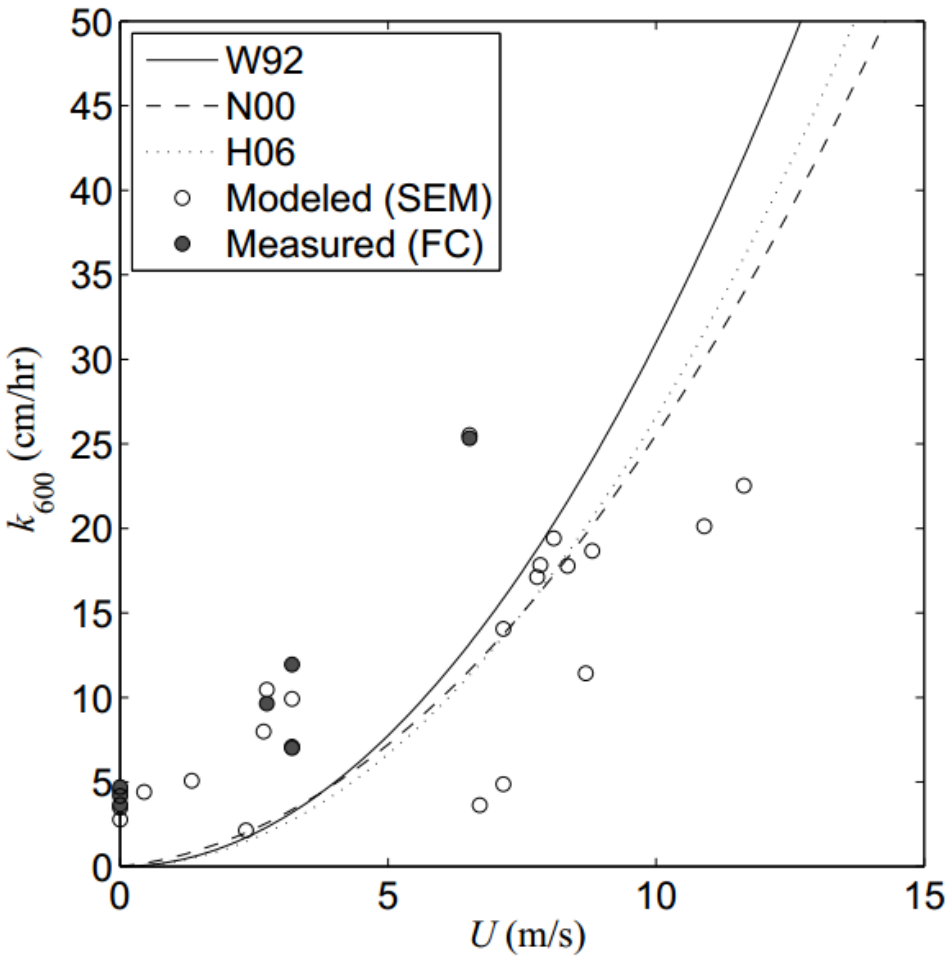

Figure 5-12: Plot of interfacial transfer velocity k_{600} against wind speed, the cases with "uncovered" configurations are also plotted based on the SEM prediction.

In this study, I also plot the relation of measured or modeled transfer velocity of CO_2 in fresh water system at 20 ℃ against recorded wind speed. Three widely used wind speed models are employed for comparison in the figure 5-12. W92 represents the short term or steady wind speed condition estimation, since the measurements in this study is much shorter than that of tracer release experiments in the ocean [*R Wanninkhof,* 1992]. N00 represents the model based on the coastal area measurement in fetch limited environments [*Nightingale et al.,* 2000]. H06 relationship is obtained from SOLAS Air-Sea Gas Exchange (SAGE) experiment in Southern Ocean [*Ho et al.*, 2006a].

In general, good correlation between interfacial gas exchange rate and wind speed was observed for current data (both FC measured and SEM modeled). As can be seen, for cases with wind speed smaller than 5 m/s, estimation of gas transfer velocity from local measurement method is higher than that from wind speed estimation. For most cases with higher wind speed, the SEM predicted transfer velocity is smaller than that from wind speed model, while the FC method is difficult to be achieved.

Chapter 6

Concluding Remarks and Recommendation for Future Works

6.1 Concluding remarks

The aim of this dissertation is to conduct *in situ* experimental studies on the interfacial gas exchange and its relationship with the aqueous side turbulence immediately adjacent to the air-water interface. An advanced *in situ* free floating PIV system was developed in this work. The use of scanning mirror technique is a successful approach to bring the standard laboratory instrumentation to real and natural environmental systems. With the FPIV, the turbulence structures, including the rate of strain, turbulent dissipation rate and other statistical parameters, were investigated immediately below the undulating water surface, in the presence of surface gravity waves.

Most of the work that contributed to this dissertation centered at aquatic system of Lake Michigan. Lake Michigan is an excellent environment to study the interfacial gas exchange under the complex wind-wave forcing conditions. Lake Michigan is also an excellent research site for field PIV deployment, since the natural tracers provide bright, high quality images for PIV analysis. The experimental results at wind wave surface layer of Lake Michigan validated the methodology. These results also reveal a significant wave effect on near surface turbulence production term, which agree with laboratory results in the literature.

With the application of field PIV technique, a series of experiments were conducted at the topmost layer of Lake Michigan, focusing on measurement of the turbulent structure immediately below the air-water interface with surface gravity waves. Two apparently distinguished sea states were studied. Turbulence under surface waves at the wind-wave initiation period was measured inside of Milwaukee harbor. The results show that the turbulence structure is most likely similar to wall bounded turbulence. Dissipation rates decay away from the air-water interface quickly following near $\varepsilon \sim z^{-1}$. The value of turbulent dissipation rate is smaller than that predicted with the Law of Wall.

Due to growth of wind waves, the effects of wave age should be investigated as parameterizing the statistics of near surface turbulence, particularly close to the air-water interface. In this dissertation, I compared the turbulence dissipation rate profiles for the cases with different wind speed but very short fetch, the cases with similar wave height but different sea state. The wave age was found significantly affecting the TKE dissipation rate near the water surface. A universal relation was found for all cases accounting for the factors contributed by wind shear velocity, wave height and wave age.

To this end, the result can be utilized in estimation of surface turbulent dissipation under non-breaking wave condition, which would update the current transfer velocity model.

At last, two hydrodynamic models for estimating interfacial gas transfer velocity were compared with direct measurement within an incubated surface area by a floating chamber. Both small scale eddy model and surface divergence model give reliable estimation of gas transfer velocity. Although promising, it should be noted that the model coefficient in the SEM may not be a constant. A strong correlation was found between the coefficient and measured dissipation rate. I suggest the controlling mechanism of interfacial gas exchange is the result of combined effects of turbulent eddies with different scales. The smallest scale turbulent bursts might not fully explain the process of interfacial gas flux. Two dimensional PIV measurements also enable us to evaluate the effect of floating chamber on quantifying gas transfer velocities. The artificial effect of the FC would be very different with various environmental conditions. However, the FC generally overestimates the gas transfer velocity due to the disturbance on aquatic system.

6.2 Recommendation for future works

In light of the apparent relation among surface gravity waves, wind shear and turbulence close to the water surface, comprehensive studies are need to investigate how energy transfer is made amongst the all three physical parameters. Herein, I present a series of experimental studies of statistics of turbulence immediately below the air-water interface, aiming to give a practical parameterization of near surface turbulence using environmental factors.

Therefore, upon the finding of this dissertation, I suggest the future work should focus on quantifying the wave-current-turbulence interaction and further studying on appropriate scales of near surface turbulence which can be utilized to characterize gas transfer across the interface.

More specifically, a well designed laboratory experiment can be used to study the unsolved questions in the future. Both wind wave and mechanic wave are worth to the interaction effect with free surface turbulence and background current. One can focus on studying the small-scale turbulence structure immediately below the air-water interface and scaling rule at vertical direction. Obviously, the completely understanding the interaction among current, waves and turbulence needs triple decomposition of measured velocity data. However, there might be no way to completely make this decomposition. In this case, one might investigate wave impact on background turbulence from a series known parameters. For example, if applying mechanic waves on background turbulence generated by grid stirred device, which has been extensively studied and described by a well established turbulence generation mechanism. Then, one can investigate wave impact on background turbulence. In such a way, changes can be made on wave frequency, wave height, wave length, steepness, etc to investigate if there exists a peak frequency where interaction between surface wave and turbulence is maximum.

I also suggest study the evolution of interaction between surface waves and near surface turbulence. Moreover, one of most important topic in the future is to quantify the energy path among the current, waves and turbulence. For momentum and energy budget, each term in mean kinetic energy (MKE) equation, wave kinetic energy (WKE) equation and turbulent kinetic energy equation (TKE) equation would be analyzed carefully for

different wave generation mechanism. This is important to compare the shear stress production term with other interaction terms for wind wave cases and mechanic wave cases.

From the biogeochemical point of view, it is ideal to estimate interfacial gas flux from environmental data, which is easy to implement in the global models. Surface renewal model suggest to use a time scale to quantify the gas transfer velocity, which results hydrodynamic models with different parameterization based on the size of dominant eddies. In this study, both large and small eddies are found to be important. However, the relationship between gas transfer velocity with turbulent characteristics is still semi-empirical. The finding suggested a single scaling might not be enough to describe the gas transfer process at the air-water interface. Future study should focus on investigating the spectrum of near surface hydrodynamics that can be linked with gas flux parameterization.

Finally, the interfacial gas exchange is related to complex environmental forcing, such as wave breaking with air bubble entrainment, precipitation, micro-scale wave breaking, etc. A universal parameterization may or may not exist to describe the gas transfer velocity. I am hoping to get clear pictures for individual dominant case, which can be used in global models.

References:

Adrian, R. J., K. T. Christensen, and Z. C. Liu (2000), Analysis and interpretation of instantaneous turbulent velocity fields, *Exp Fluids*, *29*(3), 275-290.

Agrawal, Y. C., E. A. Terray, M. A. Donelan, P. A. Hwang, A. J. Williams, W. M. Drennan, K. K. Kahma, and S. A. Kitaigorodskii (1992), Enhanced Dissipation of Kinetic-Energy beneath Surface-Waves, *Nature*, *359*(6392), 219-220.

Alin, S. R., M. D. F. L. Rasera, C. I. Salimon, J. E. Richey, G. W. Holtgrieve, A. V. Krusche, and A. Snidvongs (2011), Physical controls on carbon dioxide transfer velocity and flux in low-gradient river systems and implications for regional carbon budgets, *J Geophys Res-Biogeo*, *116*.

Anderson, R. J. (1993), A Study of Wind Stress and Heat-Flux over the Open-Ocean by the Inertial-Dissipation Method, *J Phys Oceanogr*, *23*(10), 2153-2161.

Anis, A., and J. N. Moum (1995), Surface Wave-Turbulence Interactions - Scaling Epsilon(Z) near the Sea-Surface, *J Phys Oceanogr*, *25*(9), 2025-2045.

Ardhuin, F., and A. D. Jenkins (2006), On the interaction of surface waves and upper ocean turbulence, *J Phys Oceanogr*, *36*(3), 551-557.

Asher, W. E. (1997), The sea-surface microlayer and its effects on global air-sea gas transfer, in *The sea surface microlayer and global change*, edited by P. S. Liss and R. A. Duce, pp. 251-286, Cambridge University Press.

Asher, W. E., and J. F. Pankow (1986), The interaction of mechanically generated turbulence and interfacial films with a liquid phase controlled gas/liquid transport process, *Tellus B*, *38*, 305-318.

Asher, W. E., A. T. Jessup, and M. A. Atmane (2004), Oceanic application of the active controlled flux technique for measuring air-sea transfer velocities of heat and gases, *J Geophys Res-Oceans*, *109*(C8).

Asher, W. E., L. M. Karle, B. J. Higgins, P. J. Farley, E. C. Monahan, and I. S. Leifer (1996), The influence of bubble plumes on air-seawater gas transfer velocities, *J Geophys Res-Oceans*, *101*(C5), 12027-12041.

Asher, W. E., H. Liang, C. J. Zappa, M. R. Loewen, M. A. Mukto, T. M. Litchendorf, and A. T. Jessup (2012), Statistics of surface divergence and their relation to air-water gas transfer velocity, *J Geophys Res-Oceans*, *117*(C05035).

Atmane, M. A., W. E. Asher, and A. T. Jessup (2004), On the use of the active infrared technique to infer heat and gas transfer velocities at the air-water free surface, *J Geophys Res-Oceans*, *109*(C8).

Babanin, A. V., and B. K. Haus (2009), On the Existence of Water Turbulence Induced by Nonbreaking Surface Waves, *J Phys Oceanogr*, *39*(10), 2675-2679.

Banerjee, S. (1990), Turbulence structure and transport mechanisms at interfaces, in *Proc. 9th International Heat Transfer Conference*, edited, pp. 395-418.

Banerjee, S., E. Rhodes, and D. S. Scott (1968), Mass transfer through falling wavy liquid films in turbulent flow, *Industrial and Engineering Chemicals Fundamentals*, *7*, 22-27.

Banerjee, S., D. Lakehal, and M. Fulgosi (2004), Surface divergence models for scalar exchange between turbulent streams, *Int J Multiphas Flow*, *30*(7-8), 963-977.

Berg, P., H. Roy, F. Janssen, V. Meyer, B. B. Jorgensen, M. Huettel, and D. de Beer (2003), Oxygen uptake by aquatic sediments measured with a novel non-invasive eddy-correlation technique, *Mar Ecol-Prog Ser*, *261*, 75-83.

Berg, P., R. N. Glud, A. Hume, H. Stahl, K. Oguri, V. Meyer, and H. Kitazato (2009), Eddy correlation measurements of oxygen uptake in deep ocean sediments, *Limnol Oceanogr-Meth*, *7*, 576-584.

Bluteau, C. E., N. L. Jones, and G. N. Ivey (2011), Estimating turbulent kinetic energy dissipation using the inertial subrange method in environmental flows, *Limnol Oceanogr-Meth*, *9*, 302-321.

Bock, E. J., T. Hara, N. M. Frew, and W. R. McGillis (1999), Relationship between air-sea gas transfer and short wind waves, *J Geophys Res-Oceans*, *104*(C11), 25821-25831.

Borges, A. V., J. P. Vanderborght, L. S. Schiettecatte, F. Gazeau, S. Ferron-Smith, B. Delille, and M. Frankignoulle (2004), Variability of the gas transfer velocity of CO2 in a macrotidal estuary (the Scheldt), *Estuaries*, *27*(4), 593-603.

Boutin, J., J. Etcheto, L. Merlivat, and Y. Rangama (2002), Influence of gas exchange coefficient parameterisation on seasonal and regional variability of CO(2) air-sea fluxes, *Geophys Res Lett*, *29*(8).

Broecker, H. C., J. Petermann, and W. Siems (1978), The influence of wind on CO_2 exchange in a wind wave tunnel, including the effects of monolayers, *J Mar Res*, *36*, 595-610.

Broecker, W. S., T. H. Peng, G. Östlund, and M. Stuiver (1985), The distribution of bomb radiocarbon in the ocean, *J Geophys Res-Oceans*, *99*, 6953-6970.

Burchard, H. (2001), Simulating the wave-enhanced layer under breaking surface waves with two-equation turbulence models, *J Phys Oceanogr*, *31*(11), 3133-3145.

Businger, J. A., and S. P. Oncley (1990), Flux Measurement with Conditional Sampling, *J Atmos Ocean Tech*, *7*(2), 349-352.

Charnock, H. (1955), Wind stress on a water surface, *Q J Roy Meteor Soc*, *81*, 639-640.

Cheung, T. K., and R. L. Street (1988), The Turbulent Layer in the Water at an Air Water Interface, *J Fluid Mech*, *194*, 133-151.

Chong, M. S., A. E. Perry, and B. J. Cantwell (1990), A General Classification of 3-Dimensional Flow-Fields, *Phys Fluids a-Fluid*, *2*(5), 765-777.

Chu, C. R., and G. H. Jirka (1992), Turbulent Gas Flux Measurements Below the Air-Water-Interface of a Grid-Stirred Tank, *Int J Heat Mass Tran*, *35*(8), 1957-1968.

Chu, C. R., and G. H. Jirka (2003), Wind and stream flow induced reaeration, *J Environ Eng-Asce*, *129*(12), 1129-1136.

Clark, J. F., P. Schlosser, R. Wanninkhof, H. J. Simpson, W. S. F. Schuster, and D. T. Ho (1995), Gas Transfer Velocities for Sf6 and He-3 in a Small Pond at Low Wind Speeds, *Geophys Res Lett*, *22*(2), 93-96.

Cowen, E. A., and S. G. Monismith (1997), A hybrid digital particle tracking velocimetry technique, *Exp Fluids*, *22*(3), 199-211.

Craig, P. D. (1996), Velocity profiles and surface roughness under breaking waves, *J Geophys Res-Oceans*, *101*(C1), 1265-1277.

Craig, P. D., and M. L. Banner (1994), Modeling Wave-Enhanced Turbulence in the Ocean Surface-Layer, *J Phys Oceanogr*, *24*(12), 2546-2559.

Csanady, G. T. (1990), The Role of Breaking Wavelets in Air-Sea Gas Transfer, *J Geophys Res-Oceans*, *95*(C1), 749-759.

D'Asaro, E., and C. McNeil (2007), Air-sea gas exchange at extreme wind speeds measured by autonomous oceanographic floats, *J Marine Syst*, *66*(1-4), 92-109.

Danckwerts, P. V. (1951), Sinificance of liquid-film coefficients in gas absorption, *Ind. Eng. Chem.*, *43*, 1460-1467.

de Jong, J., L. Cao, S. H. Woodward, J. P. L. C. Salazar, L. R. Collins, and H. Meng (2009), Dissipation rate estimation from PIV in zero-mean isotropic turbulence, *Exp Fluids*, *46*(3), 499-515.

Deacon, E. L. (1977), Gas transfer to and across an air-water interface, *Tellus*, *29*, 363-374.

Dhanak, M. R., and K. Holappa (1999), An autonomous ocean turbulence measurement platform, *J Atmos Ocean Tech*, *16*(11), 1506-1518.

Doron, P., L. Bertuccioli, J. Katz, and T. R. Osborn (2001), Turbulence characteristics and dissipation estimates in the coastal ocean bottom boundary layer from PIV data, *J Phys Oceanogr*, *31*(8), 2108-2134.

Drazen, D. A., and W. K. Melville (2009), Turbulence and mixing in unsteady breaking surface waves, *J Fluid Mech*, *628*, 85-119.

Edson, J. B., A. A. Hinton, K. E. Prada, J. E. Hare, and C. W. Fairall (1998), Direct covariance flux estimates from mobile platforms at sea, *J Atmos Ocean Tech*, *15*(2), 547-562.

Eugster, W., G. Kling, T. Jonas, J. P. McFadden, A. Wuest, S. MacIntyre, and F. S. Chapin (2003), CO2 exchange between air and water in an Arctic Alaskan and midlatitude Swiss lake: Importance of convective mixing, *J Geophys Res-Atmos*, *108*(D12).

Fairaill, C. W., J. E. Hare, J. B. Edson, and W. McGillis (2000), Parameterization and micrometeorological measurement of air-sea gas transfer, *Bound-Lay Meteorol*, *96*(1-2), 63-105.

Farmer, D. M., C. L. Mcneil, and B. D. Johnson (1993), Evidence for the Importance of Bubbles in Increasing Air Sea Gas Flux, *Nature*, *361*(6413), 620-623.

Fortescue, G. E., and J. R. A. Pearson (1967), On gas absorption into a turbulent liquid, *Chem Eng Sci*, *22*, 1163-1176.

Frankignoulle, M. (1988), Field measurements of air-sea CO_2 exchange, *Limnol Oceanogr*, *33*(3), 313-322.

Frew, N. M., J. C. Goldman, M. R. Dennett, and A. S. Johnson (1990), Impact of Phytoplankton-Generated Surfactants on Air-Sea Gas-Exchange, *J Geophys Res-Oceans*, *95*(C3), 3337-3352.

Frew, N. M., D. M. Glover, E. J. Bock, and S. J. McCue (2007), A new approach to estimation of global air-sea gas transfer velocity fields using dual-frequency altimeter backscatter, *J Geophys Res-Oceans*, *112*(C11).

Frew, N. M., et al. (2004), Air-sea gas transfer: Its dependence on wind stress, small-scale roughness, and surface films, *J Geophys Res-Oceans*, *109*(C8).

Frost, T., and R. C. Upstill-Goddard (2002), Meteorological controls of gas exchange at a small English lake, *Limnol Oceanogr*, *47*(4), 1165-1174.

Garbe, C. S., U. Schimpf, and B. Jähne (2004), A surface renewal model to analyze infrared image sequences of the ocean surface for the study of air-sea heat and gas exchange, *J Geophys Res-Oceans*, *109*(C8).

Geernaert, G. L., K. L. Davidson, S. E. Larsen, and T. Mikkelsen (1988), Wind Stress Measurements during the Tower Ocean Wave and Radar Dependence Experiment, *J Geophys Res-Oceans*, *93*(C11), 13913-13923.

Gemmrich, J. (2010), Strong Turbulence in the Wave Crest Region, *J Phys Oceanogr*, *40*(3), 583-595.

Gemmrich, J. R., and D. M. Farmer (2004), Near-surface turbulence in the presence of breaking waves, *J Phys Oceanogr*, *34*(5), 1067-1086.

Goldman, J. C., M. R. Dennett, and N. M. Frew (1988), Surfactant Effects on Air Sea Gas-Exchange under Turbulent Conditions, *Deep-Sea Res*, *35*(12), 1953-1970.

Gordon, L., and A. Lohrmann (2002), Near-shore doppler current meter wave spectra, in *Proc. Fourth International Symp. on Wave Measurement and Analysis: WAVES 2001*, edited, pp. 33-43, San Francisco, CA, ASCE.

Gray, C., C. A. Greated, D. R. Mccluskey, and W. J. Easson (1991), An Analysis of the Scanning Beam Piv Illumination System, *Meas Sci Technol*, *2*(8), 717-724.

Guerin, F., G. Abril, D. Serca, C. Delon, S. Richard, R. Delmas, A. Tremblay, and L. Varfalvy (2007), Gas transfer velocities of CO(2) and CH(4) in a tropical reservoir and its river downstream, *J Marine Syst*, *66*(1-4), 161-172.

Hackett, E. E., L. Luznik, A. R. Nayak, J. Katz, and T. R. Osborn (2011), Field measurements of turbulence at an unstable interface between current and wave bottom boundary layers, *J Geophys Res-Oceans*, *116*.

Hare, J. E., C. W. Fairall, W. R. McGillis, J. B. Edson, B. Ward, and R. Wanninkhof (2004), Evaluation of the National Oceanic and Atmospheric Administration/Coupled-Ocean Atmospheric Response Experiment (NOAA/COARE) air-sea gas transfer parameterization using GasEx data, *J Geophys Res-Oceans*, *109*(C8).

Harriott, P. (1962), A random eddy modification of the penetration theory, *Chem Eng Sci*, *17*, 149-154.

Hauß ecker, H., and B. Jähne (1995), In situ measurements of the air-sea gas transfer rate during the MBL/CoOP west coast experiment, in *Air Water Gas Transfer*, edited by B. Jähne and E. C. Monahan, pp. 775-784.

Haußecker, H., B. Jähne, and S. Reinelt (1995), Heat as a proxy tracer for gas exchange measurements in the field: principles and technical realization, in *Air Water Gas Transfer*, edited by B. Jähne and E. C. Monahan, pp. 405-413.

Herlina, and G. H. Jirka (2004), Application of LIF to investigate gas transfer near the air-water interface in a grid-stirred tank, *Exp Fluids*, *37*(3), 341-349.

Herlina, and G. H. Jirka (2008), Experiments on gas transfer at the air-water interface induced by oscillating grid turbulence, *J Fluid Mech*, *594*, 183-208.

Higbie, R. (1935), The rate of absorption of a pure gas into a still liquid during short periods of exposure, *AIChE Transactions*, *31*, 365-390.

Hinze, J. O. (1975), *Turbulence*, McGraw-Hill.

Ho, D. T., P. Schlosser, and P. M. Orton (2011a), On Factors Controlling Air-Water Gas Exchange in a Large Tidal River, *Estuar Coast*, *34*(6), 1103-1116.

Ho, D. T., L. F. Bliven, R. Wanninkhof, and P. Schlosser (1997), The effect of rain on air-water gas exchange, *Tellus B*, *49*(2), 149-158.

Ho, D. T., W. E. Asher, L. F. Bliven, P. Schlosser, and E. L. Gordan (2000), On mechanisms of rain-induced air-water gas exchange, *J Geophys Res-Oceans*, *105*(C10), 24045-24057.

Ho, D. T., C. S. Law, M. J. Smith, P. Schlosser, M. Harvey, and P. Hill (2006a), Measurements of air-sea gas exchange at high wind speeds in the Southern Ocean: Implications for global parameterizations, *Geophys Res Lett*, *33*(16).

Ho, D. T., C. S. Law, M. J. Smith, P. Schlosser, M. Harvey, and P. Hill (2006b), Measurements of air-sea gas exchange at high wind speeds in the Southern Ocean: Implications for global parameterizations (vol 33, art no L16611, 2006), *Geophys Res Lett*, *33*(20).

Ho, D. T., F. Veron, E. Harrison, L. F. Bliven, N. Scott, and W. R. McGillis (2007), The combined effect of rain and wind on air-water gas exchange: A feasibility study, *J Marine Syst*, *66*(1-4), 150-160.

Ho, D. T., R. Wanninkhof, P. Schlosser, D. S. Ullman, D. Hebert, and K. F. Sullivan (2011b), Toward a universal relationship between wind speed and gas exchange: Gas transfer velocities measured with (3)He/SF(6) during the Southern Ocean Gas Exchange Experiment, *J Geophys Res-Oceans*, *116*.

Ho, D. T., C. J. Zappa, W. R. McGillis, L. F. Bliven, B. Ward, J. W. H. Dacey, P. Schlosser, and M. B. Hendricks (2004), Influence of rain on air-sea gas exchange: Lessons from a model ocean, *J Geophys Res-Oceans*, *109*(C8).

Ho, D. T., C. L. Sabine, D. Hebert, D. S. Ullman, R. Wanninkhof, R. C. Hamme, P. G. Strutton, B. Hales, J. B. Edson, and B. R. Hargreaves (2011c), Southern Ocean Gas Exchange Experiment: Setting the stage, *J Geophys Res-Oceans*, *116*.

Huang, C. J., and F. L. Qiao (2010), Wave-turbulence interaction and its induced mixing in the upper ocean, *J Geophys Res-Oceans*, *115*.

Huang, N. E., Z. Shen, S. R. Long, M. L. C. Wu, H. H. Shih, Q. N. Zheng, N. C. Yen, C. C. Tung, and H. H. Liu (1998), The empirical mode decomposition and the Hilbert spectrum for nonlinear and non-stationary time series analysis, *P Roy Soc Lond a Mat*, *454*(1971), 903-995.

Hunt, J. C. R., and J. M. R. Graham (1978), Free stream turbulence near plane boundaries, *J Fluid Mech*, *84*, 209-235.

Jähne, B., and H. Haußecker (1998), Air-water gas exchange, *Annu Rev Fluid Mech*, *30*, 443-468.

Jähne, B., W. Huber, A. Dutzi, T. Wais, and J. Ilmberger (1984), Wind/wave-tunnel experiments on the Schmidt number and wave field dependence of air-water gas exchange, in *Gas transfer at water surfaces*, edited by W. Brutsaert and G. H. Jirka, pp. 303-309.

Jähne, B., K. O. Munnich, R. Bosinger, A. Dutzi, W. Huber, and P. Libner (1987), On the Parameters Influencing Air-Water Gas-Exchange, *J Geophys Res-Oceans*, *92*(C2), 1937-1949.

Jessup, A. T., W. E. Asher, M. Atmane, K. Phadnis, C. J. Zappa, and M. R. Loewen (2009), Evidence for complete and partial surface renewal at an air-water interface, *Geophys Res Lett*, *36*.

Jones, N. L., and S. G. Monismith (2008), Modeling the influence of wave-enhanced turbulence in a shallow tide- and wind-driven water column, *J Geophys Res-Oceans*, *113*(C3).

Katija, K., and J. O. Dabiri (2008), In situ field measurements of aquatic animal-fluid interactions using a Self-Contained Underwater Velocimetry Apparatus (SCUVA), *Limnol Oceanogr-Meth*, *6*, 162-171.

Kawahashi, M., and K. Hosoi (1989), Beam-Sweep Laser Speckle Velocimetry, *Exp Fluids*, *8*(1-2), 109-111.

Kawahashi, M., and K. Hosoi (1991), Dual-Beam-Sweep Laser Speckle Velocimetry, *Exp Fluids*, *11*(4), 278-280.

Kitaigorodskii, S. A. (1984), On the field dynamical theory of turbulent gas transfer across an air-sea interface in the presence of breaking waves, *J Phys Oceanogr*, *14*, 960-972.

Kremer, J. N., S. W. Nixon, B. Buckley, and P. Roques (2003), Technical note: Conditions for using the floating chamber method to estimate air-water gas exchange, *Estuaries*, *26*(4A), 985-990.

Lamarre, E., and W. K. Melville (1991), Air Entrainment and Dissipation in Breaking Waves, *Nature*, *351*(6326), 469-472.

Lamont, J. C., and D. S. Scott (1970), An eddy cell model of mass transfer into the surface of a turbulent liquid, *Aiche J*, *16*, 513-519.

Large, W. G., and S. Pand (1981), Open ocean momentum flux measurements in moderate to strong winds, *J Phys Oceanogr*, *11*, 324-336.

Lewis, W. K., and W. G. Whitman (1924), Principles of Gas Absorption, *Ind. Eng. Chem.*, *16*(12), 1215-1220.

Liao, Q., and E. A. Cowen (2005), An efficient anti-aliasing spectral continuous window shifting technique for PIV, *Exp Fluids*, *38*(2), 197-208.

Liao, Q., H. A. Bootsma, J. E. Xiao, J. V. Klump, A. Hume, M. H. Long, and P. Berg (2009), Development of an in situ underwater particle image velocimetry (UWPIV) system, *Limnol Oceanogr-Meth*, *7*, 169-184.

Liss, P. S. (1983), Gas transfer: experiments and geochemical implications., in *Air-sea exchange of gases and partilces*, edited by P. S. Liss and W. G. Slinn, pp. 241-298.

Liss, P. S., and L. Merlivat (1986), Air-sea gas exchange rates: introduction and synthesis, in *The role of air-sea exchange in geochemical cycling*, edited by P. Buat-Menard, pp. 113-129.

Lorke, A., and A. Wuest (2005), Application of coherent ADCP for turbulence measurements in the bottom boundary layer, *J Atmos Ocean Tech*, *22*(11), 1821-1828.

Lorke, A., and F. Peeters (2006), Toward a unified scaling relation for interfacial fluxes, *J Phys Oceanogr*, *36*(5), 955-961.

MacIntyre, S., A. Jonsson, M. Jansson, J. Aberg, D. E. Turney, and S. D. Miller (2010), Buoyancy flux, turbulence, and the gas transfer coefficient in a stratified lake, *Geophys Res Lett*, *37*.

Matthews, C. J. D., V. L. St Louis, and R. H. Hesslein (2003), Comparison of three techniques used to measure diffusive gas exchange from sheltered aquatic surfaces, *Environ Sci Technol*, *37*(4), 772-780.

McCready, M. J., E. Vassilliadou, and T. J. Hanratty (1986), Computer simulation of turbulent mass transfer at a mobile interface, *Aiche J*, *32*, 1108-1115.

McGillis, W. R., J. B. Edson, J. E. Hare, and C. W. Fairall (2001), Direct covariance air-sea CO2 fluxes, *J Geophys Res-Oceans*, *106*(C8), 16729-16745.

McGillis, W. R., et al. (2004), Air-sea CO2 exchange in the equatorial Pacific, *J Geophys Res-Oceans*, *109*(C8).

McKenna, S. P., and W. R. McGillis (2004), The role of free-surface turbulence and surfactants in air-water gas transfer, *Int J Heat Mass Tran*, *47*(3), 539-553.

McNeil, C., and E. D'Asaro (2007), Parameterization of air-sea gas fluxes at extreme wind speeds, *J Marine Syst*, *66*(1-4), 110-121.

Melville, W. K. (1994), Energy-Dissipation by Breaking Waves, *J Phys Oceanogr*, *24*(10), 2041-2049.

Melville, W. K. (1996), The role of surface-wave breaking in air-sea interaction, *Annu Rev Fluid Mech*, *28*, 279-&.

Melville, W. K., F. Veron, and C. J. White (2002), The velocity field under breaking waves: coherent structures and turbulence, *J Fluid Mech*, *454*, 203-233.

Merlivat, L., and L. Memery (1983), Gas exchange across an air-water interface: experimental results and modelling of bubble contribution to transfer, *J Geophys Res-Oceans*, *88*, 707-724.

Monahan, A. H. (2006), The probability distribution of sea surface wind speeds. Part 1: Theory and SeaWinds observations, *J Climate*, *19*(4), 497-520.

Naegler, T., P. Ciais, K. Rodgers, and I. Levin (2006), Excess radiocarbon constraints on air-sea gas exchange and the uptake of CO2 by the oceans, *Geophys Res Lett*, *33*(11).

Nightingale, P. D., G. Malin, C. S. Law, A. J. Watson, P. S. Liss, M. I. Liddicoat, J. Boutin, and R. C. Upstill-Goddard (2000), In situ evaluation of air-sea gas exchange parameterizations using novel conservative and volatile tracers, *Global Biogeochem Cy*, *14*(1), 373-387.

Nimmo Smith, W. A. M., J. Katz, and T. R. Osborn (2005), On the structure of turbulence in the bottom boundary layer of the coastal ocean, *J Phys Oceanogr*, *35*(1), 72-93.

Nimmo Smith, W. A. M., P. Atsavapranee, J. Katz, and T. R. Osborn (2002), PIV measurements in the bottom boundary layer of the coastal ocean, *Exp Fluids*, *33*(6), 962-971.

Osborn, T. R., and R. G. Lueck (1985), Turbulence measurements from a towed body, *J Atmos Ocean Tech*, *2*, 517-527.

Peirson, W. L. (1997), Measurement of surface velocities and shears at a wavy air-water interface using particle image velocimetry, *Exp Fluids*, *23*(5), 427-437.

Rapp, R. J., and W. K. Melville (1990), Laboratory Measurements of Deep-Water Breaking Waves, *Philos T Roy Soc A*, *331*(1622), 735-&.

Raymond, P. A., and J. J. Cole (2001), Gas exchange in rivers and estuaries: Choosing a gas transfer velocity, *Estuaries*, *24*(2), 312-317.

Read, J. S., et al. (2012), Lake-size dependency of wind shear and convection as controls on gas exchange, *Geophys Res Lett*, *39*.

Saylor, J. R., G. B. Smith, and K. A. Flack (2000), The effect of a surfactant monolayer on the temperature field of a water surface undergoing evaporation, *Int J Heat Mass Tran*, *43*(17), 3073-3086.

Schlussel, P., A. V. Soloviev, and W. J. Emery (1997), Cool and freshwater skin of the ocean during rainfall, *Bound-Lay Meteorol*, *82*(3), 437-472.

Sheng, J., H. Meng, and R. O. Fox (2000), A large eddy PIV method for turbulence dissipation rate estimation, *Chem Eng Sci*, *55*(20), 4423-4434.

Siddiqui, K., and M. R. Loewen (2010), Phase-Averaged Flow Properties Beneath Microscale Breaking Waves, *Bound-Lay Meteorol*, *134*(3), 499-523.

Siddiqui, M. H. K., and M. R. Loewen (2007), Characteristics of the wind drift layer and microscale breaking waves, *J Fluid Mech*, *573*, 417-456.

Siddiqui, M. H. K., M. R. Loewen, W. E. Asher, and A. T. Jessup (2004), Coherent structures beneath wind waves and their influence on air-water gas transfer, *J Geophys Res-Oceans*, *109*(C3).

Smith, S. D., et al. (1992), Sea-Surface Wind Stress and Drag Coefficients - the Hexos Results, *Bound-Lay Meteorol*, *60*(1-2), 109-142.

Soloviev, A., M. Donelan, H. Graber, B. Haus, and P. Schlussel (2007), An approach to estimation of near-surface turbulence and CO2 transfer velocity from remote sensing data, *J Marine Syst*, *66*(1-4), 182-194.

Sreenivasan, K. R. (1995), On the Universality of the Kolmogorov Constant, *Phys Fluids*, *7*(11), 2778-2784.

Steinbuck, J. V., P. L. D. Roberts, C. D. Troy, A. R. Horner-Devine, F. Simonet, A. H. Uhlman, J. S. Jaffe, S. G. Monismith, and P. J. S. Franks (2010), An Autonomous Open-Ocean Stereoscopic PIV Profiler, *J Atmos Ocean Tech*, *27*(8), 1362-1380.

Takagaki, N., and S. Komori (2007), Effects of rainfall on mass transfer across the air-water interface, *J Geophys Res-Oceans*, *112*(C6).

Takahashi, T., et al. (2002), Global sea-air CO2 flux based on climatological surface ocean pCO(2), and seasonal biological and temperature effects, *Deep-Sea Res Pt Ii*, *49*(9-10), 1601-1622.

Teixeira, M. A. C. (2012), The influence of Langmuir turbulence on the scaling for the dissipation rate in the oceanic boundary layer, *J Geophys Res-Oceans*, *117*.

Terray, E. A., M. A. Donelan, Y. C. Agrawal, W. M. Drennan, K. K. Kahma, A. J. Williams, P. A. Hwang, and S. A. Kitaigorodskii (1996), Estimates of kinetic energy dissipation under breaking waves, *J Phys Oceanogr*, *26*(5), 792-807.

Thais, L., and J. Magnaudet (1996), Turbulent structure beneath surface gravity waves sheared by the wind, *J Fluid Mech*, *328*, 313-344.

Theofanus, T. G., R. N. Houze, and L. K. Brumfield (1976), Turbulent mass transfer at free, gas liquid interfaces with applications to open channel, bubble and jet flows, *Int J Heat Mass Tran*, *19*(6), 613-624.

Tokoro, T., A. Watanabe, H. Kayanne, K. Nadaoka, H. Tamura, K. Nozakid, K. Kato, and A. Negishi (2007), Measurement of air-water CO2 transfer at four coastal sites using a chamber method, *J Marine Syst*, *66*(1-4), 140-149.

Tritico, H. M., A. J. Cotel, and J. N. Clarke (2007), Development, testing and demonstration of a portable submersible miniature particle imaging velocimetry device, *Meas Sci Technol*, *18*(8), 2555-2562.

Tsai, W. T. (1996a), Impact of a surfactant on a turbulent shear layer under the air-sea interface, *J Geophys Res-Oceans*, *101*(C12), 28557-28568.

Tsai, W. T. (1996b), Effects of surfactant on free-surface turbulent shear flow, *Int Commun Heat Mass*, *23*(8), 1087-1095.

Tsai, W. T., and D. K. P. Yue (1995), Effects of Soluble and Insoluble Surfactant on Laminar Interactions of Vortical Flows with a Free-Surface, *J Fluid Mech*, *289*, 315-349.

Tsai, W. T., and K. K. Liu (2003), An assessment of the effect of sea surface surfactant on global atmosphere-ocean CO2 flux, *J Geophys Res-Oceans*, *108*(C4).

Turney, D. E., W. C. Smith, and S. Banerjee (2005), A measure of near-surface fluid motions that predicts air-water gas transfer in a wide range of conditions, *Geophys Res Lett*, *32*(4).

Upstill-Goddard, R. C. (2006), Air-sea gas exchange in the coastal zone, *Estuar Coast Shelf S*, *70*(3), 388-404.

Upstill-goddard, R. C., A. J. Watson, P. S. Liss, and M. I. Liddicoat (1990), Gas transfer velocities in lakes measured with SF_6, *Tellus B*, *42*, 364-377.

Vachon, D., Y. T. Prairie, and J. J. Cole (2010), The relationship between near-surface turbulence and gas transfer velocity in freshwater systems and its implications for floating chamber measurements of gas exchange, *Limnol Oceanogr*, *55*(4), 1723-1732.

Veron, F., and W. K. Melville (1999), Pulse-to-pulse coherent Doppler measurements of waves and turbulence, *J Atmos Ocean Tech*, *16*(11), 1580-1597.

Veron, F., W. K. Melville, and L. Lenain (2009), Measurements of Ocean Surface Turbulence and Wave-Turbulence Interactions, *J Phys Oceanogr*, *39*(9), 2310-2323.

Wang, B., Q. Liao, H. A. Bootsma, and P. F. Wang (2012), A dual-beam dual-camera method for a battery-powered underwater miniature PIV (UWMPIV) system, *Exp Fluids*, *52*(6), 1401-1414.

Wang, B., Q. Liao, J. Xiao, and H. A. Bootsma (2013), A free-floating PIV system: measurements of small-scale turbulence under the wind wave surface, *J Atmos Ocean Tech*, *In press*. doi: http://dx.doi.org/10.1175/JTECH-D-12-00092.1

Wang, B., Q. Liao, Fillingham J. H. and H. A. Bootsma (2013b), a novel eddy model for prediction of air-water gas transfer velocity, *Geophys Res Lett*, under review.

Wanninkhof, R. (1992), Relationship between Wind-Speed and Gas-Exchange over the Ocean, *J Geophys Res-Oceans*, *97*(C5), 7373-7382.

Wanninkhof, R., and W. R. McGillis (1999), A cubic relationship between air-sea CO2 exchange and wind speed, *Geophys Res Lett*, *26*(13), 1889-1892.

Wanninkhof, R., J. R. Ledwell, and W. S. Broecker (1985), Gas exchange-wind speed relation measured with sulfur hexafluoride on a lake, *Science*, *227*(4691), 1224-1226.

Wanninkhof, R., W. Asher, and E. C. Monahan (1995), The influence of bubbles on air-water gas exchange results from gas transfer experiments during WABEX-93, in *Air-*

water gas transfer, edited by B. Jähne and E. C. Monahan, pp. 239-254, AEON Verlag & Studio, Hanau.

Wanninkhof, R., K. F. Sullivan, and Z. Top (2004), Air-sea gas transfer in the Southern Ocean, *J Geophys Res-Oceans*, *109*(C8).

Wanninkhof, R., J. R. Ledwell, W. S. Broecker, and M. Hamilton (1987), Gas-Exchange on Mono Lake and Crowley Lake, California, *J Geophys Res-Oceans*, *92*(C13), 14567-14580.

Wanninkhof, R., W. E. Asher, D. T. Ho, C. Sweeney, and W. R. McGillis (2009), Advances in Quantifying Air-Sea Gas Exchange and Environmental Forcing, *Annu Rev Mar Sci*, *1*, 213-244.

Wanninkhof, R., W. Asher, R. Weppernig, H. Chen, P. Schlosser, C. Langdon, and R. Sambrotto (1993), Gas Transfer Experiment on Georges Bank Using 2 Volatile Deliberate Tracers, *J Geophys Res-Oceans*, *98*(C11), 20237-20248.

Wanninkhof, R. H., and L. F. Bliven (1991), Relationship between Gas-Exchange, Wind-Speed, and Radar Backscatter in a Large Wind-Wave Tank, *J Geophys Res-Oceans*, *96*(C2), 2785-2796.

Watson, A. J., R. C. Upstillgoddard, and P. S. Liss (1991), Air Sea Gas-Exchange in Rough and Stormy Seas Measured by a Dual-Tracer Technique, *Nature*, *349*(6305), 145-147.

Webb, E. K., G. I. Pearman, and R. Leuning (1980), Correction of flux measurements for density effects due to heat and water vapour transfer, *Q J Roy Meteor Soc*, *106*, 85-100.

Wentz, F. J., S. Peteherych, and L. A. Thomas (1984), A model function for ocean radar cross section at 14.6 GHz, *J Geophys Res-Oceans*, *83*, 3689-3704.

Woolf, D. K. (1993), Bubbles and the Air-Sea Transfer Velocity of Gases, *Atmos Ocean*, *31*(4), 517-540.

Woolf, D. K. (1997), Bubbles and their role in gas exchange, in *The sea surface and global changes*, edited by P. S. Liss and R. A. Duce, pp. 173-205, Cambridge University Press, Cambridge.

Woolf, D. K. (2005), Parametrization of gas transfer velocities and sea-state-dependent wave breaking, *Tellus B*, *57*(2), 87-94.

Woolf, D. K., and S. A. Thorpe (1991), Bubbles and the Air-Sea Exchange of Gases in near-Saturation Conditions, *J Mar Res*, *49*(3), 435-466.

Woolf, D. K., et al. (2007), Modelling of bubble-mediated gas transfer: Fundamental principles and a laboratory test, *J Marine Syst*, *66*(1-4), 71-91.

Wuest, A., and A. Lorke (2003), Small-scale hydrodynamics in lakes, *Annu Rev Fluid Mech*, *35*, 373-412.

Yelland, M., and P. K. Taylor (1996), Wind stress measurements from the open ocean, *J Phys Oceanogr*, *26*(4), 541-558.

Yelland, M. J., B. I. Moat, P. K. Taylor, R. W. Pascal, J. Hutchings, and V. C. Cornell (1998), Wind stress measurements from the open ocean corrected for airflow distortion by the ship, *J Phys Oceanogr*, *28*(7), 1511-1526.

Zappa, C. J., W. E. Asher, and A. T. Jessup (2001), Microscale wave breaking and air-water gas transfer, *J Geophys Res-Oceans*, *106*(C5), 9385-9391.

Zappa, C. J., P. A. Raymond, E. A. Terray, and W. R. McGillis (2003), Variation in surface turbulence and the gas transfer velocity over a tidal cycle in a macro-tidal estuary, *Estuaries*, *26*(6), 1401-1415.

Zappa, C. J., W. E. Asher, A. T. Jessup, J. Klinke, and S. R. Long (2004), Microbreaking and the enhancement of air-water transfer velocity, *J Geophys Res-Oceans*, *109*(C8).

Zappa, C. J., W. R. McGillis, P. A. Raymond, J. B. Edson, E. J. Hintsa, H. J. Zemmelink, J. W. H. Dacey, and D. T. Ho (2007), Environmental turbulent mixing controls on air-water gas exchange in marine and aquatic systems, *Geophys Res Lett*, *34*(10).

Zappa, C. J., D. T. Ho, W. R. McGillis, M. L. Banner, J. W. H. Dacey, L. F. Bliven, B. Ma, and J. Nystuen (2009), Rain-induced turbulence and air-sea gas transfer, *J Geophys Res-Oceans*, *114*.

Zemmelink, H. J., J. W. H. Dacey, and E. J. Hintsa (2004), Direct measurements of biogenic dimethylsulphide fluxes from the oceans: a synthesis, *Can J Fish Aquat Sci*, *61*(5), 836-844.

Zemmelink, H. J., W. W. C. Gieskes, W. Klaassen, H. W. de Groot, H. J. W. de Baar, J. W. H. Dacey, E. J. Hintsa, and W. R. McGillis (2002), Simultaneous use of relaxed eddy accumulation and gradient flux techniques for the measurement of sea-to-air exchange of dimethyl sulphide, *Atmos Environ*, *36*(36-37), 5709-5717.

Zhang, W. Q., W. Perrie, and S. Vagle (2006), Impacts of winter storms on air-sea gas exchange, *Geophys Res Lett*, *33*(14).

Zhao, D., Y. Toba, Y. Suzuki, and S. Komori (2003), Effect of wind waves on air-sea gas exchange: proposal of an overall CO2 transfer velocity formula as a function of breaking-wave parameter, *Tellus B*, *55*(2), 478-487.

CURRICULUM VITAE

BINBIN WANG

Education:

2009-Present, Ph.D. Candidate
Department of Civil Engineering & Mechanics, University of Wisconsin – Milwaukee
2006-2009, M.S.
Key Laboratory of Fire Science, University of Science and Technology of China
2000-2004, B.S.
The College of Physics and Electronic Information, Anhui Normal University

Research Experiences:

2009-Present, Research Assistant
Department of Civil Engineering & Mechanics, University of Wisconsin – Milwaukee
Topic and research interest: The development of in situ UnderWater Particle Image Velocimetry; Turbulence generation mechanism in wind wave surface boundary layer; Transport process (momentum, heat, mass) across the air-water interface; Bacteria transport process in porous media.

2009, Visiting Scholar
Department of Building Services Engineering, The Hong Kong Polytechnic University
Topic: Numerical studies on large high-rise building fire

2006-2009, Research Assistant
State Key Lab of Fire Science, University of Science and Technology of China
Topic: Flame kinetics and dynamics; Reduced mechanism based on Computational Singular Perturbation method; Effect of Hydrogen addition on premixed LPG/Air flame

Teaching Experiences:

2012 Spring, 2012 Fall, Teaching Assistant
Department of Civil Engineering & Mechanics, University of Wisconsin – Milwaukee
Topic: CIVENG 411 Engineering Principles of Water Resources Design

2004-2006, Instructor, Laboratory Instructor
Hefei 168 Senior high school
Topic: Physics

Honors and Awards:

2013, Liege Colloquium of Ocean Dynamics Travel Award
2012, Ocean Science Meeting Outstanding Student Presentation Award
2012, UWM Graduate student Travel Award
2009-2013, UWM Chancellor's Graduate Student Award
2011, 3rd Anhui Province Distinguished Master-Thesis
2009, USTC Distinguished Graduate Student Award
2008, USTC "Ruihengda" Fellowship

Peer Reviewed Journal Publications:

[8] **Wang, B.**; Liao, Q.; Bootsma, H. A. Field observations of enhanced turbulent dissipation rate structure in the wave affect surface layer (preparing for Journal of Geophysical Research: Oceans)

[7] **Wang, B.**; Liao, Q.; Fillingham, J. H. and Bootsma, H. A. On A novel eddy model for prediction of air-water gas transfer velocity. 2013, Geophysical Research Letters, under review.

[6] **Wang, B.**; Liao, Q.; Xiao, J. and Bootsma, H. A. A free-floating PIV system: measurements of small-scale turbulence under the wind wave surface, Journal of Atmospheric and Oceanic Technology, 2013, in press.

[5] **Wang, B.**; Liao, Q.; Bootsma, H. A. and Wang, P. A Dual-Beam-Dual-Camera Method for a Battery-Powered UnderWater Miniature PIV (UWMPIV) System. Exp. Fluids, 2012, 52(6), 1401-1414.

[4] Zong, H., Wu, C., **Wang, B.**, Jiang, P. and Qiu, R. Study of influence of water sprinkler on fire spread and smoke movement in storehouse fire based on numerical simulation. Journal of Safety and Technology. 2008, 4(1), 10-14 (In Chinese)

[3] Yang, L., **Wang, B.** and Jiang, Y. Study on the smoke movement of an indoor street based on numerical simulation. Journal of Safety and Technology. 2008, 4(4), 51-54 (In Chinese)

[2] **Wang, B.**, Qiu, R. and Jiang, Y. Effects of hydrogen enhancement in LPG/Air premixed flame. Acta Physico-Chimica Sinica. 2008, 24(07), 1137-1142

[1] **Wang, B.**, Jiang, Y. and Qiu, R. Application of CSP in reduction of complex combustion reaction system. Acta Physico-Chimica Sinica. 2008, 24(12), 2221-2228 (In Chinese)

Peer Reviewed Book Chapters:

[1] Liao, Q. and **Wang, B.** (2013). Near surface turbulence and gas exchange across the air-sea interface. In E. Zambianchi Editor (Eds), Oceanography Reasearch. (accepted)

Conference Proceedings (Refereed Full Paper):

[6] **Wang, B.**; Liao, Q.; Xiao, J. and Bootsma, H. A. High resolution vertical profiles of near surface turbulence on open lake. Hydraulic Measurement & Experimental Methods Conference. August 12-15, 2012, Snowbird, UT, USA.

[5] Xiao, J.; Liao, Q.; **Wang, B.** and Bootsma, H. A. *In situ* measurement of grazing effects of Dreissenid mussels in Lake Michigan. Hydraulic Measurement & Experimental Methods Conference. August 12-15, 2012, Snowbird, UT, USA.

[4] Liao, Q.; **Wang, B.** and Bootsma, H. A. Measurement of near surface turbulence on the aqueous side of the air-water interface with a self-contained floating PIV system. The 16th International Symposium on Applications of Laser Techniques to Fluid Mechanics. July 9-12, Lisbon, Portugal.

[3] **Wang, B.**; Xiao, J.; Liao, Q and Bootsma, H. A. *In situ* PIV measurement of small scale turbulence in a wind wave boundary layer. 3rd Int. Symp. On Shallow Flows, June 4-6, 2012, Iowa City, IA, USA.

[2] Xiao, J.; **Wang, B.**; Liao, Q and Bootsma, H. A. Field measurements of wave-current interaction in the bottom boundary layer of Lake Michigan. 3rd Int. Symp. On Shallow Flows, June 4-6, 2012, Iowa City, IA, USA.

[1] **Wang, B.**, Jiang, Y. Qiu, R. and An, J. Construction of combustion mechanism of typical fuel and numerical simulation of pollution and control of characteristic toxicant. (In Chinese) Annual Conference of The Chinese Society of Engineering Thermophysics – Combustion. Oct 30 – Nov 2, 2009, Hefei, China.

Conference Proceedings (Refereed Abstract):

[6] Fillingham, J.H.; **Wang, B.**; Bootsma, H. A. and Liao, Q. Towards a parameterization for the CO2 gas transfer velocity useful for biogeochemical modeling of the Great Lakes. 56th Annual Conference on Great Lakes Research, June 2-6, 2013, West Lafayette, IN, USA

[5] **Wang, B.**; Fillingham, J.H.; Liao, Q. and Bootsma, H.A. Evaluating gas transfer velocity with *in situ* free floating PIV/flating chamber measurements. 56th Annual Conference on Great Lakes Research, June 2-6, 2013, West Lafayette, IN, USA

[4] **Wang, B.**; Liao, Q.; Bootsma, H.A. and Fillingham, J.H. *In situ* turbulence measurement and its relation to air-water gas exchange rate. 45th Liege Colloquium of Ocean Dynamics. May 13-17, 2013, Liege, Belgium (poster).

[3] **Wang, B.**; Liao, Q.; Xiao, J.; Bootsma, H. A. and Wu, C. H. Measurement of the structure of turbulence in a wind wave boundary layer with an *in situ* PIV system. TOS/ASLO/AGU Ocean Science Meeting. Feb 20-24, 2012, Salt Lake City, UT, USA

[2] Xiao, J.; Liao, Q.; Bootsma, H. A. and **Wang, B**. *In situ* measurements of fluxes of particles and dissolved phosphors over a quagga mussel bed in Lake Michigan. TOS/ASLO/AGU Ocean Science Meeting. Feb 20-24, 2012, Salt Lake City, UT, USA

[1] **Wang, B.**; Liao, Q and Bootsma, H. A. The development of the second generation of *in situ* Particle Image Velocimetry (PIV). 53rd Annual Conference on Great Lakes Research, May 17-21, 2010, Toronto, Canada.